

CHARLES UNIVERSITY

Faculty of Science

Developmental and Cell Biology



Katarzyna I. Szczerkowska

Function of Zinc finger protein 644 (Zfp644) in mouse organism.

Doctoral Thesis

Supervisor: Assoc. Prof. Radislav Sedlacek, Ph.D

Co-Supervisor: Jan Prochazka, PhD

Dept. of Transgenic Models of Diseases; Institute of Molecular Genetics AS CR, v.v.i.

Prague, 2021

Prohlášení:

Prohlašuji, že jsem závěrečnou práci zpracovala samostatně a že jsem uvedla všechny použité informační zdroje a literaturu. Tato práce ani její podstatná část nebyla předložena k získání jiného nebo stejného akademického titulu.

V Praze, 19.10.2021

Acknowledgements

I am grateful to my supervisors Assoc. Prof. Radislav Sedlacek, PhD and Jan Prochazka, PhD for their invaluable advice, continuous support, and patience during my PhD study. I would also like to acknowledge Silvia Petrezselyova, PhD and Jan Dvorak, PhD for their technical support, especially at the beginning of my study. My upmost regards go to all the members of Czech Center for Phenogenomics and Laboratory of Transgenic Models of Diseases, especially those involved in my projects, among the others Petr Kaspar, PhD and Vendula Novosadova, PhD. It is their kind help and support that have made my study successful. I would also like to thank my friends and lab mates for a cherished time spent together in the lab, and in social settings. Foremost, I would like to express my extreme gratitude to my parents and my partner. Without their tremendous understanding and encouragement in the past few years, it would be impossible for me to complete my study.

Abstract

ZNF644 (Zinc Finger Protein 644) is a C2H2 zinc finger gene encoding a putative transcription regulator, of which a point mutation (S672G) is associated with inherited high myopia in humans. It is also described to be a partner of the G9a/GLP (G9a- euchromatic histone-lysine *N*-methyltransferase 2, EHMT2; GLP - euchromatic histone-lysine *N*-methyltransferase 1, EHMT1) complex, known for its essential role in histone methylation, specifically H3K9me1 and H3K9me2. It was reported that another transcription factor, WIZ (Widely-Interspaced Zinc Finger-Containing Protein), can bind to this complex and cooperate in gene silencing simultaneously.

In order to study *Zfp644* impact on myopia, we generated a mouse model, *Zfp644*^{S673G} that mimics human mutation. In addition, a mouse with a persuasive truncated form of the protein, *Zfp644*^{Δ8} was created. Both mouse models went through an examination of retinal function and morphology. Moreover, with use of ultrasonography, different ocular parameters were examined. We conclude, that *Zfp644* gene is causative for myopia in mice. Further examinations of *Zfp644*^{Δ8} animals show severe symptoms in metabolism and female fertility. To describe the impact of *Zfp644* in mouse fertility we performed various experiments including analysis of expression of *Zfp644* in reproductive organs, breeding performance, ovarian morphometry and estrus cycle. Additionally, a full knockout mouse model named *Zfp644*^{-/-} was prepared and analyzed together with *Zfp644*^{Δ8} in the fertility study. The levels of hormones crucial for correct estrus cycling, in each of the phases, was analyzed. We also followed the development of mammary gland growth during puberty and during pregnancy. We found striking differences in *Zfp644*^{Δ8} females, when compared to *Zfp644*^{-/-} and control animals. The studies were complemented by the mammary gland organoids assays. Furthermore, a transplantation of ovaries from *Zfp644*^{Δ8} homozygous to control animal; and vice-versa was performed. We rescued homozygous *Zfp644*^{Δ8} ovaries transplanted to control animals. Ovaries were fully functional and females were able to successfully breed and deliver multiple litters. However, *Zfp644*^{Δ8} homozygous females after transplantation of ovaries remain sub-fertile. To fully rescue the subfertility phenotype in *Zfp644*^{Δ8} females, we decided to apply hormone replacement therapy. We were able to successfully breed *Zfp644*^{Δ8} homozygous females and generate the viable offspring when applying progesterone therapy. Taken together,

our most recent data shows strong aberration in female sex hormone homeostasis, which seems to be the cause of the female infertility we observed.

To complement our study by further exploration of G9a/GLP complex function, we expanded our research by another transcription factor, working simultaneously with G9a/GLP complex and ZNF644, WIZ protein. Similar to *Zfp644* studies, we investigated a role of *Wiz* knockout in mouse. Unlike *Zfp644*, functional ablation of *Wiz* causes late embryonic lethality. However not as early as *G9a* nor *GLP* knockout mice. That might suggest higher importance of *Wiz* protein when compared to *Zfp644* in the methylation complex but not crucial for methylation in early embryonic stages. Morphological changes were deeply analyzed in embryos between E14.5 to E18.5. The most severe malformations include a shorter snout, cleft palate and cleft eyelids. Moreover, we analyzed the histone methylation to understand the impact of *Wiz* knockout on G9a/GLP function. Based on the data, we conclude that the histone methylation pattern is suppressed. Our data strongly suggest, that *Wiz* plays an important role in the G9a/GLP methylation complex, especially in craniofacial development.

Taken together, this work presents a novel data that could be valuable for further studies on ZNF644, WIZ and G9a/GLP complex. The close similarity between human and mouse Zinc Finger Protein 644 implies the possibility for translation of our study on myopia to human medicine in the future. Further research on the G9a/GLP methylation complex and its action in the organism, influenced by ZNF644 and WIZ is necessary, however, we believe that presented data might shed a light on molecular mechanism of this complex.

Key words: *Zfp644*, ZNF644, WIZ, G9a, GLP, histone methylation, transcription factor, vision, fertility, development

Abstrakt

Gen ZNF644 kóduje transkripční regulátor Zinc Finger Protein 644 patřící do podrodiny Cys2-His2 zinc finger proteinů. Mutace lidského ZNF644 (S672G) způsobuje vážnou dědičnou myopii. Výzkum ukázal, že ZNF644 ovlivňuje expresi podřízených genů prostřednictvím interakce s komplexem G9a/GLP (G9a - euchromatic histone-lysine N-methyltransferase 2, EHMT2; GLP - euchromatic histone-lysine N-methyltransferase 1, EHMT1), který hraje významnou roli při methylaci histonů, konkrétně H3Kme1 a H3K9me2. Dále tento komplex může vázat transkripční factor WIZ (Widely-Interspaced Zinc Finger-Containing Protein) a tím současně regulovat umlčení jemu podřízených genů.

Abychom mohli studovat dopad mutace ZFP644 na vývoj myopie, vytvořili jsme myší modely, jeden mimikující lidskou mutaci - *Zfp644*^{S673G} a druhý se zkrácenou formou proteinu *Zfp644*^{Δ8}. Oba modely byly podrobeny důkladné vyšetření funkce a morfologie retiny. S využitím ultrasonografie, byly u těchto modelů odhaleny fenotypy v podobě poruchy retiny. Měření potvrdilo spojitost mutace *Zfp644* a myopie v obou modelech, navíc byly odhaleny vážné poruchy metabolismu a fertility samic u *Zfp644*^{Δ8} modelu. Pro detailnější popis vlivu *Zfp644* na plodnost byly provedeny experimenty zahrnující analýzu exprese *Zfp644* v reprodukčních orgánech, morfometrie vaječníků, sledování reprodukční aktivity a estrálního cyklu. Paralelně byly měřeny hladiny hormonů řídící estrální cyklus v každé jeho fázi, a na závěr byl sledován vývoj mléčných žláz v průběhu puberty a těhotenství. Tyto experimenty byly doplněny studiem organoidů mléčných žláz ze zmíněných myších modelů.

Pro hlubší pochopení regulace fertility, byly provedeny transplantace vaječníků z mutantních homozygotů do kontrolních jedinců a naopak. Podařilo se plně obnovit funkci vaječníků mutantních zvířat po jejich transplantaci do kontrolních zvířat. Homozygotní samice byly po transplantaci opět fertilní. Nicméně, u *Zfp644*^{Δ8} homozygotních samic k úplnému obnovení funkce nedošlo, samice zůstávaly subfertilní. K obnovení fertility mutantních samic, jsme experimentálně aplikovali hormonální terapii. To ukázalo, že lze obnovit fertilitu *Zfp644*^{Δ8} samic a dostat životaschopné mláďata za pomoci terapie progesteronem. Naše data dále ukazují, že *Zfp644* ovlivňuje homeostázu pohlavních hormonů v samicích a jeho mutace vede k neplodnosti.

Výzkum byl dále rozšířen o studium funkce WIZ proteinu v rámci G9a/GLP komplexu. Podobně jako v případě *Zfp644*, byl pozorován negativní dopad aberace *Wiz* genu v myším modelu. *Wiz* knockoutní myši umírají v pozdním embryonálním vývoji. Nicméně, umírají později než *G9a* nebo *GLP* knockoutní myši. Proto byly všechny morfologické změny mutantních myší studovány v embryonálních stadiích od E14.5 po E18.5. Mezi nevýznamější fenotypy patřilo zkrácení čumáku, rozštěp patra a očních víček. Dále jsme analyzovali metylace histonů pro bližší pochopení role *Wiz* proteinu v interakci s G9a/GLP komplexem. Na základě našich zjištění, lze odvodit že *Wiz* hraje důležitou roli v G9a/GLP methylačním komplexu, konkrétně ve vývoji kraniofaciálních struktur.

Tato práce představuje nová data, aplikovatelná pro další výzkum funkce a interakce ZFN644, WIZ proteinů a G9a/GLP komplexu. Vysoká podobnost myšího a lidského ZFP44 naznačuje translační potenciál myšího modelu. Je potřeba detailnějšího výzkumu methylačního komplexu G9a/GLP a jeho součinnosti s ZNF644 a WIZ proteiny. Nicméně věříme, že tato práce pomohla odhalit některé molekulární mechanismy studovaných proteinů.

Table of Contents

Abstract.....	5
Abstrakt	7
1. Introduction	11
1.1. Zinc finger protein 644.....	11
1.2. Binding partners of ZNF644	14
1.2.1. WIZ.....	14
1.2.2. G9a/GLP complex	15
1.3. Histone methylation	18
1.4. Disease related to Zfp644 mutations.....	21
1.4.1. Myopia.....	21
1.4.2. Female infertility and health status during pregnancy.....	22
2. Aims of the study	28
3. Materials and methods.....	29
3.1. Experimental approach.....	29
3.2. Mouse models generation.....	30
3.3. Microscopy and expression analysis	31
3.4. <i>In vivo</i> experiments for vision analyses	34
3.5. <i>In vivo</i> methods for fertility and metabolism studies	36
3.6. Embryonic studies	41

4. Results	42
4.1. Mouse models introduction and verification	42
4.2. Expression analyses	45
4.3. Physiological role of Zfp644 and Wiz mutations on mice and extended analyses of metabolism	47
4.4. Role of Zfp644 in high myopia	56
4.5. Role of Zfp644 in mouse fertility	65
4.6. Role of WIZ in embryonic development	79
5. Discussion	84
5.1. Main results of the thesis	84
5.2. The role of Wiz protein in G9a/GLP complex	91
5.3. Troubleshooting	92
6. Summary	95
Publications and author contributions	96
List of Abbreviation	107
List of Figures	108
List of Tables	110

1. Introduction

1.1. Zinc finger protein 644

Zinc finger protein 644 is a protein encoded by the ZNF644 gene in human, located on chromosome 1; or the Zfp644 gene in mouse, located on chromosome 5. ZNF644 has two isoforms, from which the longest is the main focus. Zinc finger protein 644 is ubiquitously expressed in tissues (both human and mouse). It is known to be a transcription factor. Location of the protein is in the nucleus [www.ncbi.nlm.nih.gov].

The protein is quite large, containing of over 1300 AA. It contains 8 zinc finger binding motifs from which one is atypical. It has an ability to bind to a TAD domain (A topologically associating domain) by its N-terminus site (G9a binding¹). The secondary structure of the protein remained highly unknown for a long time. It is predicted to be in highly intrinsic disordered state (Fig.1.1). To simplify, this means that the protein does not usually have one, fixed 3-D structure, in the absence of their binding partners. The intrinsic disorder protein can be full or partial, as in case of ZNF644. Many of these proteins can fix their structure when bound to an interacting partner (proteins, RNA etc.) to fulfil their biological function.

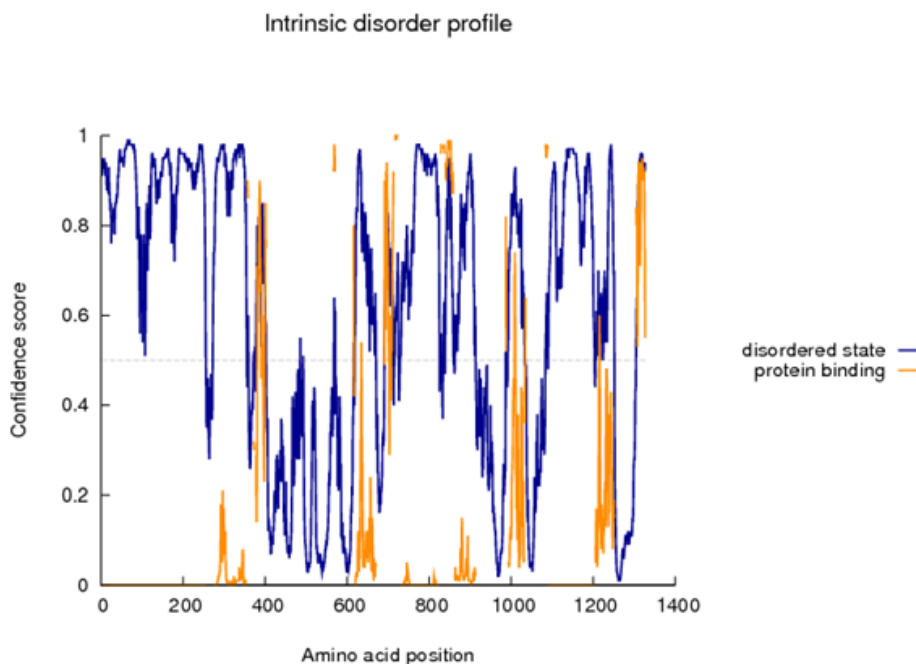


Figure 1.1. Intrinsic disorder profile of ZNF644 protein created with RaportX software,²⁻⁴

Recently the structure was revealed in AlphaFold database however with low confidence in large parts of the sequence, due to a lack of similarity with other, known structures. To complement this study by 3-D modeling, we analyzed the AlphaFold database (Fig.1.2.). Parts with higher confidence, mostly corresponds to protein binding regions presented on Figure 1.1. and predicted C2H2 domains [uniprot.org]. The disordered state was mostly predicted with low confidence.

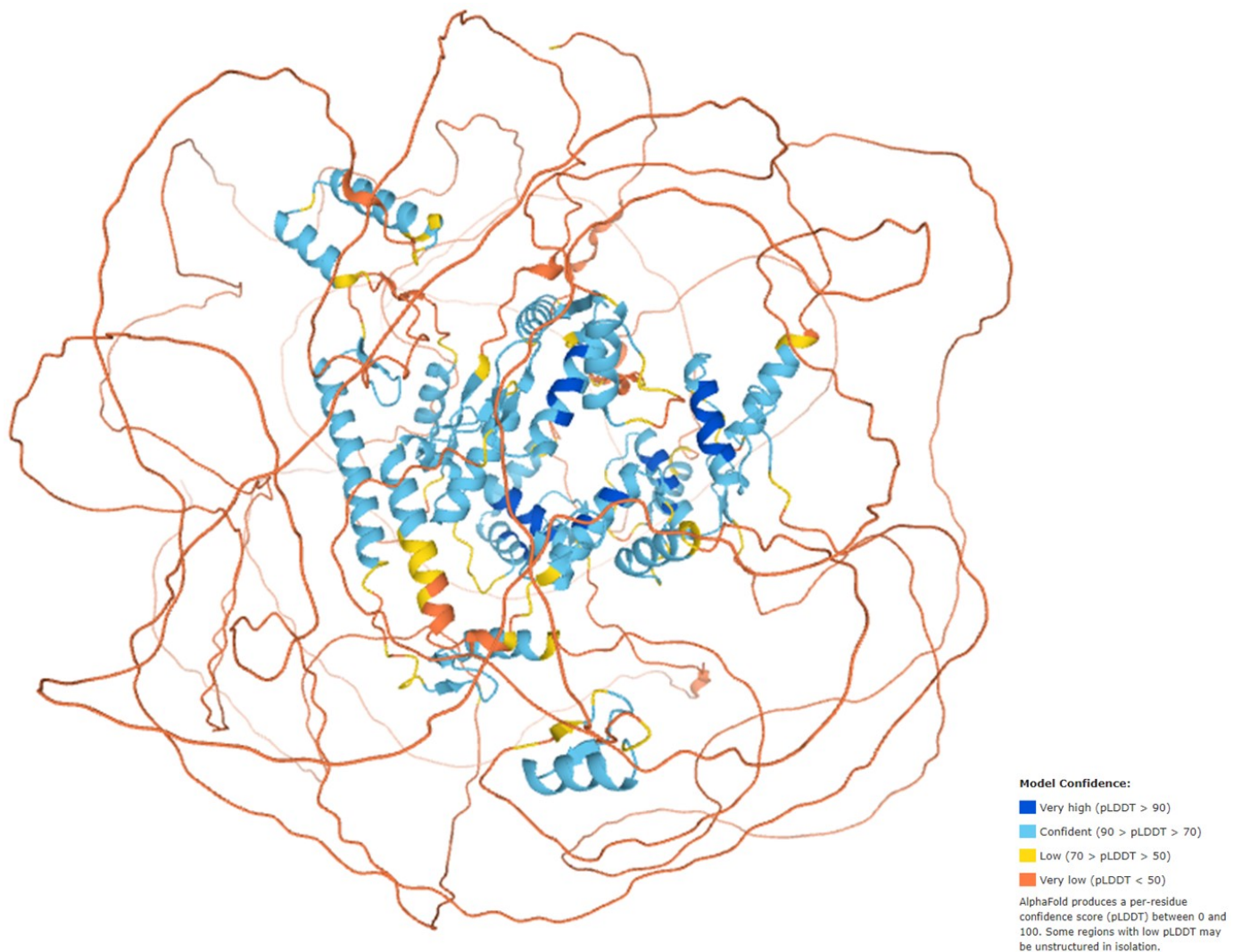


Figure 1.2. 3D model of full length Zfp644 protein; analysis were done with AlphaFold database ⁵

So far not much is known about the function of ZNF644. The first systematic description of ZNF644 function in humans were analyses from a GWAS study (A genome-wide association study) that found multiple point mutations in *ZNF644* gene, predicted to be causative of high myopia. In total 12 point mutations in humans were found and described⁶⁻¹⁰ (Fig.1.3.). Interestingly, most of them are located in 3rd exon. Among them, presented in the red rectangle, is a point mutation S672G, which became our focus in the vision study described in detail in further chapters.

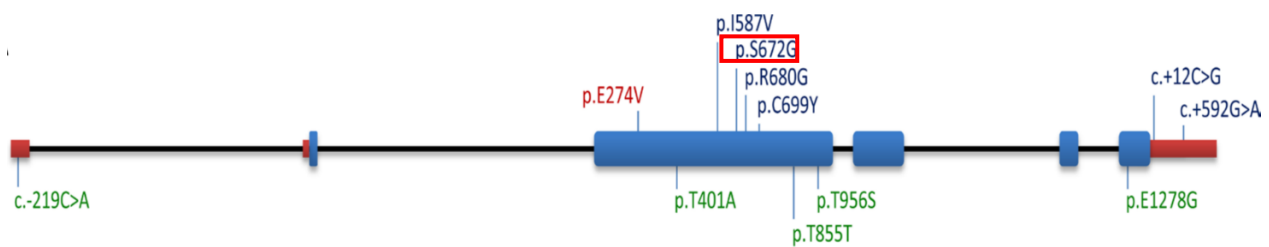


Figure 1.3. Mutation spectrum of *ZNF644* in patients with high myopia up to now. Mutation locations in the *ZNF644* DNA sequence. The mutations colored blue were found by Shi et al., the mutation colored red was identified by Tran-Viet et al., and the mutations colored green were identified in this study. Xiang et al. 2014

Further studies on ZNF644 brought interesting insights based on a cell work. Two publications mentioned ZNF644 as an important player of G9a/GLP methylation machinery^{11 1}. In HEK293T cells, knockdown of ZNF644 reduces proliferation. It also make the cell more sensitive to replication stress and increases DNA damage in replicating cells. It was also shown that ZNF644 in complex with G9a is present in Active Replication Forks¹¹. It was proven that ZNF644 in complex with G9a/GLP consist of one more protein that simultaneously bind to GLP, called WIZ. It is a transcription factor, previously described as a binding partner of G9a/GLP complex. It was proven that both WIZ and ZNF644 bind to G9a/GLP complex and are targeting it to specific DNA loci that are crucial for the regulation of G9a function during replication.¹ Further studies of ZNF644 in complex with G9a/GLP were conduct in zebrafish. Experiments on the morphants proved that ZNF644 with the G9a/GLP complex are responsible for histone methylation and are crucial for gene silencing during retinal neuronal differentiation¹².

1.2. Binding partners of ZNF644

1.2.1. WIZ

Wiz is a ubiquitously expressed transcription factor, described as a binding partner of G9a/GLP already in 2006¹³. Two spliced variants of WIZ were identified, WizS and WizL. The name, Widely-Interspaced Zinc Finger-Containing Protein, has its source in the protein architecture. WIZ protein contains 12 Zinc Finger motifs. Usually, C2H2 – type zinc finger motifs are separated by seven amino acids, however in Wiz protein, this distance is in a range from 16 to 258 amino acids, and up to 263 in the longest human variant¹⁴.

WIZ was also described as a factor important for G9a protein stability, with ability to bind both G9a and GLP proteins. Binding to GLP is direct and occurs between the C-terminus of WIZ and the TAD domain; binding to G9a occurs with the catalytic domain¹ (Fig.1.4.). The same domain is necessary for GLP – G9a binding, therefore, binding of WIZ to G9a seems to be indirect. WIZ knockdown leads to an H3K9me2 loss, but not as a result of GLP or G9a protein degradation. WIZ was also reported to be important for the retention of G9a on chromatin¹⁵.

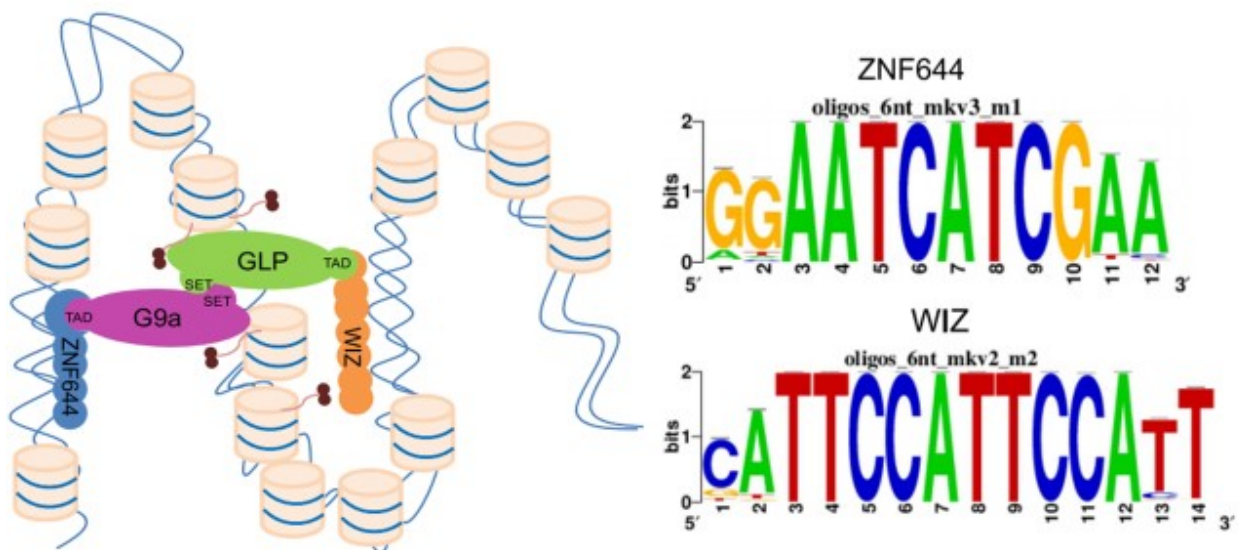


Figure 1.4. ZNF644 and WIZ binding through TAD domains to G9a and GLP respectively. The consensus DNA binding motif of ZNF644 and WIZ proteins ¹

WIZ was reported as a potential docking molecule to link G9a/GLP HMTases (histone methyltransferases) to CtBP (C-terminal-binding protein) – co repressor machinery¹³. CtBP is known as a transcriptional co-repressor, important for development and ontogenesis, and was shown to interact with various transcriptional molecules. A knockout mouse model of *Wiz*, *Wiz^{mommeD30}* was proposed in 2013 and described as an early embryonic lethal model¹⁶.

To complete our study, we decided to expend the analysis by a complementary project to understand the role of WIZ protein in the G9a/GLP complex by creating *Wiz* knockout mouse with use of CRISPR/Cas9 technology. The results of experiments can be find in Results Chapter.

1.2.2. G9a/GLP complex

Histone lysine methylation is one of the crucial histone post translational modifications. Suv39h1, the first described histone lysine methyltransferase (HKMT) including a SET domain (Su(var)3-9–Enhancer of zeste–Trithorax domain) (Fig.1.5.), was just a beginning for further research in histone methylation.¹⁷ In mammals, primary HKMTs are EHMT1 and EHMT2, responsible for mono-, and demethylation of Lysine 9 on histone 3 (H3K9me1, H3K9me2). This highly similar proteins exist predominantly as a G9a–GLP heteromeric complex (Shinkai). Loss of either of them results in a high decrease in either mono- or demethylation of H3K9 (Tachibana, Peters, Rice). Both genes are ubiquitously expressed in human and mouse. G9a was recognized also for methylation of H1 and other non-histone proteins, including itself^{18,19 20 21 22}. Binding of H3K9me1 and H3K9me2 products of G9a and GLP occurs via ankyrin repeat domains^{23,24}. The domains contain a hydrophobic cage present in methyllysine binding modules of diverse folds, which serves well for binding H3K9me1/2, but not H3K9me3.

Knockout mice were analyzed for both GLP and G9a and both were diagnosed with pre weaning lethality (<https://www.mousephenotype.org/data/genes/MGI:1924933#phenotypesTab>; <https://www.mousephenotype.org/data/genes/MGI:2148922#phenotypesTab>). Moreover, studies on mice knockout cells showed, that depletion of one of the enzymes results in degradation of the remaining partner protein^{25 26}. Restructuring of these cells with a complex consisting of either G9a or GLP catalytic mutant showed, that the catalytic activity of GLP, but not G9a, is dispensable for methylation²⁵. Cells with knockout of GLP or G9a lost their DNA methylation activity and binding to euchromatin²⁵⁻²⁷.

Both EHMT1 and EHMT2 are ubiquitously expressed and are a major complex responsible for H3K9 mono- and demethylation. The role of G9a and GLP in various biological systems was proposed. As explained above, they play a crucial role in mouse development. Moreover, G9a seems to play a role in imprinting of some genes^{28 29}. Further roles in germ cells development and meiosis, brain function, drug response or immune response was described³⁰. The most widely studied role of G9a/GLP complex is tumorigenesis. Multiple evidences pointed its role in different types of tumors, e.g. lung, breast, bladder, colon, cervical, gastric, skin cancers, hepatocellular carcinoma and hematological malignancies³¹. The mechanism behind G9a role in cancer development is based on epigenetic dysregulation. Increased methylation caused by G9a upregulations results in the downregulation of significant tumor suppressor genes in various cancers³².

G9a and GLP enzymes are involved in a variety of biological processes and demonstrate both co-activator and co-repressor function^{23,24,30,33}. They interact with other SET –domain proteins, such as SETDB1, Suv39HI and PRC complex^{34 35}. The protein structure and domain organization of both G9a and GLP is crucial for their specificity for H3K9. Thanks to selective recognition of the residues flanking K9 in the histone H3 N-terminal tail they are able to fulfil their role in histone methylation³⁶. Post-translational modifications of residues proximal to Lysine 9 in histone 3, such as R8me, S10ph, T11ph abolish methylation by G9a, whereas modification distal to K9 has no effect on specificity of G9a^{20 18}. The ankyrin domains of G9a and GLP also play a role in H3K9 methylation. They function via a *trans* mechanism of interactions between ankyrin domains of G9a and GLP and existing H3K9me1 or H3K9me2 that recruits these enzyme to chromatin and direct the methylation of unmodified H3K9 in adjacent nucleosomes. In conclusion, these findings illustrate distinct mechanisms by which the methyllysine binding domains of G9a and GLP target these enzymes to chromatin substrates. The described domain organization of G9a and GLP can be appreciated on the presented figure (Fig.1.5.).

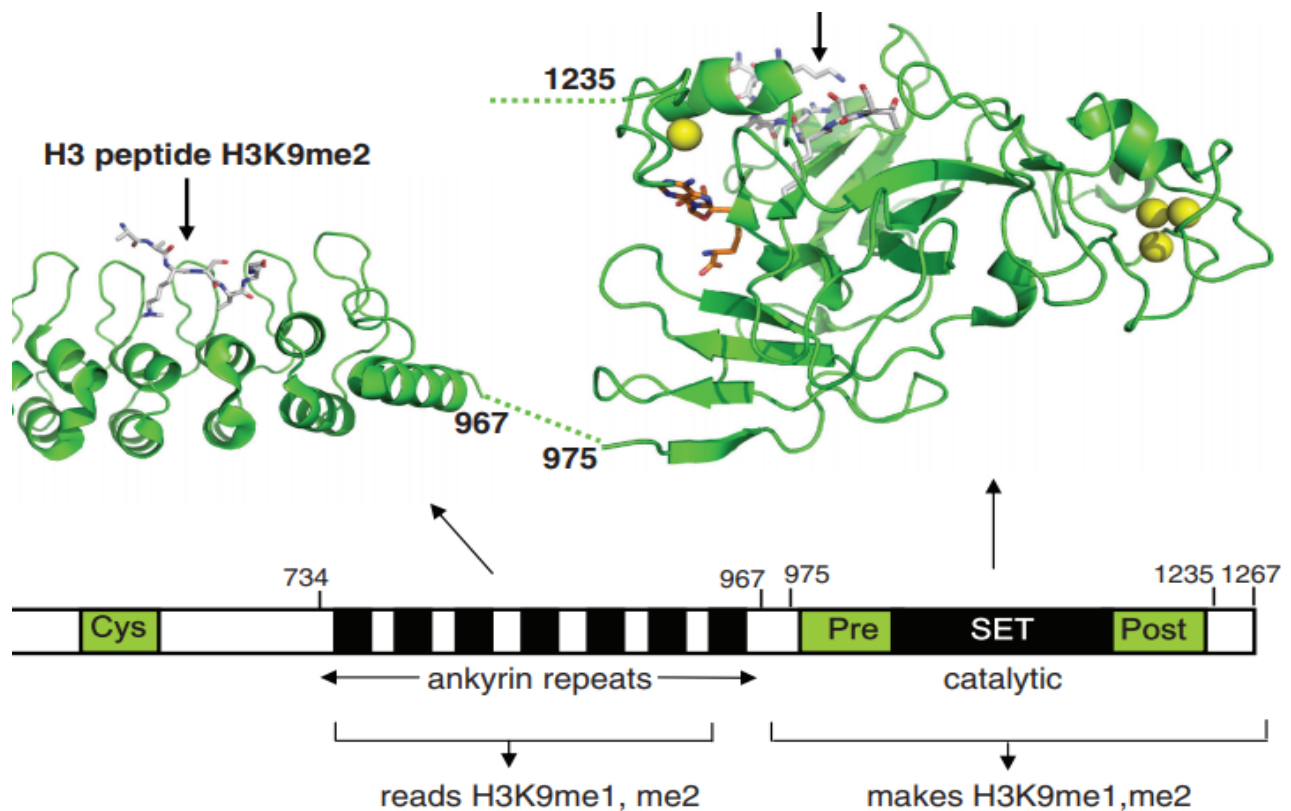


Figure 1.5. Graphical explanation of domains organization in G9a and GLP, Collins R et al. 2010

Although crucial, G9a and GLP proteins lack the DNA recognition motifs to target specific genes. However, two proteins described in previous chapters, ZNF644 and WIZ were reported to lead the G9a/GLP complex to specific target loci. Very likely, they function together to recognize specific DNA sequences. Double recognition may stabilize and precise the histone methylation in a specific loci¹.

More partners of either G9a, GLP or complex in general were described. Among the others, DNMT1, that plays a role in the histone methylation together with G9a. Many nonhistone substrates that are methylated by G9a/GLP were described, including p53 (K372), Wiz (K305), CDYL1 (K135), ACINUS (K654), and Reptin (K67)^{20,22,37,38}. As described by Shinkai et al. many other molecules have been reported as partners of G9a. Most of them are either repressive chromatin protein or multi zinc finger protein³⁰. An interesting example seems to be a STAT3 transcription factor, another described partner of G9a³⁹⁻⁴¹. STAT3 is a member of the STAT protein family. It responds to cytokines and growth factors, is phosphorylated by Janus kinase

(JAK) and then translocates to the cell nucleus where it acts as a transcriptional activator. Recently STAT3 was described as a player in female reproductive tract⁴²⁻⁴⁴ and reproduction^{45,46}.

1.3. Histone methylation

Each human cell has almost two meters in length of DNA, if it would be completely stretched out. Thanks to histones, and more specifically the way DNA can be wound about them, the actual size is as little as 90 μm ⁴⁷. Histones are divided into five families and two groups: linkers (H1, H5) and core (H2, H3, H4). Histones undergo many PTMs (post-translational modifications) regulating the structure and functions of chromatin. Histone methylation is involved in DDR (DNA damage response), regulated by histone methyltransferase or histone demethylase⁴⁸. Common histone mark, histone methylation is an addition of methyl group (-CH₃) to an arginine or lysine amino acid residue^{49,50}. Both lysine and arginine can be methylated (me) by adding one (mono, me), two (di, me₂) or, only in case of lysine, three (tri, me₃) methyl groups. Moreover, to arginine groups (me₂) can be added symmetrically (me₂s) or asymmetrically (me₂a). The situation is visible on the scheme below (Fig.1.6.). Currently, HMTs are divided into three groups, however as the purpose of this literature review we will focus on enzymes that include SET domain.

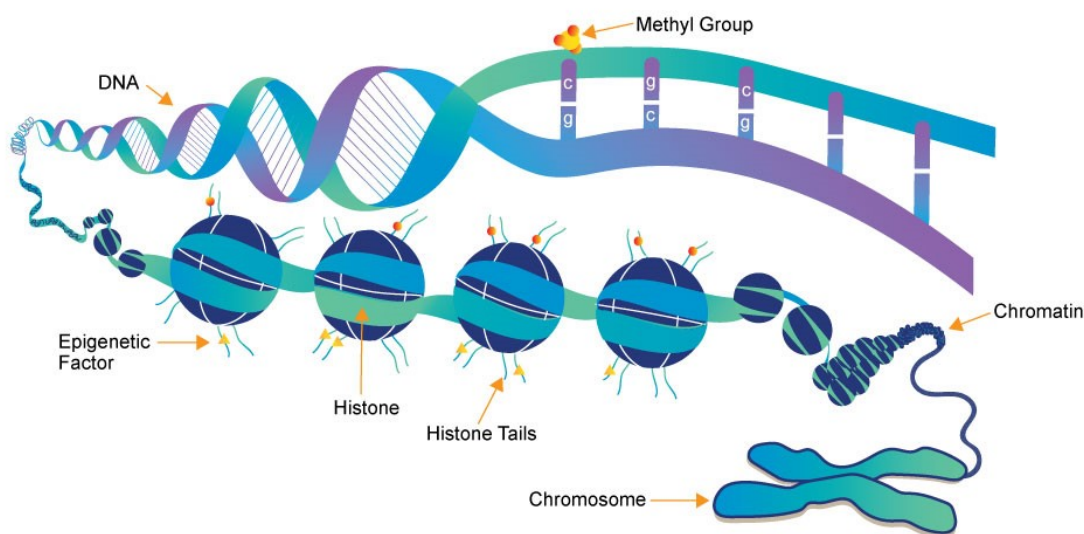


Figure 1.6. Schematic representation of chromatin structure as well as histones and DNA available to epigenetic marks. www.whatisepigenetics.com

When describing H3K9me2 and H3K9me3 in mammalian system, large broad domains cannot be omitted, as they are often found there^{51 52 53}. H3K9me2 domains, or LOCKs (Large Organized Chromatin K modifications), conserved between mouse and human, emerge and spread upon differentiation and a majority depend on G9a⁵³. LOCKs might play a role in regulating the expression in differentiated cell types. Many genes contained in these domains are developmentally regulated⁵⁴. Moreover, Lamin B1 might be involved in these processes through lamin-associated domains (LADs)^{53,55} and correlated with LOCKs and further with H3K9me2 in C-elegans⁵⁶ suggesting, that H3K9me2 domains may be important determinants of higher order chromosome structure and nuclear architecture. The data taken together suggest, that H3K9 through the large domains, might be an important determinant of 3D nuclear architecture and chromatin arrangement in nucleus.

Histone methylation plays a crucial role in genomic functions⁵⁷. In particular, histone lysine modifications have a great impact on various chromatin-associated functions, for example transcription regulations, heterochromatin formation and DNA repair or recombination^{57,58}. Histone lysine methylation controls protein (histone) – protein interactions, each methylated lysine residue of H3 or H4 recruits different functional molecules involved in different chromatin-associated processes¹³. The most studied and described are histone modification to H3, therefore in this review, we will focus on H3K9 methylation, the main target of G9a/GLP and concurrent, ZNF644. Regularly H3K9 is methylated by proteins contains the SET-domain, as described above G9a and GLP proteins or SUV39H1, SETDB1 or PRDM2. H3K9 methylation plays a crucial role in heterochromatin formation and heterochromatic gene silencing^{59 60}. It is also an important histone mark in DDR. Epigenetic regulations have a great impact on many biological system therefore, for purpose of this review, we will focus on the role of methylation in development and fertility.

Histone methylation in animal development plays an incredibly important role. Any arrest or unspecific behavior of this epigenetic process can result in very severe developmental malformations and lead to problems in organs in mature animals or caused embryonic lethality. Histone 3 methylation on different lysine residues is widely connected and supported by studies, with many diseases. An example could be Kleefstra syndrome (KS; OMIM 610253) which is characterized by intellectual disability, childhood hypotonia, and distinctive facial features^{61,62}. Another examples is Siderius X-linked mental retardation syndrome (MRXSSD; OMIM 300263) - an X-linked intellectual disability condition. Patients display mental retardation, a long face and broad nasal tip, and cleft lip and palate which are connected to H3K9 methylation^{63,64}. Another example can be H3K9me3 showed to be responsible for the earliest embryonic lethality, occurring before embryo implantation⁶⁵, however, both mono- and demethylation of histone 3 lysine 9 imprecisions might result in embryonic lethality. Histone methylation marks are generally ubiquitously expressed, however, studies have shown that there are certain cell-type-specific and tissue-specific differences in the activity of histone methylation regulators⁶⁶. As in adult organism and in different biological systems, H3K9 methylation is also responsible for gene silencing in embryonic development. As already described, H3K9 gene silencing is physically associated with nuclear lamina, which suggests the occurrence of progressive heterochromatinization during development and lineage specification.

Histone methylation plays also an important role in the development of reproductive system. *Kdm3a*, H3K9 demethylase knockout results in fraction of XY mice to develop into females⁶⁷. Moreover, *Suv39h1* and *Suv32h2* double knockout result in deficits in spermatogenesis⁶⁸. Liu⁶⁹ have demonstrated that H3K9 histone methylation tightly controls oocyte growth, a necessary step for further correct follicle maturation required for female fertility. Studies on histone methylation were performed also on patients with infertile polycystic ovary syndrome (PCOS). The syndrome features an imbalance in luteinizing hormone (LH), follicle-stimulating hormone (FSH) and some factors involved in the inappropriate progression of folliculogenesis, and arrest of the follicle development toward the dominant stage⁷⁰. Analysis of H3K9me2 marks showed a correlation between differential occupancy of methylation in cumulus cells of PCOS patients when compared with control group as well as promotion of different binding of ER- β ⁷¹.

1.4. Disease related to Zfp644 mutations

1.4.1. Myopia

Myopia is the most common vision disease, despite the fact that scientists warned about near work without sufficient pauses already more than 400 years ago⁷². It is predicted to affect up to 5 billion people by year 2050⁷³. Currently it affects as much as 90% of high school students in East Asia⁷⁴⁻⁷⁶. Myopia is a disease caused by a refractive error based on elongation of the axial length of eyes⁷⁷⁻⁷⁹ (Fig.1.7.). In a normal, healthy eye, the light is focused on retina. In myopia, the eye is enlarged and the light is not able to reach retina. It means, that close object appears normal, but objects in the distance appear blurry. Therefore, another, common name of myopia is near-sightedness. The disease often progresses with age however the symptoms can be relieved by spectacles, contact lenses or refractive surgery. Nevertheless, myopia might improve the risk of other severe diseases, like retinal detachment, myopic macular degeneration, cataracts or glaucoma and even lead to blindness associated with high myopia⁸⁰⁻⁸³.

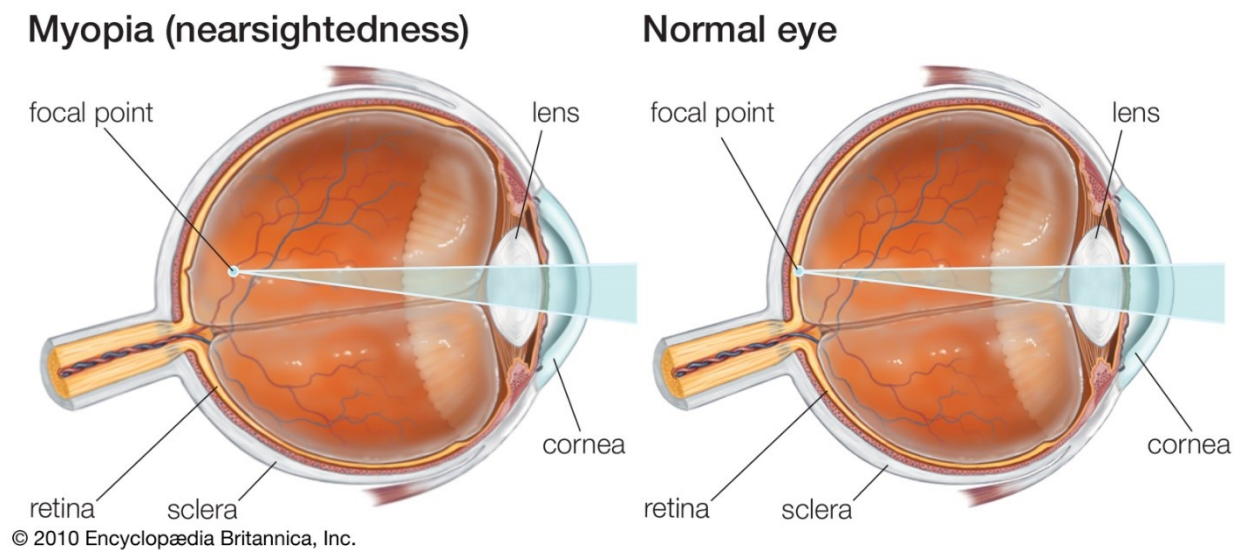


Figure 1.7. Comparison of normal and myopic eye. Britanica.com

Myopia can be divided into Primary, Secondary and Pseudomyopia. Primary myopia can be further branched to simple myopia (D from -0,5 to -7,75) and high myopia ($D \geq -8$)⁸⁴. Myopia might be caused by environmental factors but also by diet or even the education level^{74,81,85-87}. Many cases of the disease has a genetic background. To date more than 100 genes in 20 loci were identified to be associated with myopia or related by experimental analysis in GWAS studies, NGS or candidate genes analysis⁸⁸⁻⁹¹. Parental myopia studies showed, a significant association with occurrence of myopia, especially high myopia, in children⁹². Also, large twin studies showed high (~90%) heritability of myopia^{93,94}. Nevertheless, the current state of knowledge of genetic mechanisms of myopia development is very limited. High heritability and high prevalence to myopia in different populations shows the importance of studying the genetic background and impact of the disease. The mechanism of the disease is very complicated and only few individual genes were proven as predisposition of myopia in individuals⁹⁵. Therefore, even more important for understanding the disease, seems to be research on animal models. To date scientists still use induced myopia (e.g. with goggles). Genetic models are very limited. By now, besides the models created by us Zfp644 transgenic mice, only 4 mouse models are being used in myopia studies^{79,96-101}.

Nevertheless, at the time of writing, the COVID-19 pandemic and the related so called “lockdown” or a quarantine around the world might also have very strong influence on number of myopia patients in the future. Due to a higher number of activities like reading, watching TV or playing video games and other near work that requires overstimulating accommodative effort might represent a greater risk of myopia for individuals with accommodative defects¹⁰². This shows that research on prevention but also on factors causative to myopia is very important.

1.4.2. Female infertility and health status during pregnancy

The female reproductive system is made up of internal (uterus, fallopian tubes and ovaries) and external organs (genitals). Ovaries are the source of ova (eggs) and sex hormones: progestogens and estrogens. Through the fallopian tubes the ovaries are connected with the uterus. The uterus is a muscular organ, with a granular lining called the endometrium. The endometrium is responsible for correct implantation of a blastocyst and further it creates the placenta. For the correct functioning of the female reproductive system the influence

of hormones cannot be underestimated. The secretion of hormones in hypothalamus and pituitary is as important as releasing of sex hormones in ovaries. Only precise hormone secretion during the estrus cycle and pregnancy leads to successful birth and manger (Fig.1.8.).

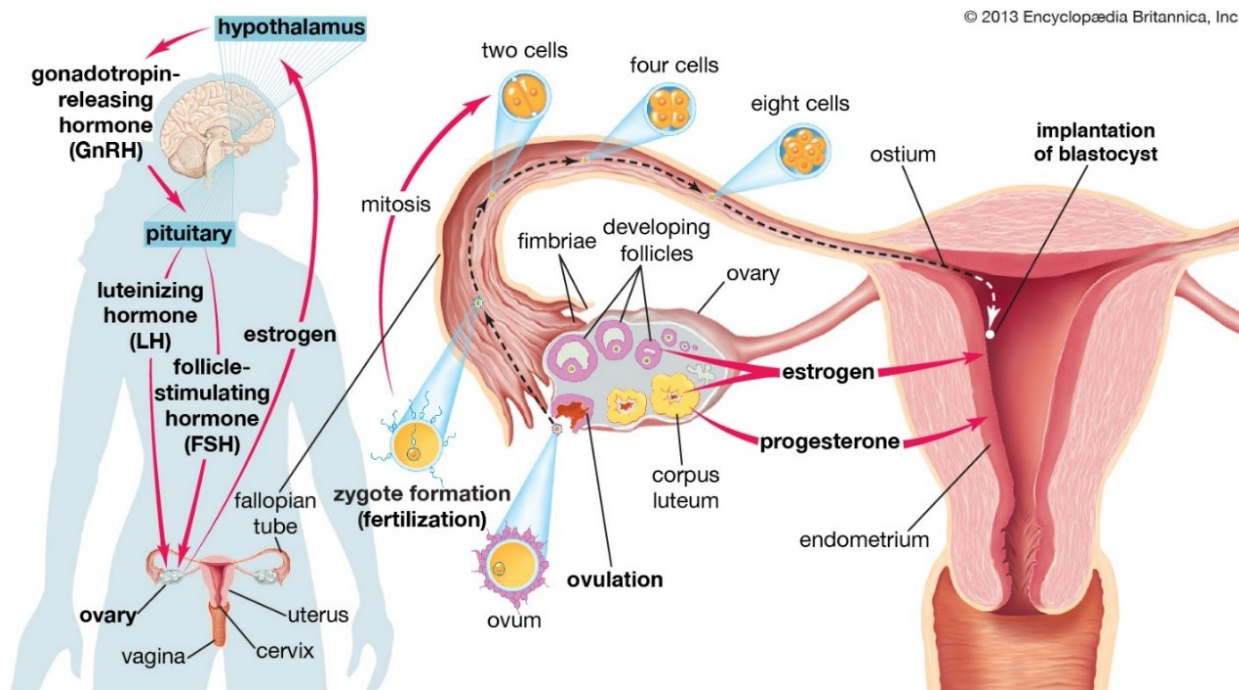


Figure 1.8. Schematic explanation of female reproductive system, Britanica.com

The female gonads, two ovaries, contains ovarian follicles, with primitive ovum or oocyte in their center. From the hundreds of thousand follicles, which a girl is born with, most degenerate in childhood or after puberty. From puberty, cyclically, one or more follicles mature. The crucial role in this process is played by hormones. Respectively, follicle-stimulating hormone (FSH), luteinizing hormone (LH), estrogens and later on also progesterone and prolactin. The liberation of the ovary is called ovulation and, together with formation of the polar body, it is necessary for successful fertilization.

In mouse, the estrous cycle is also observed. Unlike in human, it takes only 5 days. Hormone circulation play a crucial role in maturing of the follicles and changes during the estrus phases (Fig.1.9.). The main hormones involved in estrus cycle in mouse are LH, FSH, Progesterone, Prolactin and 17- β -estradiol. Irregularities in secretion of any of the hormones

results in disruptions in estrus cycle and might lead to semi – or infertility in females. Moreover, distortion in levels of ovarian oestrogen and progesterone might lead to implantation failure.

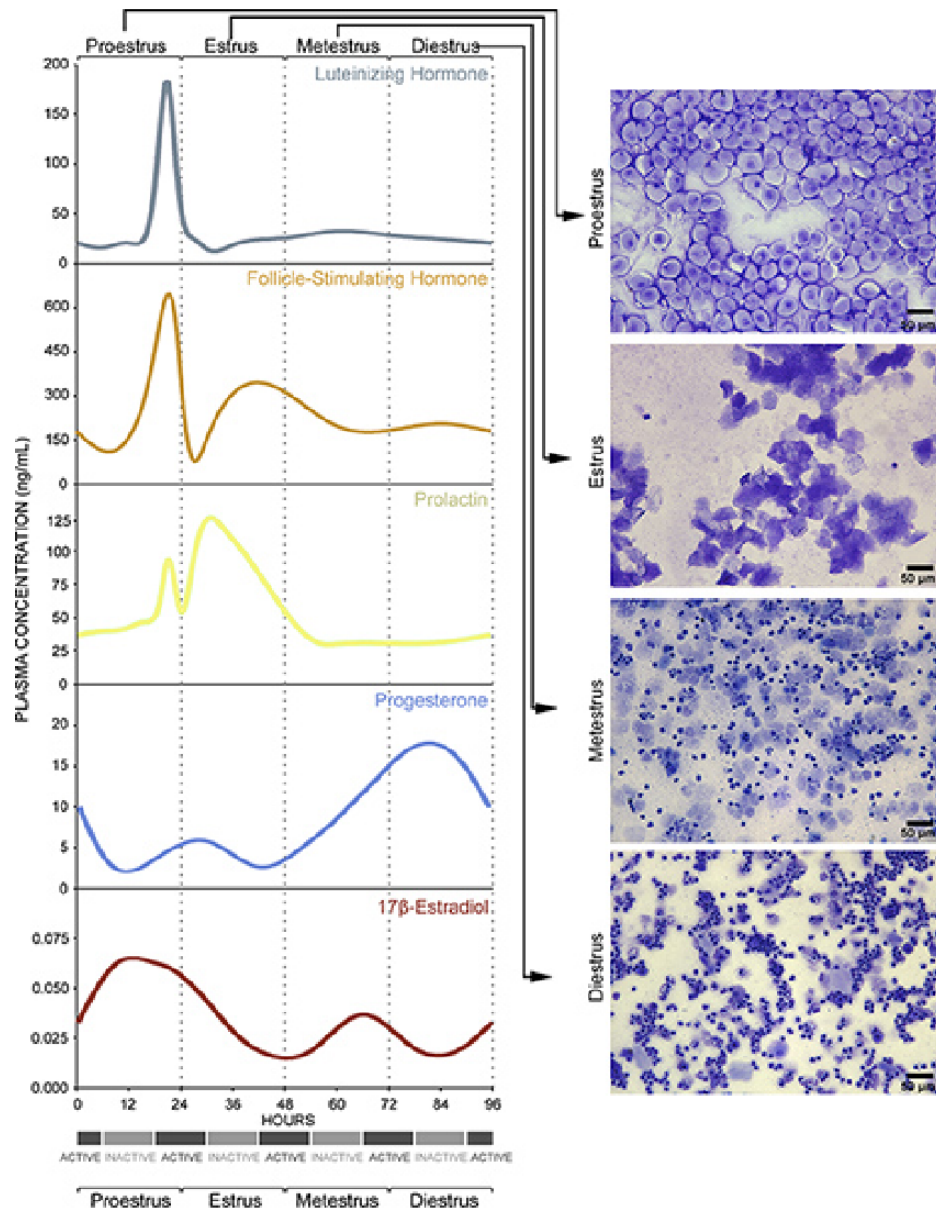


Figure 1.9. Vaginal smear cytology reflects underlying endocrine events. McLean AC, Valenzuela N, Fai S, Bennett SA. Performing vaginal lavage, crystal violet staining, and vaginal cytological evaluation for mouse estrous cycle staging identification. J Vis Exp. 2012 Sep 15;(67):e4389. doi: 10.3791/4389. PMID: 23007862; PMCID: PMC3490233.

Hormonal circulation during puberty, estrus cycle or pubertal influence also the mammary gland (Fig.1.10.). It is not part of the reproductive system however an indispensable organ, especially during pregnancy and manger periods. Its incredible function to nourish and immunologically support new borns becomes possible also through hormonal signaling. Mammary gland development in mouse starts already during embryonic development¹⁰³. It continues with puberty (in mouse around 4 weeks of age), and is highly dependent on ovarian hormones, pituitary hormones and local growth factors and cytokines¹⁰⁴. Mammary gland development during puberty starts with accelerated elongation of ducts and branching. At this time we can observe terminal end buds (TEBs) as large club-shaped structures at the tip of duct. They contain both body cells and cap cells. TEBs are highly proliferative and drive the ductal tree extension, what will further create a transport channel for milk at lactation¹⁰³.

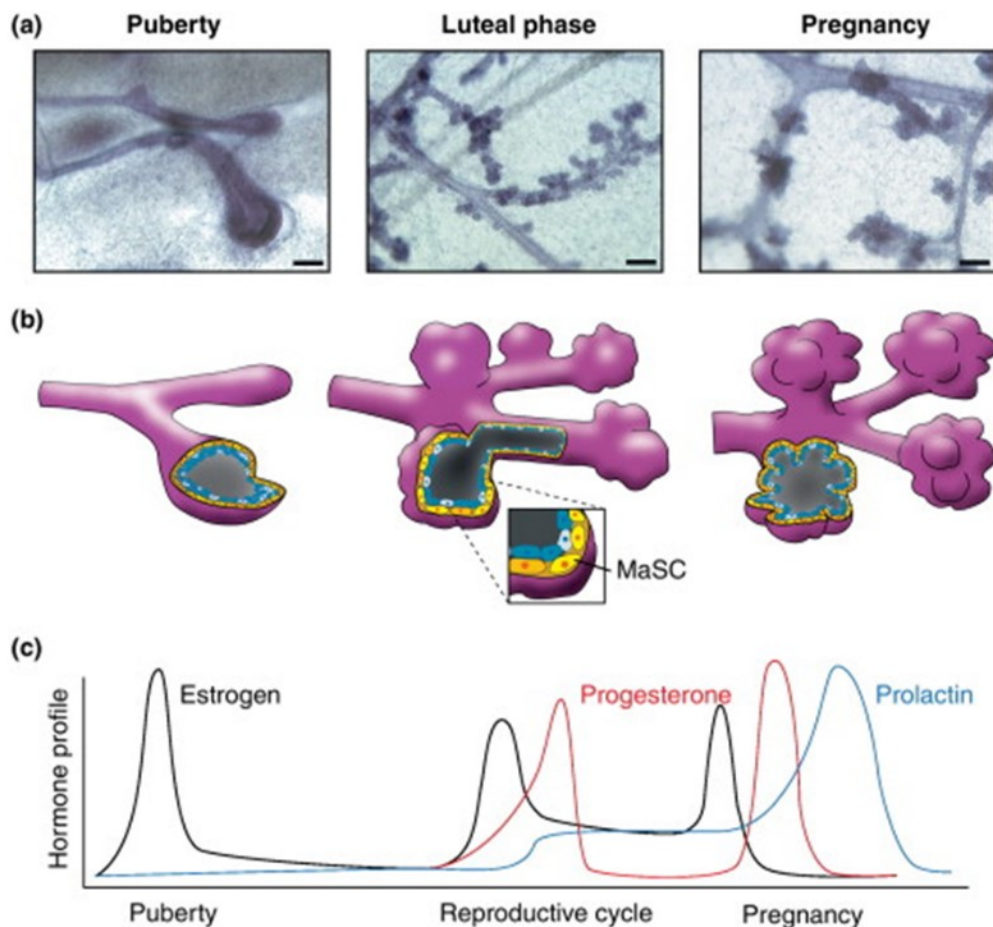


Figure 1.10. Representative comparison of lactiferous ducts morphology and hormonal profile in different stages in female mice. Joshi PA et al.; Trends in Endocrinology & Metabolism; 2012

During the pregnancy, cells undergo numerous divisions. Also during this stage hormones play a crucial role. Not only estrogen and progesterone release by corpus luteum but also by placenta seems to be crucial at the beginning of pregnancy. The next players are the pituitary hormones prolactin and adrenocorticoids from adrenal glands. Functional differentiation is completed at parturition when milk is being produced and secreted during lactation. This process is tightly controlled by balanced progesterone and prolactin signaling¹⁰⁵. Receptors are also necessary for correct growth of the glands during the pregnancy. Progesterone receptors are necessary for the ductal growth¹⁰⁶⁻¹⁰⁸ and prolactin receptors for lobuloalveolar differentiation and lactogenesis^{106,107}. After weaning cells undergo involution and mammary glands are back to a much resembled virgin – like morphology^{109,110}.

Among the others, two important factors involved in described above hormonal regulation and mammary gland function need to be addressed in this literature review. One of them is the already described G9a protein. As mentioned before, the epigenetic regulations of H3K9 have an influence on hormonal regulations. Independently of histone methylation, G9a acts as a coactivator of endogenous oestrogen receptor α (ER- α)¹¹¹. G9a influences also mammary ductal tree formation and the loss of H3K9 methylation was shown to result in loss of tissue function¹¹². G9a is highly correlated with STAT3 protein. STAT3 – G9a crosstalk was repeatedly described, especially in cancer research. STAT3 and G9a was not only described in HER3 positive cancer⁴⁰, but also with breast cancer⁴¹, where another factor in the pathway, LEPR, was introduced³⁹. Moreover, when analyzing the impact of STAT3 in reproduction and fertility, it is worth to mention a study reporting STAT3 and PR crosstalk is required for successful implantation in the mouse uterus¹¹³. The STAT3 protein function in reproductive tract of females was shown to be a transducer of signaling by hormones, growth factors and cytokines identified in the female reproductive tract from oocytes and granulosa cells of the ovary to uterine epithelial and stromal cells. Its significant impact on uterine stromal cells, causing a significant reduction in number of viable fetuses on gestational day 18, increased fetal resorptions and disrupted placental morphology was identified as evident causes of the reduced fertility⁴⁵. Interestingly, STAT3 and its inhibitor PIAS3 seems to be a major factor included in endometriosis, an inflammatory disease of endometrium¹¹⁴, and both were found to interact with ZNF644 (PIAS3) and G9a (STAT3) in a ChipSeq studies on HEK293T cells¹.

In case of a failure in any of the mentioned systems (development of reproductive system or mammary gland, hormone release or follicle maturation) the ability to get pregnant and successfully carry the pregnancy to live birth might decrease or become impossible. Infertility is an inability of a couple to conceive and reproduce. It is also defined as the inability of woman to carry the pregnancy to live birth. This problem affects 10% to 15 % of population (Britanica). Subfertility can be used as a synonym to fertility¹¹⁵, or as a term defining any form or grade of reduced fertility¹¹⁶. Normal female fertility depends on correct implantation of the fertilized ovum and further maturation of embryos in utero. The process, from the very beginning, is highly affected by multiple factors, like alcohol, tobacco or drug abuse, sexually transmitted disease or general medical history. The main cause of female infertility is ovulation failure and further causes include tubal damage, endometriosis, cervical mucus defects or dysfunction and uterine abnormalities¹¹⁷. However, we cannot forget that not only correct development of reproductive system is necessary for fertility. At the foundation of female fertility the egg was laid, matured and correctly secreted. Endocrinology of female fertility was investigated already over 40 years ago¹¹⁸. The data showed that failure of any of the menstrual cycle components will lead to ovulation failure and hence infertility. Normal follicular and luteal phases, divided by ovulation, prepare the female organism for a successful fertilization¹¹⁹.

Progress in the reproduction field was made in last two decades and multiple examples of studies based on mouse models can be presented. Numerous genetic malformations were found to be causative of infertility in mice when researchers were able to analyze over 400 mouse models¹²⁰ in relation to fertility. Thanks to progress in sequencing, 25 inbred mouse strains were analyzed for SNPs related to infertility in female mice¹²¹. Genome-wide associated mapping of female infertility in inbred mice was analyzed. A majority of SNPs found in genes were related to signal transduction, developmental processes and cell organization and biogenesis. Among the others, a study showed *Sorbs1* as a candidate gene for female infertility and further analysis showed its possible correlation with early pregnancy loss.

Now, many forms of treating the female fertility have been proposed; from hormonal treatment to IVF (*in vitro* fertilization) and ART (Assisted reproductive technology). Nevertheless, there is a rapidly growing demonstration of predisposition of infertile woman, or woman with infertility –associated diagnosis, to develop other health problems¹²², exhibiting a further need of female fertility research.

2. Aims of the study

ZNF644 is a transcription factor, working with the G9a/GLP methylation machinery. Until now, a detailed role of ZNF644 has not been described. Limited studies on ZNF644 have been carried out and pointed towards it being a potential factor in human high myopia. Here, we try to reveal not only the impact of Zfp644 in mouse vision and high myopia but also its biological function using *in vivo* models. We were next trying to reveal the role it plays in cooperation with G9a and the molecular mechanism behind it. We decided to complement our study by additionally describing WIZ and its role in the G9a/GLP methylation complex.

Aims were set as followed:

- **Clarify the role of Zfp644 in the development of myopia disease in vivo using murine models.** GWAS studies were systematically reporting mutations in ZNF644 protein involved in developing of high myopia in humans. Two mouse models of Zfp644 protein were created to prove that Zfp644 is causative for developing the high myopia.
- **Reveal the physiological role and a molecular function of Zfp644 in mouse organism and explain the role of the transcription factor in female reproduction.** Zfp644 was described previously as a part of G9a/GLP complex. As the role of interactions of the G9a were previously described in female fertility we investigated *in vivo* the interaction pathway between Zfp644 and G9a in female fertility in cell lines and murine models.
- **The aim of a complementary project was to describe a role of Wiz in G9a/GLP complex.** G9a/GLP complex was described to work with, among the others, two zinc finger proteins simultaneously, ZNF644 and WIZ. The main interest of this thesis is the role of Zfp644, however, we would like to complement it with the findings on Wiz impact on murine development.

3. Materials and methods

3.1. Experimental approach

To reveal the function of Zfp644 in mouse organism, we decide to create several mouse models. We mainly focused on investigating two phenotypes in Zfp644 mutant mice: high myopia and female subfertility. Both required detailed analysis and use of sophisticated methods for evaluations of results. Taking advantage of accessibility to specialists and theirs equipment in Czech Center for Phenogenomics we were able to deeply analyze the phenotypes. We started the analyses from following the expression patter in adult animals and embryos in both qualitative (*in situ* hybridization) and quantitative (qPCR) way. The investigation of myopia in mice was focused on analysis of morphology and function of retina and analysis of ocular parameters by ultrasound. Analyses of fertility phenotype were more complex. We performed several breeding experiments on both males and females. Morphology and morphometry of ovaries as well as morphology of uterus were performed. Estrus cycle in mice as well as levels of hormones crucial for correct cycling in female mice were analyzed. Moreover, analysis of endometrium in pre- and post-implantation state were done. Finally, we proposed two strategies for rescue the subfertility phenotype in female mice.

In this study we also investigated the role of another transcription factor, working with G9a/GLP complex and ZNF644 simultaneously. Similar to Zfp644 studies, the investigation of the role of Wiz was based on knockout mouse model. The CRISPR technology was used to create the *Wiz* knockout mouse line. Next, after noticing that homozygous *Wiz* mice are embryonically lethal, further analysis on embryos between E14.5 and E18.5 were done. After the analysis of embryos with microCT, the fluorescent microscopy and proliferation assay were performed. The changes in methylation pattern in *Wiz* knockout embryos were followed, implicating necessity of WIZ protein presence for correct function of G9a/GLP complex.

3.2. Mouse models generation

All animal models and experiments used in this study were ethically reviewed and performed in accordance with European directive 2010/63/EU and were approved by the Czech Central Commission for Animal Welfare. All animal models were kept on a C57/Bl6N background and were created at Institute of Molecular Genetics, Prague.

For Zfp644^{S673G} and Zfp644^{Δ8} mouse models we used TALEN technology. TALENs targeting exon 3 of Zfp644 gene were designed using TAL Effector Nucleotide Targeter 2.0 (<https://talent.cac.cornell.edu/>)^{123,124} design tool and assembled using Golden Gate cloning method. Left TALENs were designed with 16 RVDs (NN NN NI NG HD NI NI NN HD NG HD NI HD NI NN NG) followed by 16 nt spacer region and right TALENs with 15 RVDs (NN NG NN NN HD HD NN HD NG NG NI NG NN NI NI NI NG). Both TALEN plasmids were used for production of TALEN encoding mRNA as described previously¹²⁵.

TALENs mRNA was mixed with a synthetic oligodeoxynucleotide encoding mutated Zfp644 sequence (5'AGG ATG CTA AAC GGA CAT TTG GAT CAT CCA GCC AGA GCG GTA ACT TCA GCA AGT TCC ACA AGA GAC CAC ATA GAA TAC AAA AAG CCCGG 3'). Targeting constructs were microinjected into male pronuclei of zygotes from C57BL/6N mice.

Both Zfp644^{-/-} and WIZ mouse models were created by CRISPR/Cas9 technology. Crispr targeting exon 3 of Zfp644 gene (transcript Zfp644-205 ENSMUST0000011269) and exon 4 of Wiz gene (transcript Wiz-001 ENSMUST00000087703) were used. Selected gRNAs for microinjections had following sequences: WIZ forward 5'-TGTAATACGACTCACTATAGGCCTGCTTTGAGACACGAAAGTTTTAGAGCTAGAAATAGC-3' and WIZ reverse 5'-TGTAATACGACTCACTATAGGCCCGCAGATGTGAACGTGCGGTTTTAGAGCTAGAAATAGC-3'. Zfp644 forward 5' TATGACTAGTGAAGAGACGG (TGG) 3' and Zfp644 reverse 5' ATTAAAGTGCGAGTATGAAC (AGG) 3', where () is the PAM sequence. gRNAs were introduced to the fertilized oocytes of C57Bl/6N strain and transferred into pseudo pregnant foster mice.

The introduced mutations led to: 1/desired point mutation in Zfp644^{S673G} mice and 2/Zfp644^{Δ8}; Zfp644^{-/-}; Wiz^{-/-} allele with the frame shift mutation (caused by deletion of desired sequenced) leading to a STOP codon.

All animals were further maintained on C57BL/6N background. For genotyping DNA extracted from tails of 3 weeks old C57BL/6N mice using the Quick Extract DNA Extraction Solution 1.0 Kit (Illumina, USA) was used as template for PCR with following primers: forward primer for Zfp644^{Δ8}: 5'-ATC AAG CTC ACA GTC AAG TAA TTT T-3'; forward primer for Zfp644^{S673G}: 5'-TCA GCA AGT TCC ACA AGA GACC-3'; reverse primer for both alleles: 5'-TTG TTG GTC AGT GCT GCT CTT AAC -3'; forward primer for Zfp644 5'-TAAGTGGAGGCCAGTCTGCT -3; reverse primer for Zfp644: 5'-GAGCACTTCTGCCTTCATCC -3'; reverse primer for Zfp644 (to distinguish wild type from heterozygote) 5'-TCTCCTCGTTTTGCCCTAGA-3'; forward primer for Wiz: 5'-CTTCTCTGAGCCTCAGTTTCC-3', reverse primer for Wiz: 5'-GATGGCTTTGTTGACAGCAGG-3'.

3.3. Microscopy and expression analysis

Histology

The mice were euthanized by cervical dislocation. Organs were sampled immediately, inserted into labelled histological cartridges, eyes and testes were fixed in Davidson's solution for 24 h, remaining organs and embryos were fixed in 4% PFA for 24h, next put into 70% ethanol solution to process using an automated tissue processor (Leica ASP 6025, Leica Microsystems, Germany), and embedded in paraffin blocks using a Leica EG 1150H paraffin embedding station (Leica Microsystems, Germany). Sections of 3-5 μm for organs were cut using a microtome (Leica M2255, Leica Microsystems, Germany) on standard glass slides (Waldemar Knittel, GmbH, Germany) or on a salinized slides (Thermo Scientific, USA) if used for immunohistochemical staining. Eyes samples were cut under the stereomicroscope view control and only medial cuts with optic nerve were selected for morphometry.

Representative organ's sections were stained with haematoxylin–eosin and mounted using Ventana Symphony H&E Slide Stainer (Ventana Medical Systems, Inc., USA).

Samples for Zfp644 studies were evaluated using a light-microscopic images obtained using a Carl Zeiss Axio Scope A1 (Zeiss, Germany) and the Axio Scan Z1 slide scanner (Zeiss, Germany).

For embryos 10-µm thick frontal sections through the palate area were mounted on Superfrost Plus slides. Embryonic sections were then deparaffinized in 100% Xylene and rehydrated using an alcohol range (100% - 70% - 30%) for immunofluorescence or *in situ* hybridization staining. For the immunofluorescence staining of embryonic samples, after deparaffinization, the antigen retrieval was performed with HIER Citrate buffer pH6 (Zytomed) for 15 min at 110°C. Next washing with Phosphate-buffered saline (PBS), permeabilization in 0,1% Triton-X at room temperature and blocking with 2, 5% ready to use Normal Goat Serum (Vector Laboratories) for 1 hour were performed. Primary antibodies were diluted in EnVision FLEX Antibody Diluent (Agilent) and applied overnight at 4°C. The dilutions of primary antibodies used: Ab Anti-Histone H3 (mono methyl K9) antibody - ChIP Grade (Abcam, ab9045) and Anti-Histone H3 (di methyl K9) antibody [mAbcam 1220] - ChIP Grade (Abcam, ab1220) were used at 1:250 dilution. Primary Ab WIZ Antibody (Novus Biologicals, NBP1-80586) was used at 1:200 dilution. Following PBS wash, secondary antibodies were applied to sections for 1 hour. (Donkey anti-Rabbit IgG (H+L) Highly Cross-Adsorbed Secondary Antibody, Alexa Fluor 488 (Thermofisher, A-21206) was used at dilution 1:1000 as well as Goat anti-Mouse IgG (H+L) Highly Cross-Adsorbed Secondary Antibody, Alexa Fluor Plus 594 (Thermofisher, A32742)). Sections were mounted with Dako Fluorescence Mounting Medium (Agilent) and kept in 4°C until microscopic images were taken in Axio Image Z2.

RNA *in situ* hybridization

Digoxigenin-labeled RNA probes (DIG RNA labeling Kit, Roche, Germany) for *In Situ* Hybridization (ISH) were generated by *in vitro* transcription from plasmid contained fragment of murine Zfp644, G9a, GLP or Wiz. Procedure were carried out according to standard protocol¹²⁶ on E9.5 after fixation in 4% PFA in whole-mount and 2 µm paraffin section for E12.5, E13.5, E14.5 and E15.5. Solutions used: Blocking solution (Roche, Germany), DIG-antibody (Roche, Germany), FastRed (SigmaAldrich, USA), DAPI mounting media (Molecular Probes, USA).

For fluorescence and bright-field imaging, Zeiss ImagerZ2 (Zeiss, Germany) was used, for whole-mount Zeiss Apotome (Zeiss, Germany) was used.

qPCR analysis

RNA was isolated and used as a template for reverse transcription into cDNA with M-MLV Reverse Transcriptase (Promega, USA). Quantative PCR (qPCR) reactions of Zfp644, G9a, GLP and WIZ on adult samples were performed using the TATAA SYBR® GrandMaster® Mix (TATAA Biocenter Sweden) in Cycloer LightCycler® 480 Instrument II (Roche, Germany). For embryonic studies and leptin expression analysis qRT-PCR was performed in The LightCycler® 480 (Roche, Germany). For leptin receptor expression analysis we used TaqMan probes (For leptin receptor expression analysis we used TaqMan probes (Lepr (all) Mm00440181_m1 Lepr (a) Mm01262070_m1 Lepr (b) Mm01265583_m1, B2m Mm00437762_m1, Sigma, USA) Sigma, USA). Expression levels of the genes of interest was estimated by the $\Delta\Delta C_t$ method¹²⁷ and normalized to levels of housekeeping reference genes (available upon request) and are presented as levels relative to wild type control (set as 1). Primers sequences are available upon request. All experiments were performed independently in triplicates on three different specimens ($n \geq 3$) per group; for embryonic studies, experiments were performed on four specimens per group.

Western blotting

Organs for Zfp644 protein expression analysis were collected from adult male mice and homogenized using beads in Tissue Lyzer II (Qiagen, Germany) in NETN400 Lysis buffer (0.5% NP-40, 50 mM Tris-HCl pH 8.0, 2 mM EDTA, 400 mM NaCl, 10 mM NaF, 50 mM β -glycerophosphate) containing protease inhibitors. Protein lysates were centrifuged at 4 °C at 3000 rpm for 5 min. The supernatant was carefully removed and pellets containing large plasma membrane pieces, DNA and nucleoli were diluted with NETN0 Lysis buffer (no containing salts) to 100 mM NaCl.

Embryonic tissue and adult tissues for remaining protein expression were harvested into RIPA buffer (150mM NaCl, 1% Nonidet P-40, 0.5% Sodium deoxycholate, 0.1% SDS, 1mM EDTA, 50mM Tris/HCl pH8) with phosphatase and protease inhibitors PhosSTOP (Roche,

Germany) and cOmplete Tablets, mini (Roche, Germany) and dissociated in Tissue Lyser II (Qiagene).

Protein concentration of samples were determined by Pierce BCA Protein Assay Kit (Thermo Scientific, USA). Samples were loaded on a 8% SDS-PAGE gel for Zfp644 protein analysis, 7% SDS-PAGE gel for embryonic samples and a gradient gel 4-12% (BioRad, USA) for remaining protein expression studies. Next, transferred onto nitrocellulose membrane (GE Healthcare Life Science, Germany). Membranes were blocked for at least 1 h in 5% milk in 0,05% Tween20 in TBS solution before incubating overnight at 4°C with the appropriate primary antibody. The following day, membranes were washed with TBS-T, incubated with appropriate secondary antibody (Sigma-Aldrich, USA) at room temperature for 1h and then washed again with TBS-T. Membranes were developed using Pierce™ ECL Western Blotting substrate (Thermo Scientific™, USA) for Zfp644 analysis and SuperSignal West Pico PLUS Chemiluminiscent Substrate (Thermo Scientific, #34580) for remaining analysis. Images were captured using a ChemiDoc™ detection system (Bio-Rad). Antibodies used: anti-GAPDH (G9545, Sigma-Aldrich, USA), anti-ZNF644 (raised against N-terminus AA50-602) was kindly provided by Xiaochun Yu, WIZ Antibody (Novus Biologicals, NBP1-80586), LEPR Antibody (ab5593, Abcam, USA), anti-G9a (ab185059, Abcam, USA), anti-H3K9me2 (D85B4, Cell Signalling, USA).

3.4. *In vivo* experiments for vision analyses

Optical coherence tomography (OCT)

The method was described in detail by Szczerkowska et al. 2019. Briefly, total of 15 Zfp644^{S673G} and 21 Zfp644^{Δ8} homozygous mice with 25 respective controls retinal fundi of 16 weeks old animals were examined. After anesthesia with 20% Zoletil–tiletamin 0.03 g/kg and zolazepam 0.03 mg/g (Virbac, France) and dilatation of pupils of eyes (Atropin-POS 0.5%; Ursapharm, Czech Republic). PMMA contact lens (Cantor&Nissel, UK) were placed on the eyes subsequently with the aqueous eye gel Vidisic 1 × 10 mg (Dr. Gerhard Mann Pharma, Germany). For the image acquisition of the retinal fundus, optical coherence tomography (OCT Spectralis™Plus, HRA Spectralis System Heidelberg Engineering GmbH, Heidelberg, Germany)

with a 30° lens was used. Mice were placed and fixed on a platform in front of the OCT camera and the eye horizontally directed toward the camera; the fundus was focused and cross sectional images were taken. The segmentation of retinal layers, retinal thickness, optic disc position and blood vessels pattern were analyzed from the high-resolution cross-sectional images using HRA/Spectralis Calculation Data Manager. The average of retinal thickness was calculated from values measured in the medial cross-section in the distance of 2 mm to the nasal and temporal side of fundus from the optic disc.

Electroretinography (ERG)

The method was described in detail by Szczerkowska et al. 2019. Briefly, ERG was performed under general anesthesia and protection of drying of eyes as described above. All measurements were done on the right eye 10 min after application of 0.5% solution of atropine (Ursapharm, Czech Republic). The ERG stimulation and recording setup (RETI-port for animal, Roland Consult, Germany) allowed single-flash stimuli to be applied to the whole retina by ganzfeld equipped with LED diodes and Xenon lamp, luminances were logarithmically distributed between 0.003 and 100 cd s/m². A golden ring (3 mm in diameter) was placed on the cornea as the active electrode, a golden wire inserted in the animal's mouth served as the reference electrode. Each stimulus was repeated 7–10 times and an averaged signal was saved. The signal was band-pass filtered between 1 and 300 Hz and digitized with 2 kHz sampling frequency. The scotopic and photopic responses were inspected offline using a custom-made script in Matlab (MathWorks), a-wave parameters were measured in the original recording whereas b-wave parameters were quantified after removal of the oscillatory potentials from the recordings by low-pass filtering with 80 Hz cut-off frequency.

Ultrasound imaging (USG)

The method was described in detail by Szczerkowska et al. 2019. The method was also used for evaluation of pregnancy in mice.

Briefly, ultrasound imaging was acquired by a Vevo 2100 Imaging System (FUJIFILM VisualSonics, Inc., Toronto, ON, Canada) equipped with a MS-550S transducer operating at a center frequency of 44 MHz. The MS550S has axial resolution of 40 µm at its focal depth. Care was taken to place the subjects in similar postures to ensure similar orientation. Sterile

hypoallergenic ultrasound gel without any air bubbles was applied between the eye (or abdomen –for pregnancy evaluation) and the transducer and subsequently eyes (embryos) were imaged. The eye structures were measured by manually delineating margins using Vevo ®LAB V1.7.0. Software. The software then calculated the corresponding length of each eye.

3.5. *In vivo* methods for fertility and metabolism studies

Fertility study

Mice of both sexes, of each genotype (wild type, heterozygotes, homozygotes), in reproductive age, were mated with wild type mouse for the period of four months. The breeding performance was evaluated for each mouse. Mice were kept in the same facility, in 12h/12h light/dark cycle and in regular conditions with access to food and water.

Mammary gland organoids

Female's mammary gland were collected after sacrificing the animals by cervical dislocation. The procedure was carried as previously described¹²⁸. Briefly, female mice of age 6 – 9 weeks were sacrificed by cervical dislocation, and mammary gland were collected, then minced, shake up to 40 min in 37°C in collagenase/trypsin solution in DMEM/F12 (GIBCO, USA), 0.1 g trypsin (GIBCO, USA), 0.1 g collagenase (Sigma C5138, USA), 5 ml fetal calf serum, 250 µl of 1 µg/ml insulin, and 50 µl of 50 µg/ml gentamicin (all University of California, San Francisco Cell Culture Facility, USA). Next the solution was centrifuged several times and resuspended in 4ml DMEM/F12 + 40 µl DNase (2U/µl) (SigmaAldrich, USA). After shaking by hand and centrifugation organoids were separated from single cells through centrifugation. The final pellet was resuspended in the desired amount (usually 50 µl) of Matrigel (Corning 356231, USA). The organoid assay was performed in 24-well plates (Corning, USA) at 37 °C in culture medium (DMEM/F12, 1% v/v insulin, transferrin, selenium (SigmaAldrich, USA) and 1% v/v penicillin/streptomycin (100× stock) or FGF2/branching medium (minimal medium + 2.5 nM FGF2 (Sigma F0291, USA).

Mammary gland whole mount staining

Mammary gland whole mount staining was performed according to a standard protocol. Briefly, mammary glands were isolated, spread on a glass slide and shortly air dried. Then, fixed

o/n in Carnoy's solution in 4°C. Next samples were rehydrate in 70% and then 50% ethanol and stain o/n with Carmine red. Following day, samples were dehydrate with 70%, 95% and 100% ethanol and moved to xylene for at least 2h. Samples were evaluated using a fluorescent images obtained using a Carl Zeiss Axio Scope A1 (Zeiss, Germany). Quantitative evaluation of size of the mammary gland was analyzed by AngioTool¹²⁹.

Measurement of endometrium thickness

Uterus thickness was analyzed based on H&E stained, scanned slides with use of Ventana Symphony H&E Slide Stainer (Ventana Medical Systems, Inc., USA). Samples were evaluated based on average of 3 measurements from each animal on both transversal and sagittal planes using a light-microscopic images obtained using a Axio Scan Z1 slide scanner (Zeiss, Germany).

Estrus cycle analysis

Estrus cycle was analyzed based on vaginal smears as described previously^{130,131}. Briefly, vaginal smears were prepared from cells collected through vaginal lavage (20 ul of PBS in room temperature). Collected samples were centrifuged directly on a glass slide (Rotofix 32A, Hettich, Germany) for 10 minutes in 8 000 rpm. Next, samples were air-dried and standard Giemsa staining was performed. Samples were evaluated with Axio Scan Z1 slide scanner (Zeiss, Germany).

Transplantation of ovaries

Donor mouse was sacrificed by cervical dislocation and ovaries were collected into PBS, next ovaries were divided into half with lancet. Recipient mouse was anesthetized with 20% Zoletil-tiletamin 0.03 g/kg and zolazepam 0.03 mg/g (Virbac, France). The ovary and uterus were surgically exposed, small incision in the bursa was made by scissors. With watchmaker's forceps ovarian fragment was placed through the incision into the bursal sac. Ovary and the uterus were gently placed back into the body cavity and suture with one stich. The skin was suture with wound clip. Mouse was kept on a heating pad in the temperature of 37°C until fully recovered from anesthesia and then placed into a clean cage. Breeding started four weeks later.

Blood collection from the orbital sinus and plasma isolation

Blood collection for the regular analysis as well as terminal blood collection was performed from the orbital sinus as describes previously ¹³². Collected blood was for 10 min kept at a room temperature and then kept on ice. To isolate plasma, blood sample was centrifuge at 3000 g for 10 minutes at 4°C (Centrifuge 5430R, Eppendorf, Germany). Plasma was aliquoted and stored in -80°C.

Measurements of hormone concentration

ELISA test were used to measure following hormones concentrations in plasma: Leptin (Mouse Leptin DuoSet ELISA; R&D Systems); 17- β -estradiol (Estradiol ELISA; LSBio LS-F5297) and progesterone (Progesterone Mouse/Rat ELISA; BioVendor RTC008R) according to manufacturer's protocol with use of Epoch™ Microplate Spectrophotometer (BioTek, USA). Levels of FSH, LH and prolactin in plasma were measured with Endocrine Multiplex Assay (Milliplex Mouse Pituitary Panel Merck Millipore MPTMAG-49K-03) according to manufacturer's protocol with use of Bio-Plex® 200 system (Bio Rad, USA). The results were analysed by Mixed ANOVA Interactions with Prism GraphPad 9.

Hormonal replacement therapy

Adult females in reproductive age were mated with control males overnight. If the mating occurs, females were injected with pellet with hormones (SP-131 Progesterone 15mg/pellet, SE-121 17 β -Estradiol 15mg/pellet) or placebo (SC-111 Placebo/Control 15mg/pellet) (all pellets were order from Innovative Research of America, USA). Application by injection, was performed under low concentration of isoflurane (1-3%). If case of a cut of a skin, stiches would be provided. After at least 7 days, pregnancy control was done by ultrasound imaging, under similar conditions of anesthesia. In case of pregnancy, females were observed until birth.

Indirect Calorimetry

The system used to perform the indirect calorimetry was a PhenoMaster (TSE Systems, Bad Homburg, Germany). The software used in the PhenoMaster PC was (TSE PhenoMaster v.7.1.2). Prior to the start the indirect calorimetry measurements, a complete calibration protocol for the gas analysers according to the manufacturer's recommendations using normal air compressed, CO₂ 1% and N₂ 100% was performed. Mice were weighted before introducing them

into the calorimetric system. Every cage *ad libitum* was provided to access to water and food, standard chow diet (Altromin 1314). Bedding volume was limited to approximately 150 ml during indirect calorimetry measurements to properly detect locomotor activity of the mice by infrared beam breaks frame surrounding the cage in the horizontal plane.

The mice were individually housed in a multiplex system with 8 cages plus reference cage. Sampling frequency to measure the CO₂ and O₂ gas measurements was every 15 min. The environmental conditions inside the climatic chamber were 23 degrees centigrade, 55% relative humidity and a light cycle of 12 hours of light and 12 hours of darkness synchronized with the animal facility where the mice were previously housed. The following 48 h period was used for measurements of the CO₂ production and O₂ consumption, where Energy Expenditure (EE) and Respiratory exchange ratio (RER) is calculated, and measurements for locomotor activity, and food and water intake. After 48h of experimental recording data, the experiment was stopped and the mice were weighted and placed to their original cages.

Non-invasive whole-body imaging

Non-invasive whole-body imaging was used to analyze the body composition (ratio of fat, muscle and skeleton) of experimental animals *in-vivo*. The aim was to provide multimodular information about the condition of the experimental animal. The expected benefit were to obtain the information on the physiological state of the animal in parallel with three-dimensional information on fat deposition in a non-invasive way enabling further experimental work according to relevant experimental projects.

The examination was performed under intraperitoneal induction. Zoletol (zolazepam, tiletamine) (20mg/ml) and xylazine (1 mg / ml) in dosage 50mg/kg zoletol, 3.2mg / kg xylazine were injected. The mouse was placed in a physiological position on the scanner bed (Bruker Skyscan1176) and launch tomographic scanning. Scanning takes 10-15 minutes, scanner chamber was heated to 37°C. Mouse was placed on a heated pad (37°C) until it wakes up from anesthesia and returned into the original cage afterwards.

The data were analyzed by SkyScan1176 with parameters: resolution 35 µm voxel; filter: Al 0.5 mm; exposure 200 ms; source voltage: 50 kV and source current:160 µA. NRecon 1.7.1.0. (Bruker, USA) was used for reconstructions and CT Analyser (Bruker, USA) 1.17.7.2+ was used for the analysis.

RNAseq

The RNA was isolated and the quality was analyzed. The RNA libraries were prepared with poly-A selection (SENSE Total RNA-Seq Library Prep Kit, Lexogen, USA). Then the sequencing was performed (NextSeq® 500/550 High Output Kit v2 and NextSeq PhiX Control Kit, Illumina, USA).

Statistical analyses

Statistical analyses from ultrasonography examination, hormonal plasma examinations and mammary gland analyses, breeding performance analyses were performed using GraphPad Prism software version 7.0 (GraphPad, USA); data were analyzed with one-way ANOVA. Data from OTC examination was performed in R software version 3.3 (R Core Team, Austria) using linear mixed model. Data from qPCR were analyzed using Genex 6.1 (MultiD, Sweden); qPCR statistic, analysis and graphs were performed in R software version 3.3 (R Core Team, > Austria). The statistical analysis of weight and results from bioimaging (aging experiment) were performed with use of linear mixed model using R (version 4.0.2), package lme4 (Douglas 2015) and multcomp (Torsten 2008). Data from indirect calorimetry was analyzed by CalR Version 1.2¹³³. RNAseq data was preprocessed by salmon (<https://combine-lab.github.io/salmon/>). Differential expression analysis were performed by DESeq (<https://www.bioconductor.org/packages//2.10/bioc/html/DESeq.html>). The RNAseq heatmaps were performed by pheatmap package (<https://cran.r-project.org/web/packages/pheatmap/pheatmap.pdf>) in R (version 4.0.2). If not stated otherwise, graphs were created with Excel 2016.

3.6. Embryonic studies

Embryo viability

The embryo viability was analyzed in two main steps: 1) successful weaning of knockout offspring from crosses of heterozygous pair, 2) viability observation, genotyping and systematic harvesting of embryos at E12.5, E14.5 and E18.5. For the study total of 4 litters at E12.5 (30 embryos), 6 litters at E14.5 (35 embryos) and 6 litters at E18.5 (36 embryos) were harvested.

MicroCT – samples preparation and scanning

The method was described in detail by Bukova et al. 2021. Briefly MicroCT analysis of embryos included scanning with incubation in contrast agent. Embryos were fixed for 7 days in 4% PFA, next stained for at least 10 days (E14.5) and 2 weeks (E18.5) with Lugol's Iodine solution. The stock solution (10g KI and 5g I₂ in 100ml H₂O) was diluted to a 25% working solution in H₂O to achieve neutral osmotic pressure and avoid tissue distortion. SkyScan 1272 high-resolution microCT (Bruker, Belgium) was set up for voxel size 2-3, 5µm, and 1 mm Al filter. A 360° scan with 0.200° rotation step and 3 frames averaging setup was used for scanning. In total 5 Wiz^{-/-} and 5 WT embryos were scanned at E18.5 and 4 Wiz^{-/-} and 2 WT embryos at E14.5. Crown Rump Length (CRL) was measured on 5 Wiz^{-/-} and 5 WT E18.5 embryos using ImageJ software. Frontal midline section from 3D reconstruction was used for the measurement.

4. Results

4.1. Mouse models introduction and verification

The main aim of this study was to reveal the molecular mechanism of Zinc finger 644. In order to answer the question, three different mouse models were created, each serving a different role in the study. First, two mouse models were created to serve the myopia study. One mimicking the human mutation (*Zfp644*^{S673G}) and the second one, that we suggest, is a truncated form of Zfp644 protein (*Zfp644*^{Δ8}). For further studies on the molecular mechanism, a full length knockout mouse was created, potentially working as a functional ablation of *Zfp644*, further called *Zfp644*^{-/-}. We suggest, that the difference between *Zfp644*^{-/-} and *Zfp644*^{Δ8} is crucial for understanding the molecular mechanism and function of Zfp644 in G9a/GLP complex. We hypothesized, that the truncated form of Zfp644 maintains the ability to bind with G9a, as described previously, situated at its N-terminus¹. It also preserve five out of eight zinc finger binding motifs, but not the atypical one. The functional ablation model does not retain any of these motifs. The stop codon placed much earlier than in the truncated variant (570 AA longer) allows the formation of only 102 amino acids which, we suggest, results in its inability to bind to the TAD domain of G9a protein. Created mutants are also graphically explained on a figure below (Fig.4.1).

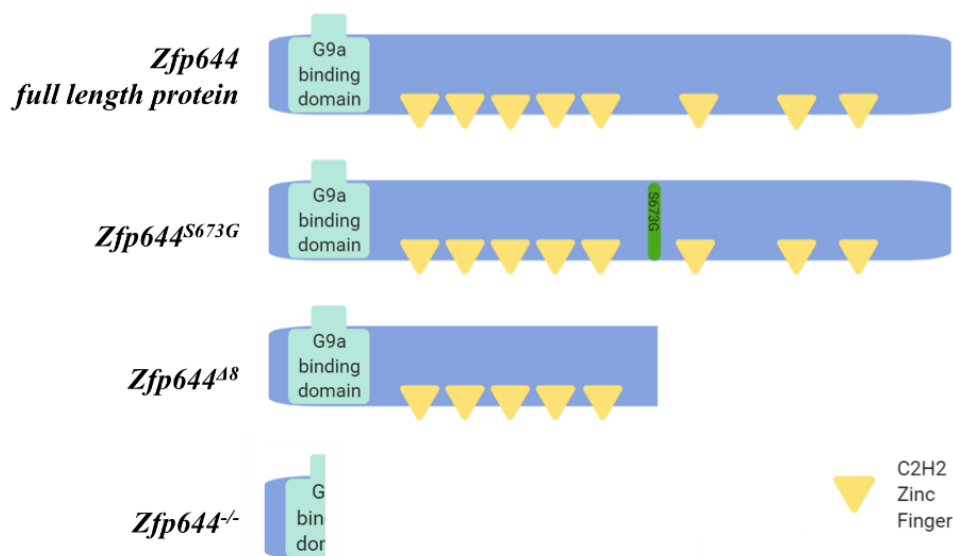


Figure 4.1. Graphical explanation of Zfp644 mutant models created in R. Sedlacek group. Cartoon was created with BioRender tool.

Additionally, the *Wiz* knockout mouse model was also created with use of CRISPR/Cas9 technology. Targeting the fourth exon resulted in 32 nucleotide deletion and frame shift mutation that led to a STOP codon.

On the figure below a detailed design of the knockout strategy for *Zfp644* with use of TALENs (Fig.4.2.A upper panel) for the creation of point mutation mutant (*Zfp644*^{S673G}) and a potentially truncated form of the protein (*Zfp644*^{Δ8}). CRISPR/Cas9 method was used to create the full protein knockout (*Zfp644*^{-/-}) by deleting of a large fragment (824 bp) of the third exon that results in a frame shift and introducing a STOP codon (Fig.4.2.A lower panel). A similar strategy was used for creation of the *Wiz*^{-/-} mouse model. Western blot analysis showed no expression of WIZ protein in homozygous embryonic sample (Fig.4.2.E) were provided. Verification of the design of *Zfp644* mouse models was done by sequencing and western blot results (Fig.4.2.B, D). The expected size of the *Zfp644* protein is 145 kDa, and is marked with the black arrow (Fig.4.2.D). Moreover, similarity between human and mouse amino acid sequence introduced in *Zfp644*^{S673G} mouse model was presented (Fig.4.2.C).

All of described mouse models were prepared by AFM of IMG, however the clear description of the design is crucial for understanding of the project. Presented sequencing and western blot of *Zfp644* were performed by the author of the doctoral thesis.

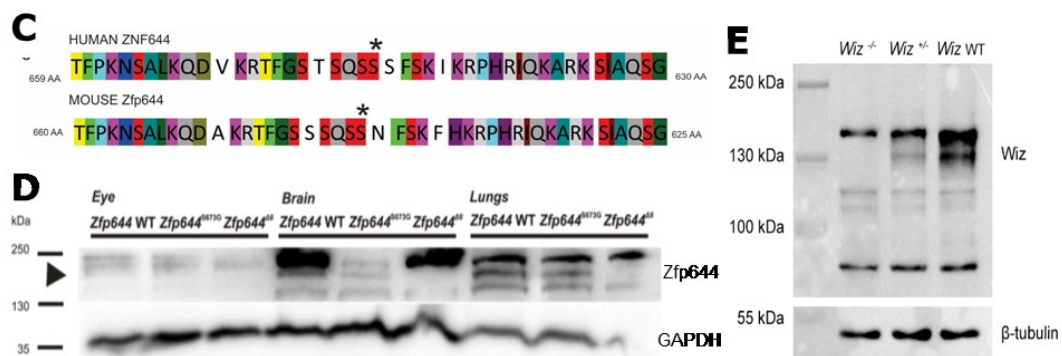
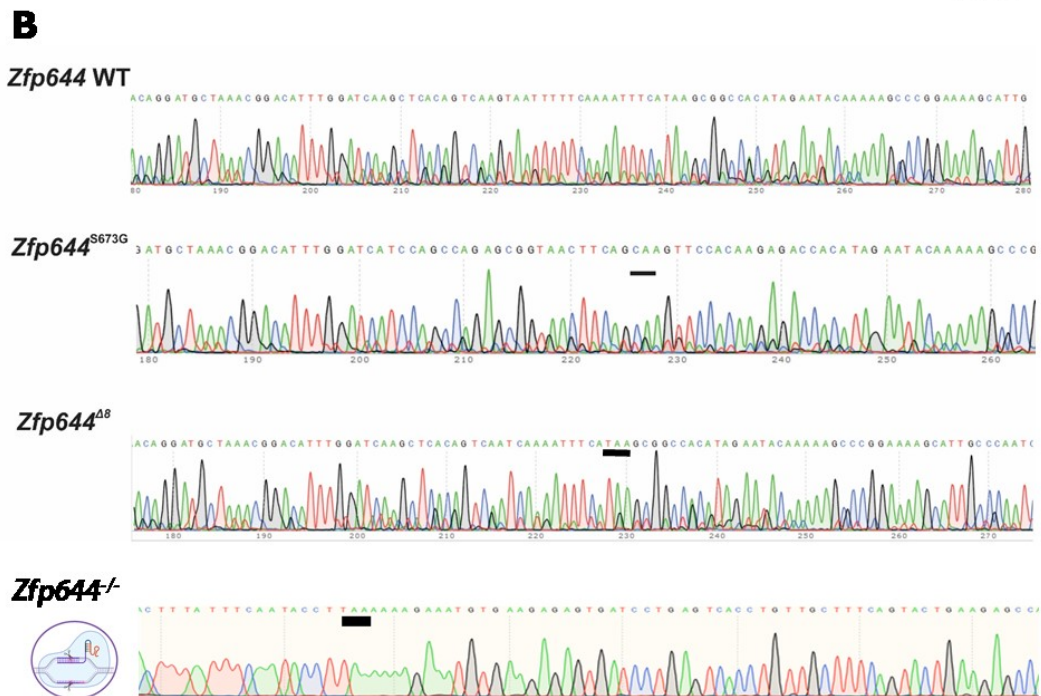
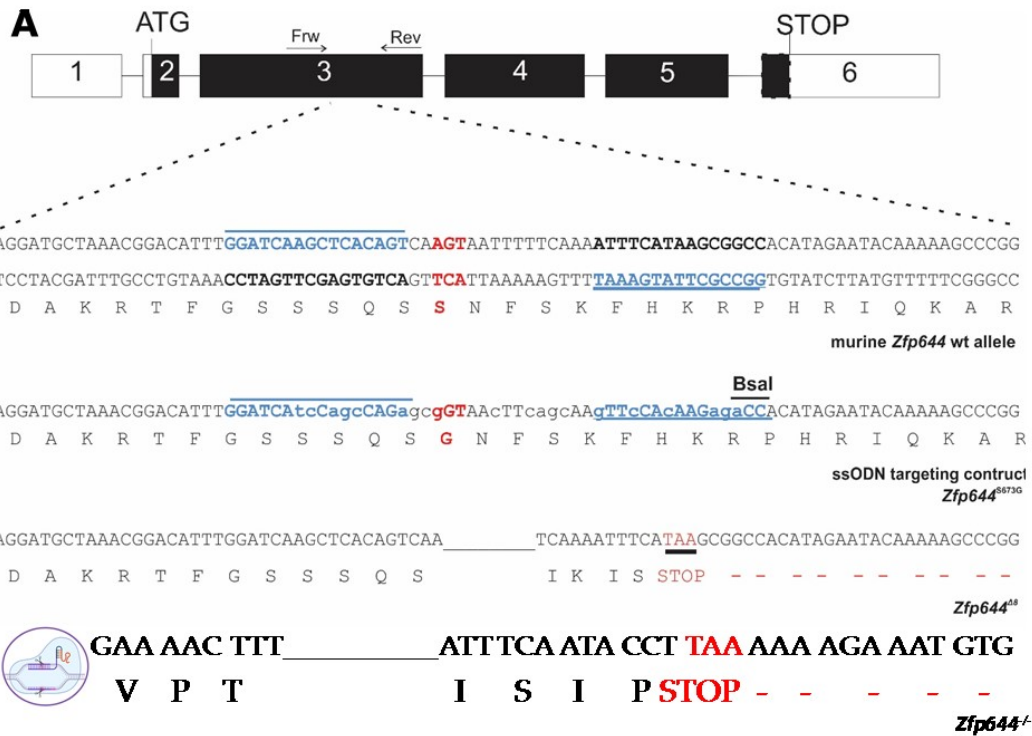


Figure 4.2. Generation of mutant mice used in the study. (A) Schematic representation of murine *Zfp644* gene with depiction of the targeted DNA sequence for TALEN and CRISPR targeting. Position of critical AGT nucleotides (red) in the exon 3 of murine *Zfp644*. TALEN binding sites are marked with blue underline, position of primers for PCR screening (For, Rev) are denoted. Sequence of *Zfp644*^{Δ8} with highlighted deletion of 8 nucleotides (black underline) and a STOP codon (red letters) is shown. Similar sequence is shown for CRISPR targeted *Zfp644*^{-/-}. (B) All of *Zfp644* mutations were confirmed by sequencing in both G1 and cDNA of adult mice eyes, brain and lungs of transgenic and control animals (C) Protein sequence alignment of human ZNF644 and mouse *Zfp644* showing position of the single point mutation at the amino acid at position 673 (asterisk); (D) In every examined tissue of *Zfp644*^{Δ8} animals no detectable protein expression of *Zfp644* can be found, while the samples of *Zfp644*^{S673G} and control animals show protein expression in every examined tissue. Black arrow indicates correct size of *Zfp644* protein (145 kDa). (E) Western blot analysis from *Wiz*^{-/-}, *Wiz*[±], and WT embryonic lysate showing protein *Wiz* sized 130 kDa in WT sample, lower amount in heterozygous sample and none present in KO sample Figure is partially adapted from Szczerkowska et al. 2019, Western blot analysis for *Wiz* animals (E) are adapted from Bukova et al. 2021; CRISPR/Cas9 graph created by biorender.com

4.2. Expression analyses

The quantification analyses of all the components of the studied complex were provided. *Zfp644*, *Wiz*, *G9a* and *GLP* genes are ubiquitously expressed in adult samples. Representative results, including testis, uterus, ovaries, prostate, eyes and liver are presented (Fig. 4.3. A-D). The analysis of wild type animals extended by two *Zfp644* mouse models - *Zfp644*^{S673G} and *Zfp644*^{Δ8} are presented on representative organs (Fig. 4.3. A-D). We found that quantitative expression of all examined genes was higher in testis and prostate than ovaries and uterus. Moreover, we found higher expression of *Zfp644* in male eyes, when compared to females, which might partially explain the results of vision examination in following chapters (4.4).

In a qualitative expression analyses *Zfp644* and *Wiz* were also localized in murine embryos and embryonic organs in different stages of development. *Zfp644* whole mount of wild type embryo at E9.5 is presented below (Fig.4.3.E) as well as in the developing eye at E12.5 and E14.5 (Fig.4.3.G, H). Expression of *Wiz* in palatal sections of mouse embryos at stages E13.5, E14.5 and E15.5 were analyzed (Fig.4.27.A). Moreover, qualitative studies of *Zfp644* expression in organs were performed on adult mice. Representative data in Figure 4.3 (F, I, J) shows the expression of *Zfp644* gene in adult eye, ovaries and testis.

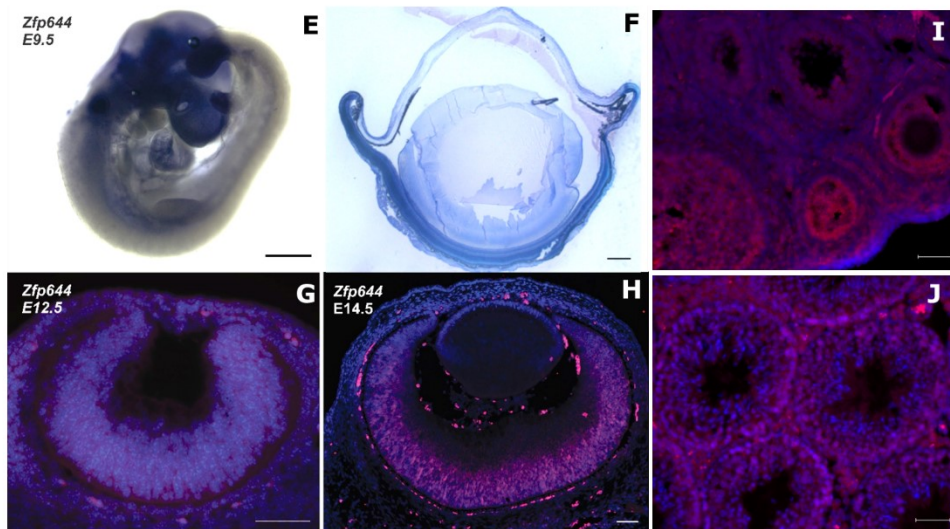
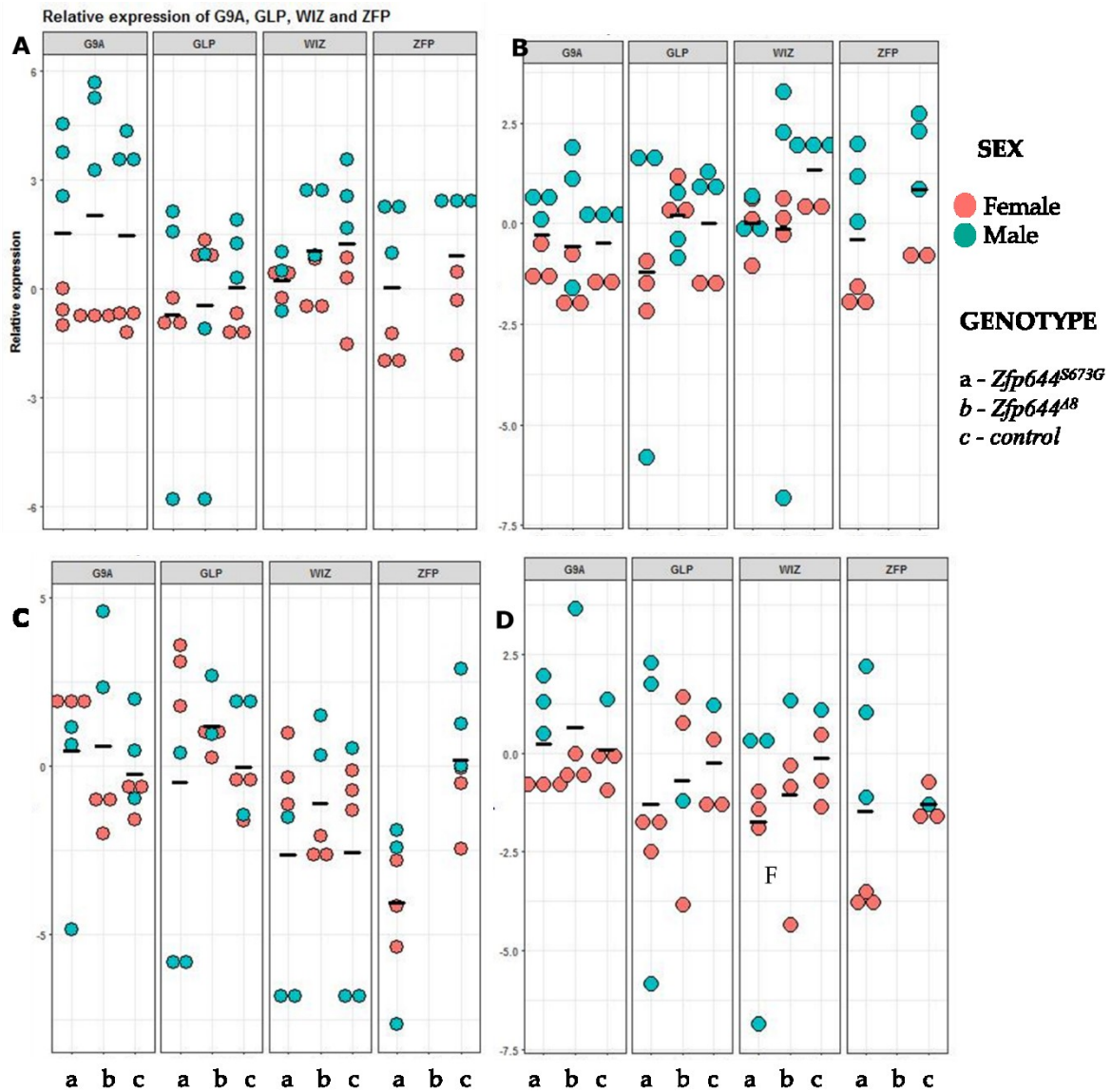


Figure 4.3. Expression analysis of Zfp644, Wiz, G9a and GLP in Zfp644 mouse transgenic models (*Zfp644*^{S673G} and *Zfp644*⁴⁸) and control animals. Results were normalized to control. No expression of Zfp644 was measured in *Zfp644*⁴⁸ samples. The results of expression of Zfp644, Wiz, G9a and GLP: **(A)** testis and ovaries **(B)** eyes **(C)** liver **(D)** uterus and prostate are presented in the top panel. Qualitative expression analysis performed by *in situ* hybridization are presented in the bottom panel: **(E)** Expression of *Zfp644* gene in embryonic eye at E9.5; scale bar, 500 µm. **(F)** Expression of *Zfp644* gene in adult eye of E 12.5; scale bar, 50 µm. **(G)** Expression of *Zfp644* gene in eye of E 14.5; scale bar, 50 µm. **(H)** Expression of Zfp644 in adult eye; scale bar, 500 µm. **(I)** Expression of *Zfp644* gene in ovary; scale bar 50 µm. **(J)** Expression of *Zfp644* gene in testis; scale bar 50 µm. Figure is partially adapted from Szczerkowska et al. 2019

4.3. Physiological role of Zfp644 and Wiz mutations on mice and extended analyses of metabolism

All four mouse models introduced in chapter 4.1 were phenotyped in the Czech Center for Phenogenomics (CCP). The CCP is led by my supervisor, Assoc. Prof. Radislav Sedlacek, Ph.D, and there is close cooperation between the Center and the Laboratory of Transgenic Models of Diseases. The phenotyping pipeline is performed on animals from nine weeks of age and finishes with histopathological, hematological immunological examinations at 16 weeks of age. The pipeline consists of profound analyses of the mouse organism. It includes analyses of main systems in mouse organism such as: behavior, vision, hearing, cardiovascular, metabolism or body composition. The results can be seen on the figure below (Fig.4.4). For the *Wiz* mouse model, the data comes from analysis of heterozygotes, as the model is embryonically lethal.

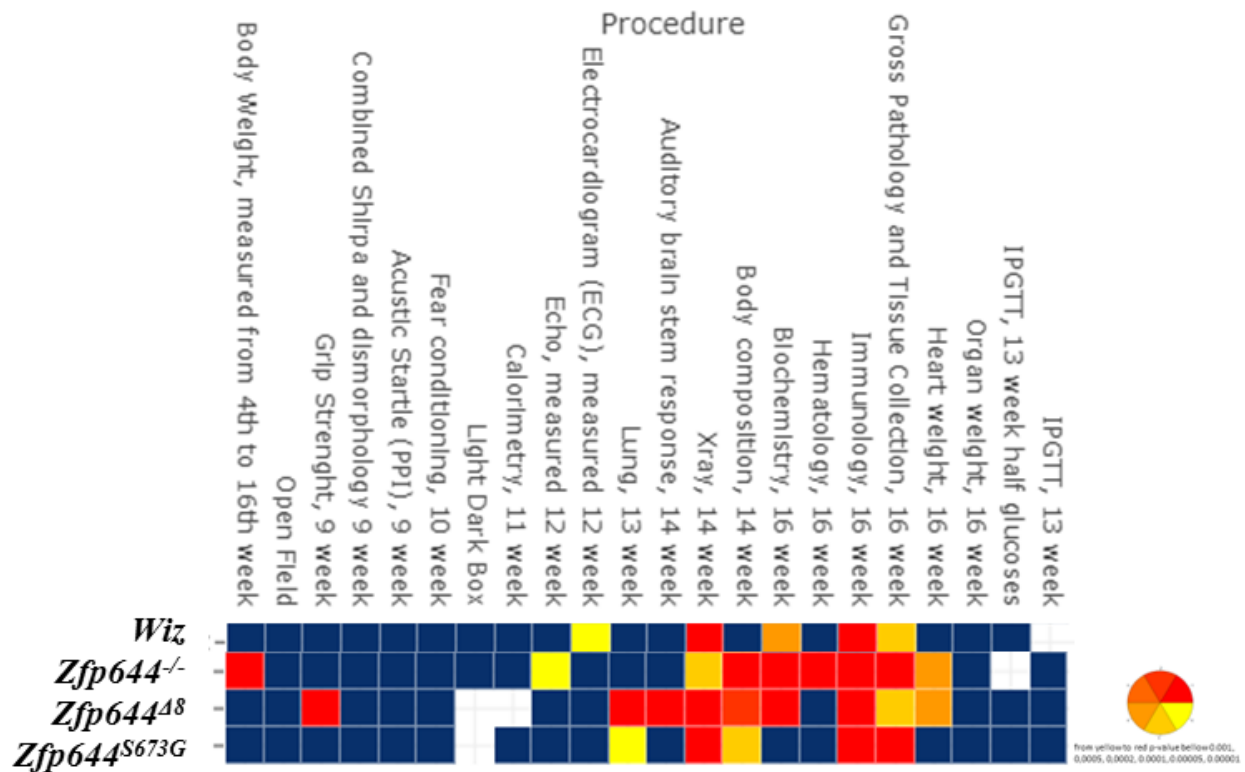


Figure 4.4. Graphical expression of phenotyping results of *Zfp644* mutant mice and *Wiz* mouse model generated in Czech Center of Phenogenomics shows significant differences in numerous biological systems. The presented data, beside the *Wiz* mutants, were collected from homozygous animals of both sexes. The levels of significance are indicated by colors from yellow to red, starting from p value = 0,001 (yellow) to 0,000001 (red).

On the graph the results of phenotyping can be appreciated. All of the described models exhibit significance across a range of biological systems. As already described, all *Zfp644* models show irregularities in vision, but also significant differences in biochemistry or body composition.

To follow up with these findings, we performed the analysis of weight from weaning to adulthood of mice from transgenic *Zfp644* lines. We found a significant difference in weight of both males and females of *Zfp644^{Δ8}* line during the whole measured period. The difference in weight of *Zfp644^{Δ8}* animals (Fig. 4.5.) led us to hypothesize, that the metabolism of the animals might be affected.

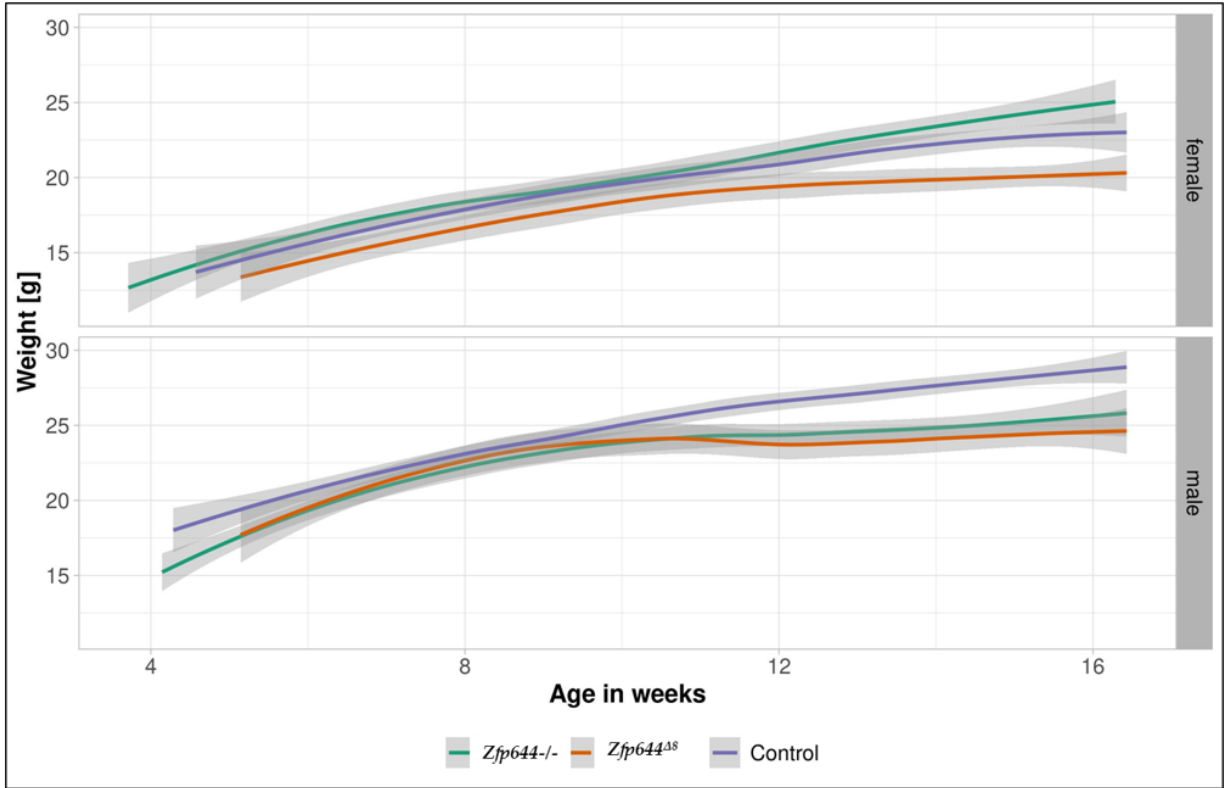


Figure 4.5. Analysis of weight of *Zfp644* transgenic mice shows severe weight decrease in *Zfp644*^{Δ8} animals. Comparison of weight between *Zfp644*^{Δ8}, *Zfp644*^{-/-} and control animals showed severe drop of weight in *Zfp644*^{Δ8} animals, significant for both males and females when compared to wild type controls. The weight is also significantly different for *Zfp644*^{-/-} males after 11 weeks of age, when compared to wild type controls. The grey area indicates the error bar.

To analyze the transcriptome, we performed the RNAseq analysis of uterus and compared the results of *Zfp644*^{Δ8} females with their wild type controls. The choice of the examined organ does not make a clear connection with the phenotype however we were simultaneously investigating the subfertility phenotype in *Zfp644*^{Δ8} females. The limited finding for the experiment, made us to choose the more promising phenotype, therefore we decided to run with the analysis of uterus. Among the others, we found the upregulation of LEPR (leptin receptor) in homozygous transgenic animals (Fig.4.6.).

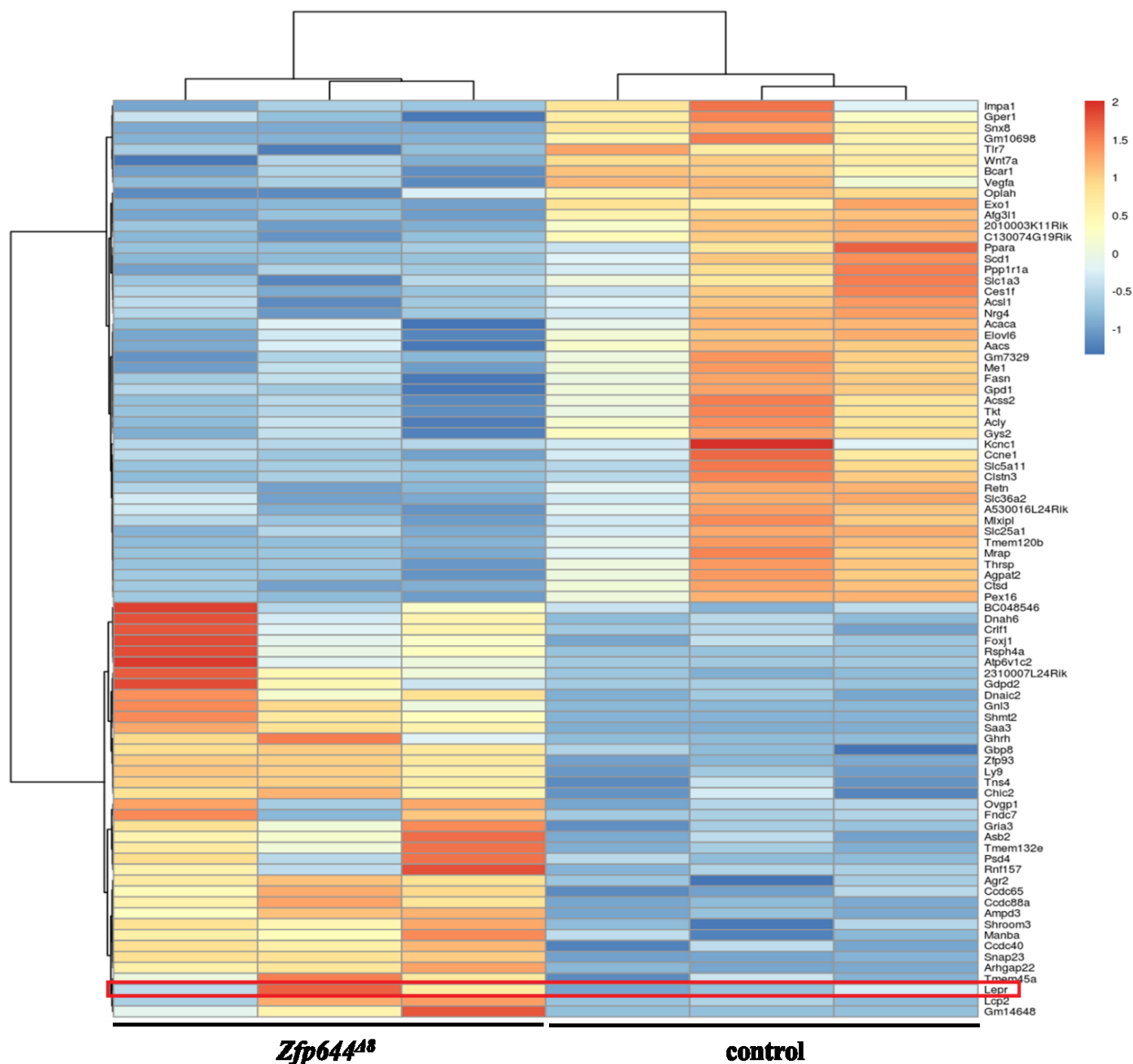


Figure 4.6. RNAseq analysis of uterus of *Zfp644*⁴⁸ females shows upregulation of the leptin receptor. The RNAseq results were compared between *Zfp644*⁴⁸ female uterus samples (left panel) and control samples (right panels) and only statistically significant genes are present on the heatmap. The legend of the heatmap is presented on the top right corner, showing upregulated genes are red and downregulated genes as blue. The leptin receptor expression is marked with red rectangle.

It was described previously, that leptin upregulation might result in lower body weight and a higher metabolism rate in mice ¹³⁴. Moreover, we analyzed the publically available ChIPseq data ¹ and found that both ZNF644 and G9a might interact and/or affect the expression level of LEPR. To evaluate the levels of leptin receptor in *Zfp644*^{Δ8} animals, we performed both gene (Fig.4.7.B) and protein expression (Fig.4.7.A) analysis as well as analysis of leptin level in plasma (Fig.4.7.C). However, no significant difference was found in any of measured parameters. This data suggests, that the difference observed on a transcriptome level, does not seem to affect the protein expression or leptin secretion in the examined animals. Taken together the analyses suggest that the difference in weight, found during the phenotyping examination, is not a result of upregulation of leptin receptor.

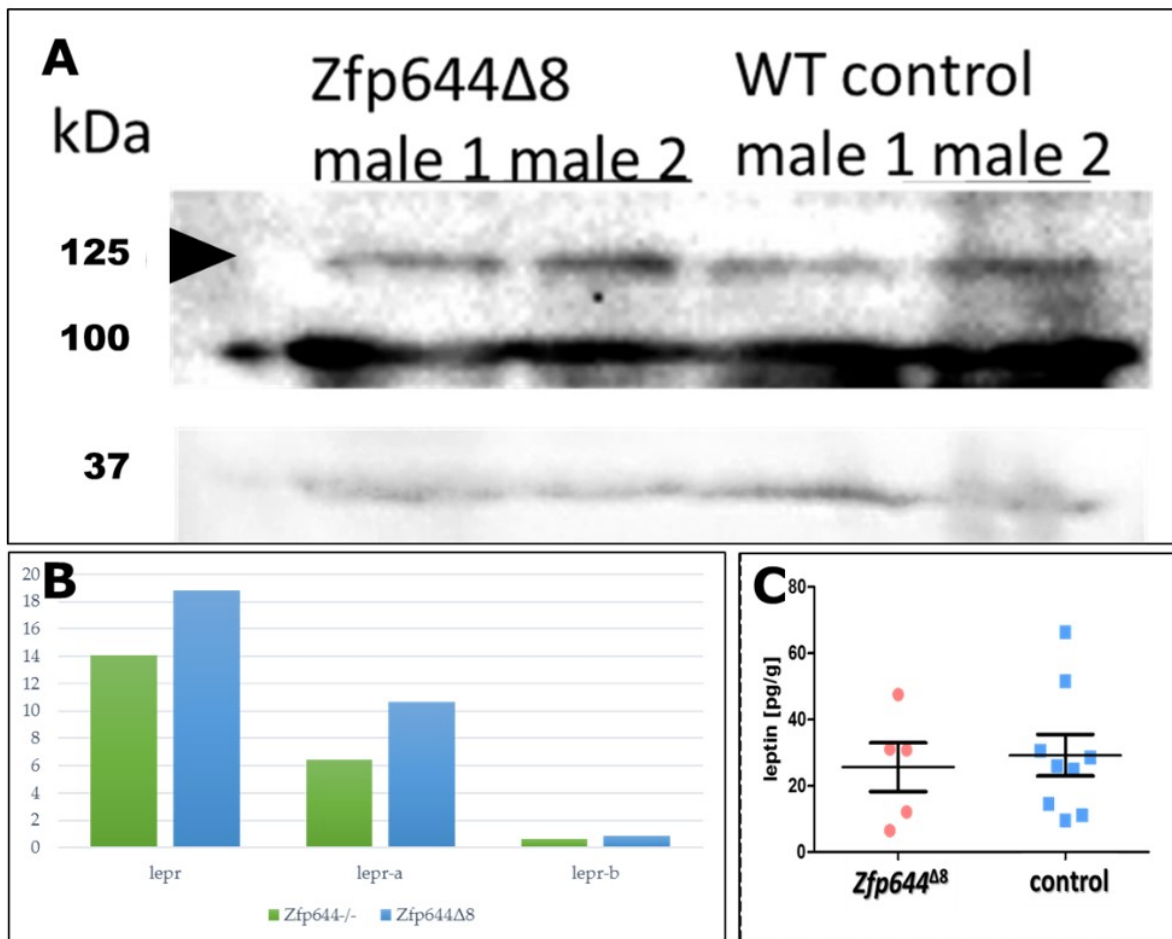


Figure 4.7. Analysis of expression of the leptin receptor and leptin level in plasma shows no differences among genotypes. (A) The expression of protein level of leptin receptor was measured in liver protein lysate of *Zfp644*^{Δ8}

homozygous males and compared to their wild type controls. The observed size of the protein is 125 kDa. A loading control used was GAPDH with observed size of 37 kDa. **(B)** Expression of *lepr* and both isoforms of leptin receptor – a and b were measured on a gene level. The tendency for upregulation was found in *lepr* and in isoform a were found, however the differences were not significant. **(C)** No significant difference in concentration of leptin in plasma was found in *Zfp644*^{Δ8} homozygous males when compared to their wild type control animals.

To further test the hypothesis, whether the metabolism of *Zfp644*^{Δ8} animals could be affected, an aging experiment was designed. A large group of animals, 16 females and 15 males were included in the experiment. Animals were divided into four groups (by age) and examined for multiple parameters. The examination included: indirect calorimetry, weekly weight measurements, body composition examination by μ CT and collection of plasma for further analysis of biochemical parameters. Both indirect calorimetry and the following plasma collection were repeated five times, every six weeks. The analysis started at 10 weeks of age of mice and finished at 41 weeks of age with terminal screen, including plasma collection and necropsy. Body composition was measured five times on a representative group of animals at age of 15, 25, 30, 35 and 40 weeks of age. Representative results of the performed examinations are presented on the figure below (Fig.4.8.).

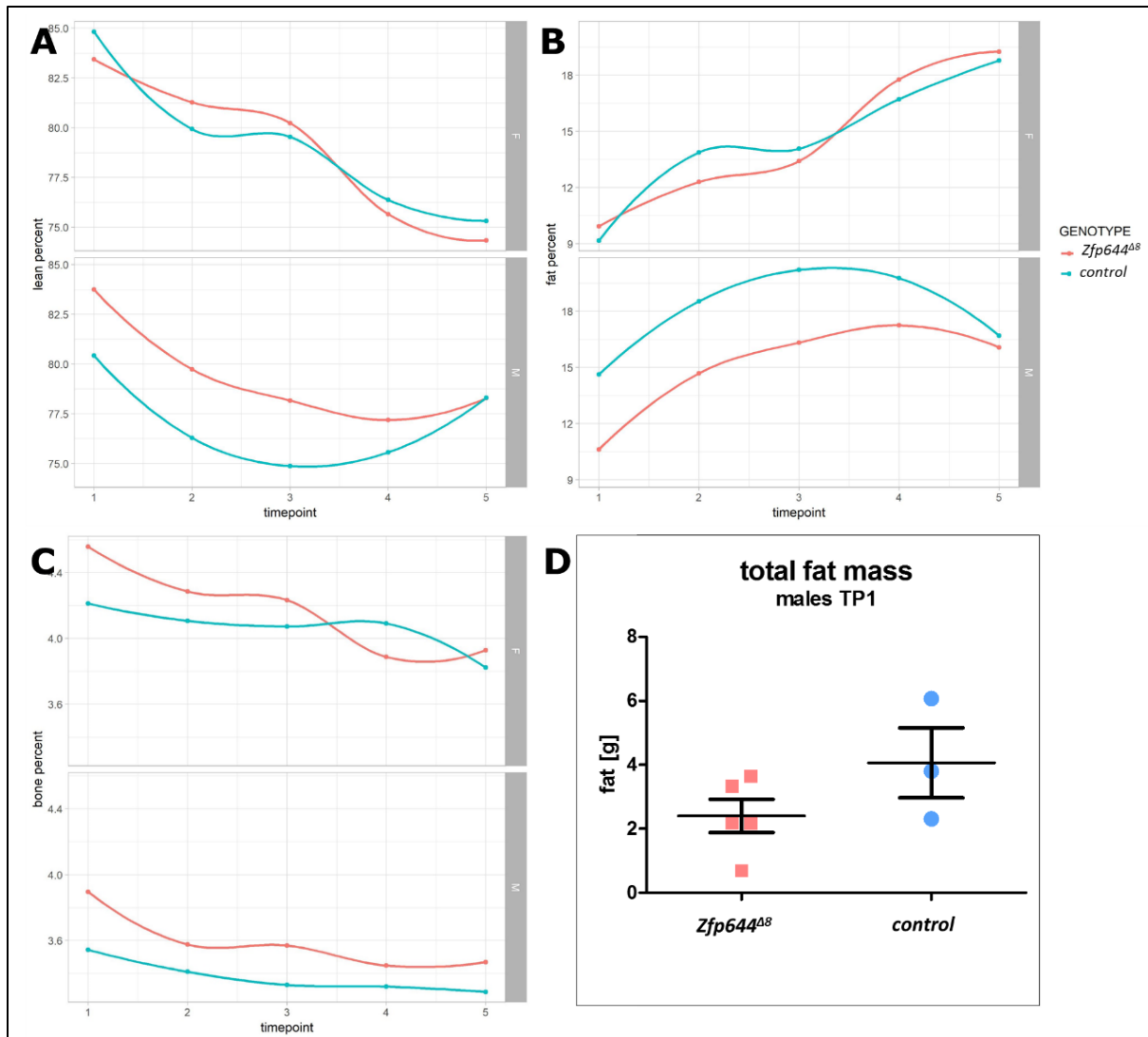


Figure 4.8. Analysis of body composition parameters: lean mass, fat content and bone mass shows tendency for lower fat content in *Zfp644*^{Δ8} males. The measured parameters: (A) lean mass, (B) fat content and (C) bone mass. The parameters are presented in percentage, as average of all measured values. No significant difference was found between *Zfp644*^{Δ8} and control animals. However a tendency to lower the fat content can be notice in males of *Zfp644*^{Δ8} line, when compared to control animals. The relative fat mass (D) shows the tendency for lower total fat mass in *Zfp644*^{Δ8} males in first time point.

Severe differences in weight of *Zfp644*^{Δ8} animals and a tendency for lower fat content in homozygous *Zfp644*^{Δ8} males and females (data not presented) when compared to their wild type controls, suggested a potentially higher metabolism rate in *Zfp644*^{Δ8} animals. Repeated

measurements of indirect calorimetry were performed in order to analyze it. Representative data of males collected during the first time point is presented on the figure below (Fig. 4.9.). It can be appreciated on a regression plot that no significant difference was found in energy expenditure in respect of body weight (Fig.4.9.B.), suggesting no metabolic differences between examined groups. Similar results were found in both males and females in each time point.

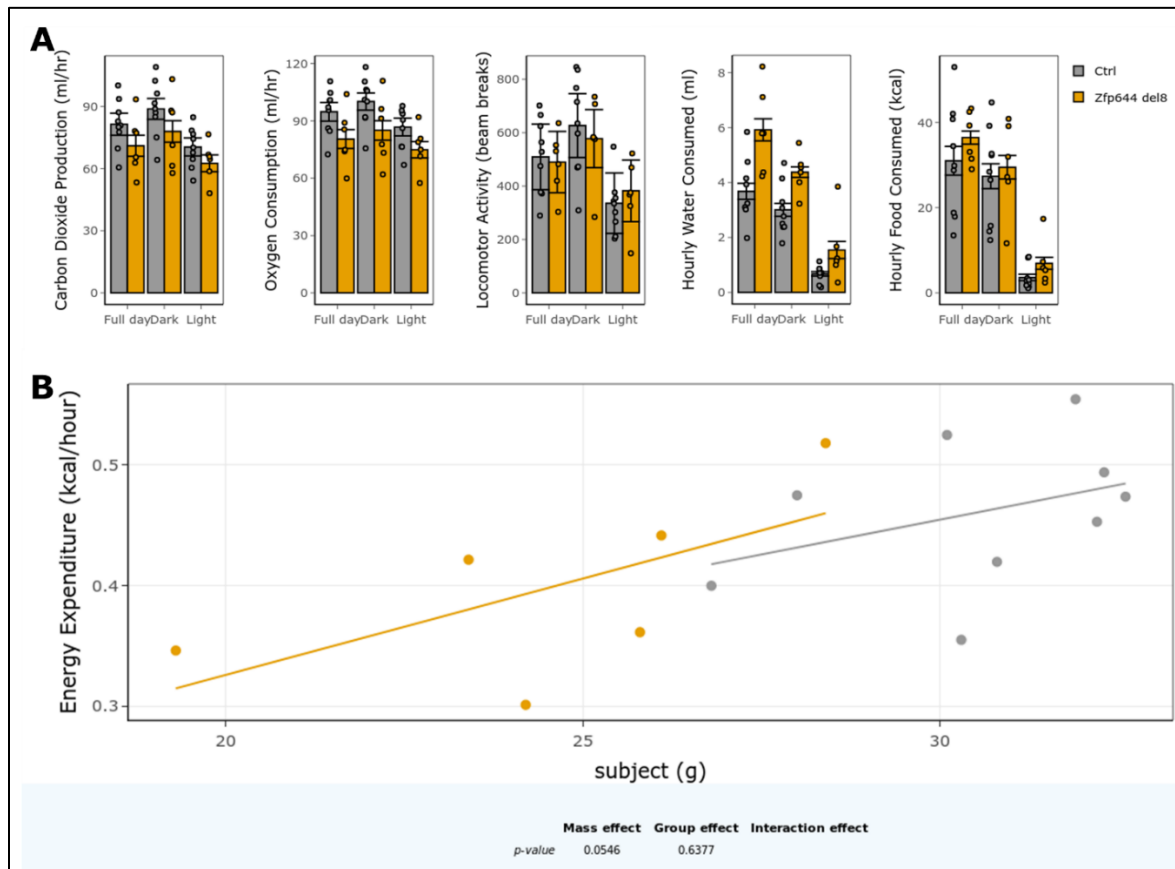


Figure 4.9. Analysis of metabolic rate in *Zfp644*^{Δ8} homozygous males shows no differences between genotypes. (A) The average results collected during 48h of the first time point are presented. No significant difference was found in any of measured parameters. The water and food consumption as well as locomotor activity differs between light and dark phases, what shows that the parameters were measured correctly and mice behavior was not interrupted. (B) The regression plot shows the energy expenditure in respect of the body weight and shows no significant difference.

Profound analysis of metabolism was performed on *Zfp644*^{Δ8} homozygous animals and compared with wild type controls. The preliminary data collected from the phenotyping pipeline examination as well as analysis of unbiased data (RNAseq of uterus (Fig.4.6) and ChipSeq analysis performed on HEK293T cells (Fig.4.10) suggested an interaction between *Zfp644*, *G9a* and *LEPR*. However detailed examinations of *Zfp644*^{Δ8} homozygous mice did not confirmed the tested hypothesis. No differences were found in protein level of leptin receptor nor in the levels of leptin in plasma. Moreover, we were able to analyze the metabolic rate of *Zfp644*^{Δ8} homozygotes in repeated measures on aging animals from both sexes. We did not find any effect of mutation introduced in the transgenic mouse line on metabolic rate, when compared to wild type controls. This data suggests that the significant weight difference present in the transgenic animals is not a result of metabolic disorder.

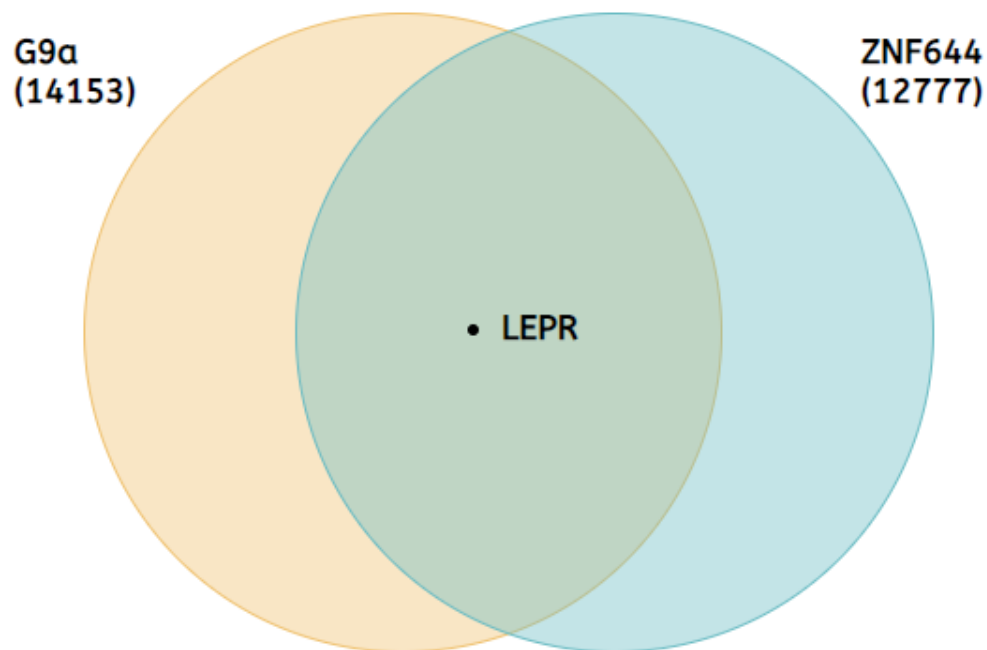


Figure 4.10. Schematic representation of ChipSeq data from HEK293T cells shows the leptin receptor binding in both G9a and ZNF644 analyses. Publically available data from ChipSeq analysis on HEK293T cells (Bian, 2015) were analyzed and are graphically explained on a Venn diagram. The enriched peaks of ZNF644 and G9a are significantly overlapping. Among the others, *LEPR* is common for both genes. The figure is inspired by Bian, 2015 and created with online tool: visual-paradigm.com.

4.4. Role of Zfp644 in high myopia

Myopia is the widest spread vision disease in the world. Among the others, also GWAS study were focused on finding the mutations present in high myopia patients. Interestingly, 12 mutations related to myopia were found among one gene – Zinc finger protein 644. In this study, we were focused on understanding the impact of Zfp644 mutations on mouse vision. Two mouse models were studied in order to reveal if mutations in Zfp644 gene are causative for high myopia in mice. The first mouse model used in this study, Zfp644^{S673G}, mimics one of the described mutations found in human, second model is a potentially truncated form of the protein, called Zfp644^{Δ8}. The design and details of these mouse models as well as expression studies were described in detail in previous chapters.

Mutations in Zfp644 lead to myopia caused by enlargement of the optical axis

Myopia is a disease caused by refractive error that occurs due to elongation of an axial length. Therefore, we asked the question if ocular parameters in Zfp644 transgenic mouse models were impacted by the introduced Zfp644 mutations. Different ocular parameters were analyzed *in vivo* by an ultrasound imagining technique. High-frequency ultrasound imaging¹³⁵⁻¹³⁸ was used to image posterior structures of the eye, in particular, the retina and optical nerve (Fig. 4.11.C and Table 1 and 2). Ultrasound images of eyes allow the measurement the ocular parameters i.e. axial length (AL), vitreous chamber depth (VCD), lens diameter (LD) and lens thickness (LT). The performed examinations included homozygous and heterozygous Zfp644^{S673G} mice (Fig. 4.11.A) Zfp644^{Δ8} mice (Fig.4.11.B), and the corresponding wild-type control mice at the age of 12–14 weeks.

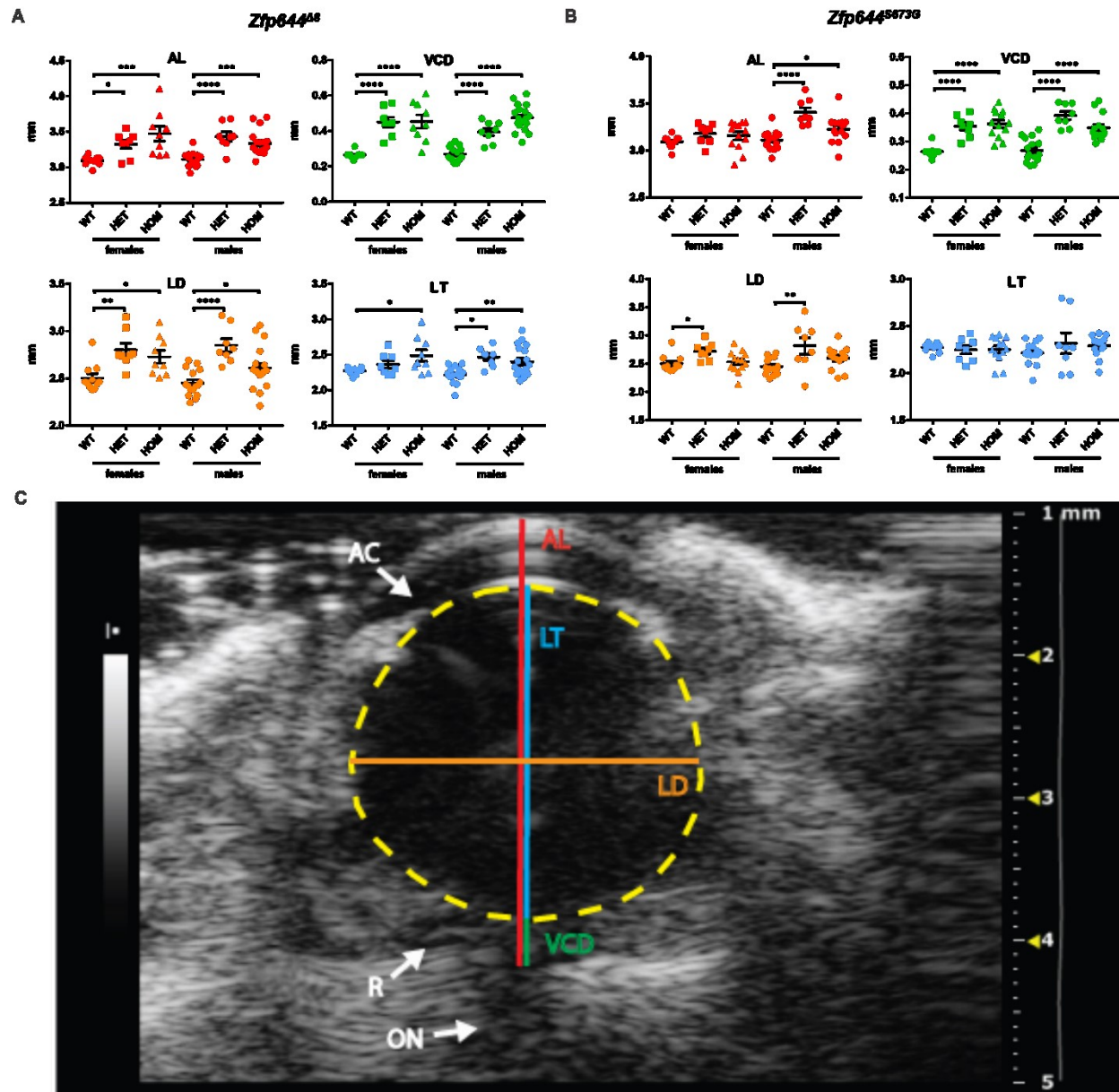


Figure 4.11. Analysis of ocular parameters measurement with an ultrasound. Four different ocular length parameters were measured: AL (axial length; in red), VCD (vitreous chamber depth; in green), LD (lens diameter; in orange) and LT (lens thickness; in blue). Analysis of ocular length parameters between groups in **(A)** *Zfp644^{Δ8}* and **(B)** *Zfp644^{S673G}*; Most prominent differences were detected in axial length and vitreous chamber diameter **(C)** Typical ultrasound image of the mouse eye; Four ocular length parameters are shown on a typical ultrasound image of an eye: AL (axial length; in red), VCD (vitreous chamber depth; in green), LD (lens diameter; in orange) and LT (lens thickness; in blue). The lens border is depicted by yellow dashed line. White arrows indicate anterior chamber (AC), optical nerve (ON) and retina (R). Figure is adapted from Szczerkowska et al. 2019

In *Zfp644*^{S673G} animals (Fig. 4.11.A and Table 1), a significant difference in measured optical parameters was found only in males. Even more interestingly, heterozygous males exhibit a higher penetrance of the phenotype than homozygote males suggesting a weak dominant negative effect of S673G mutation with gender specific bias. Data from females, did not show significant difference in total axial length. The analysis of vitreous chamber depth showed a significant difference in both, the heterozygous and homozygous animals, without gender influence.

Similarly, *Zfp644*^{Δ8} heterozygous animals showed the most significant changes in lens diameter. Moreover, alteration of the axial length is caused by morphological changes in vitreous chamber depth as well as in lens thickness and diameter (Fig. 4.11.B Table 2). To conclude, the presented analysis showed that each of the examine components of the optical axis is affected by the mutation. Differences in individual ocular parameters result in enlargement of the optical axis, meaning it results in the high myopia phenotype. The only parameter without observed significant difference, but only a tendency, was the lens thickness in heterozygous females from *Zfp644*^{Δ8} mice.

To summarize, the effect of both mutations is clearly visible in presented analysis of ocular parameters. The stronger effect on phenotype was observed in *Zfp644*^{Δ8} animals. Interestingly, in the case of S673G mutation, the eye morphology was affected more in heterozygous constitution in multiple parameters. Altogether, these results suggest dominant negative behavior of the mutated form of *Zfp644* and closely mimics the situation reported in human patients⁶.

Table 1: Summary of the results of ophthalmologic ultrasound measurements on WT, HET and HOM Zfp644^{Δ8} eyes. For each sex, medians, first and third quartile and p-values were calculated by one-way ANOVA analysis comparing WT, HET and KO eyes.								
Parameter	female			male			female	male
	WT	HET	KO	WT	HET	KO		
	n=11	n=8	n=9	n=16	n=8	n=19		
	median [25%, 75%]						p-value	p-value
LT (mm)	2.285 [2.25, 2.295]	2.316 [2.23, 2.473]	2.387 [2.283, 2.697]	2.215 [2.194, 2.285]	2.502 [2.351, 2.561]	2.329 [2.234, 2.59]	WT vs. HET ns WT vs. KO p=0.0149	WT vs. HET p=0.002 WT vs. KO p=0.0037
LD (mm)	2.465 [2.407, 2.583]	2.745 [2.708, 2.968]	2.642 [2.545, 2.908]	2.426 [2.334, 2.583]	2.797 [2.705, 3.054]	2.58 [2.535, 2.655]	WT vs. HET p=0.003 WT vs. KO p=0.0192	WT vs. HET p=0.0001 WT vs. KO p=0.0309
AL (mm)	3.096 [3.047, 3.125]	3.355 [3.149, 3.428]	3.454 [3.181, 3.651]	3.129 [3.036, 3.166]	3.43 [3.344, 3.607]	3.276 [3.229, 3.364]	WT vs. HET p=0.0392 WT vs. KO p=0.0007	WT vs. HET p=0.0001 WT vs. KO p=0.0002
VCD (mm)	0.264 [0.254, 0.264]	0.443 [0.386, 0.527]	0.433 [0.362, 0.557]	0.254 [0.237, 0.308]	0.401 [0.332, 0.444]	0.472 [0.425, 0.528]	WT vs. HET p=0.0001 WT vs. KO p=0.0001	WT vs. HET p=0.0001 WT vs. KO p=0.0001
LT, lens thickness; LD, lens diameter; AL, axial length; VCD, vitreous chamber depth; ns, non-significant								

Table 1. Summary of the results of ophthalmologic ultrasound measurements on Zfp644^{S673G} eyes. For each sex, medians, first and third quartile and p-values were calculated by one-way ANOVA analysis comparing WT, HET and HOM eyes. Figure is adapted from Szczerkowska et al. 2019

Table 2: Summary of the results of ophthalmologic ultrasound measurements on WT, HET and HOM Zfp644^{S673G} eyes. For each sex, medians, first and third quartile and p-values were calculated by one-way ANOVA analysis comparing WT, HET and KI eyes.								
	female			male				
	WT	HET	KI	WT	HET	KI		
	n=11	n=8	n=13	n=16	n=8	n=14		
	median [25%, 75%]							
LT (mm)	2.285 [2.25, 2.295]	2.27 [2.136, 2.351]	2.259 [2.189, 2.381]	2.215 [2.194, 2.285]	2.272 [1.978, 2.652]	2.329 [2.251, 2.368]	WT vs. HET ns WT vs. KI ns	WT vs. HET ns WT vs. KI ns
LD (mm)	2.465 [2.407, 2.583]	2.724 [2.577, 2.818]	2.567 [2.423, 2.667]	2.426 [2.334, 2.583]	2.837 [2.578, 3.09]	2.61 [2.515, 2.711]	WT vs. HET p=0.0142 WT vs. KI ns	WT vs. HET p=0.002 WT vs. KI ns
AL (mm)	3.096 [3.047, 3.125]	3.213 [3.102, 3.269]	3.208 [3.056, 3.286]	3.129 [3.036, 3.166]	3.35 [3.289, 3.526]	3.237 [3.141, 3.3]	WT vs. HET ns WT vs. KI ns	WT vs. HET p=0.0001 WT vs. KI p=0.0321
VCD (mm)	0.264 [0.254, 0.264]	0.358 [0.322, 0.387]	0.366 [0.323, 0.405]	0.2541 [0.237, 0.308]	0.387 [0.351, 0.436]	0.332 [0.321, 0.368]	WT vs. HET p=0.0001 WT vs. KI p=0.0001	WT vs. HET p=0.0001 WT vs. KI p=0.0001
LT, lens thickness; LD, lens diameter; AL, axial length; VCD, vitreous chamber depth; ns, non-significant								

Table 2. Summary of the results of ophthalmologic ultrasound measurements on Zfp644^{Δ8} eyes. For each sex, medians, first and third quartile and p-values were calculated by one way ANOVA analysis comparing WT, HET and HOM eyes. Figure is adapted from Szczerkowska et al. 2019

Morphology and function of the retina remains unchanged in the mutant models

It was previously described, that ZNF644 depletion in zebrafish has a severe impact on morphology and function of retina. Therefore, the murine eyes of *Zfp644* transgenic animals were analyzed for morphology and function of retina. We examined both eyes in homozygous mutants of *Zfp644*^{S673G} (n=15) and *Zfp644*^{Δ8} (n=21) with OCT at 16 weeks of age and compared them with 25 aged-matched control animals. The *in vivo* imaging of retina by OCT showed that the retinal thickness of transgenic animals is thinner when compared to control animals (Figure 4.12 D). Retinal layer segmentation, optic disc position and blood vessel patterning was assessed. However, a tendency, and not significant differences were found in these parameters (Figure 4.12. A–C').

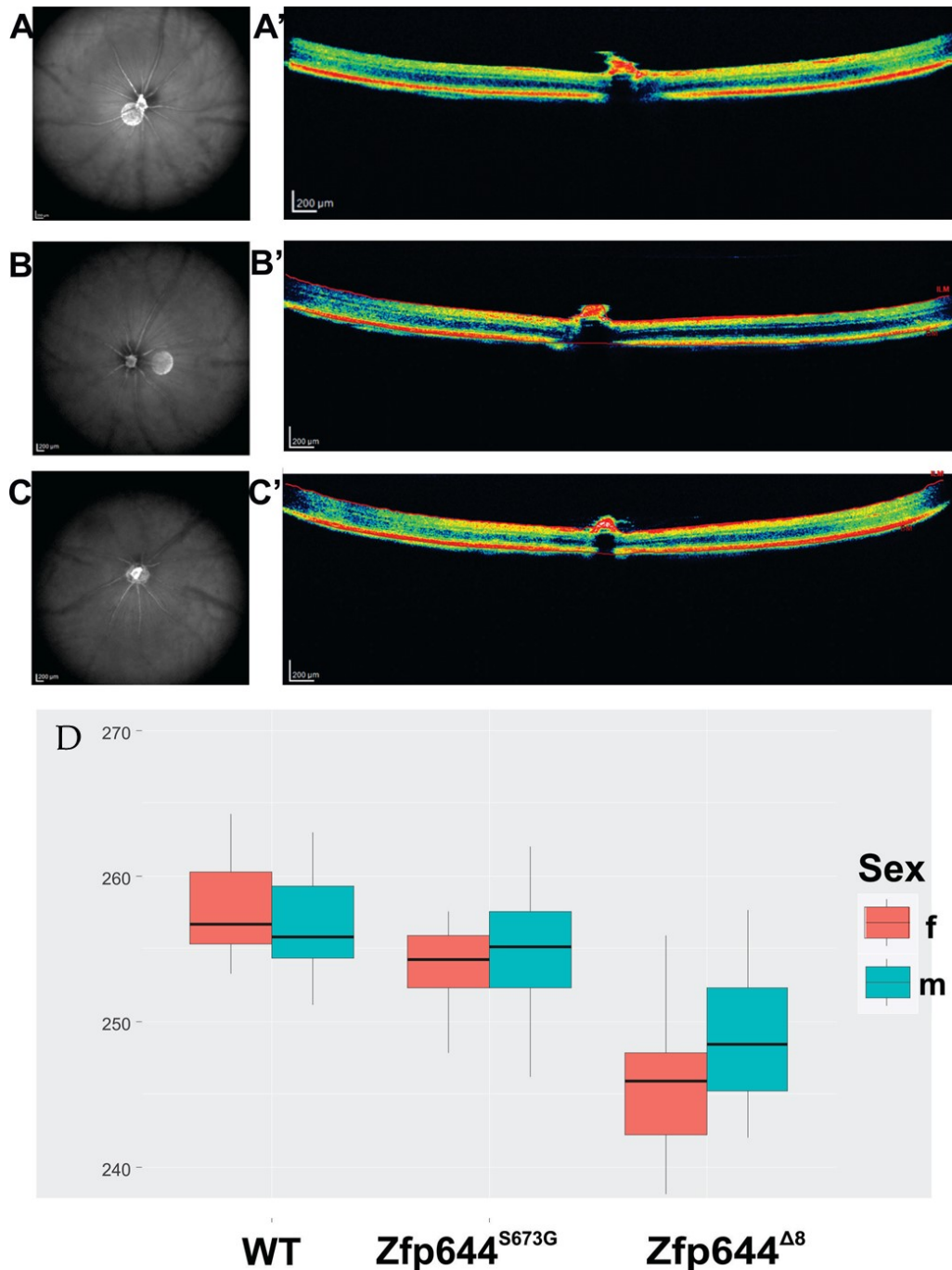


Figure 4.12. Typical view of the fundus with the optic disc and blood vessels showed no differences among genotypes. Typical view of the fundus with the optic disc and blood vessels in the (A) WT, (B) Zfp644^{S673G} and (C) Zfp644^{Δ8}. The white spot is a reflected light. A typical view of the retinal cross-sections thru the optic disc, respectively (A'-C'). ILM – internal limiting membrane, BM – Bruch's membrane. Scale bar; 200 μm. (D) Retinal thickness profile; Retinal thickness was measured as an average of five measurements on both temporal and nasal parts of fundus, starting from 0,5 μm from the middle of the optic disc, thru the nasal or temporal retina in 1,5 μm distance. Statistical analyses of retinal thickness distribution are showed in a box plot. Figure is adapted from Szczerkowska et al. 2019

Similar results were obtained with histopathological examination of retinal structure where no difference was found. Representative image of an eye from each mouse mutant line is presented in the figure below (Fig. 4.13).

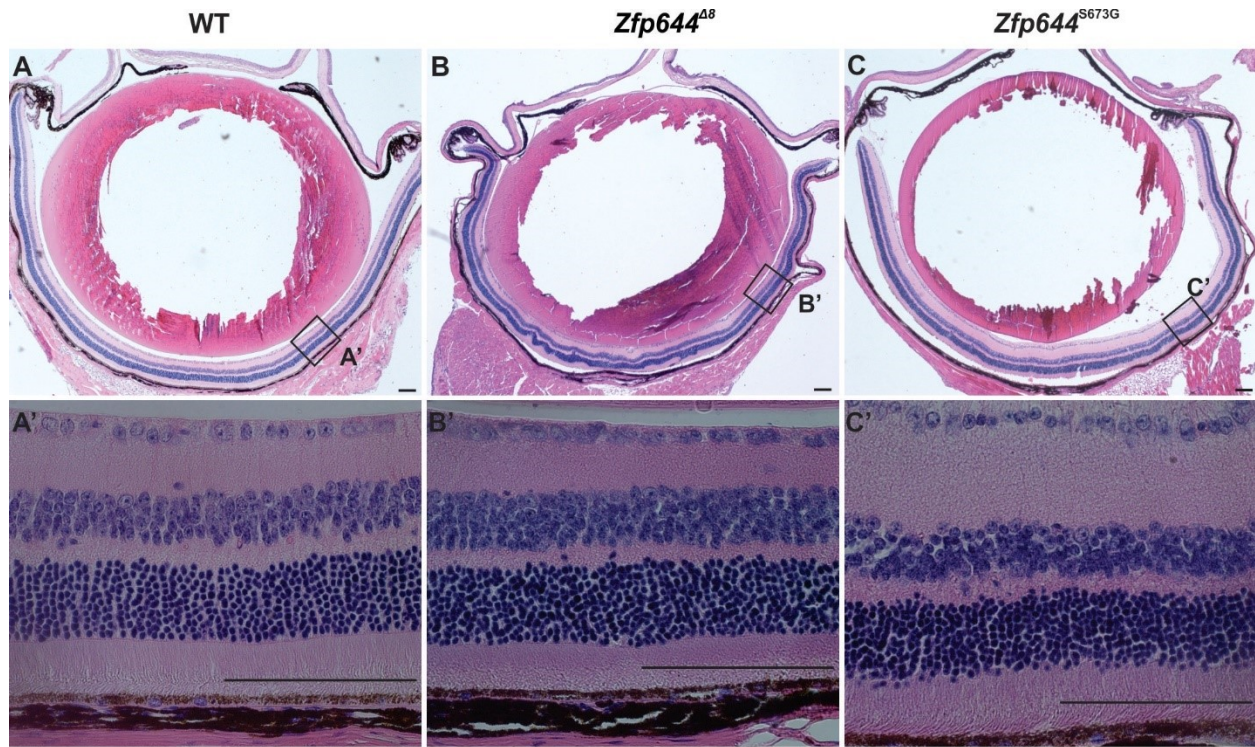


Figure 4.13. Morphology of retina showed no differences among genotypes. Morphology of retina remain unchanged in transgenic animals. Histological examination of retina, was done on 5 weeks old and 16 weeks old animals and compared between WT and transgenic animals. Representative image of eye sections of 5 weeks old animals are presented for (A) control animals, (B) $Zfp644^{\Delta 8}$ and (C) $Zfp644^{S673G}$ animals; scale bar, 100 μm . (A'-C') Zoom in on retina; scale bar, 100 μm ; Positions of zooming are denoted with a black square. Figure is adapted from Szczerkowska et al. 2019

In order to provide functional validation of morphological findings, electrophysiological measurements were performed. The electroretinography method allowed us to assess the response of photoreceptors and other neurons to light stimulation. Amplitudes and implicit times of scotopic and photopic wave a (response of photoreceptors) and wave b (response of bipolar cells) respectively, were measured. Similar to *in vivo* examinations performed by OCT and histopathological examination of eye structures, no abnormalities were found in the mutants (Fig.4.14.).

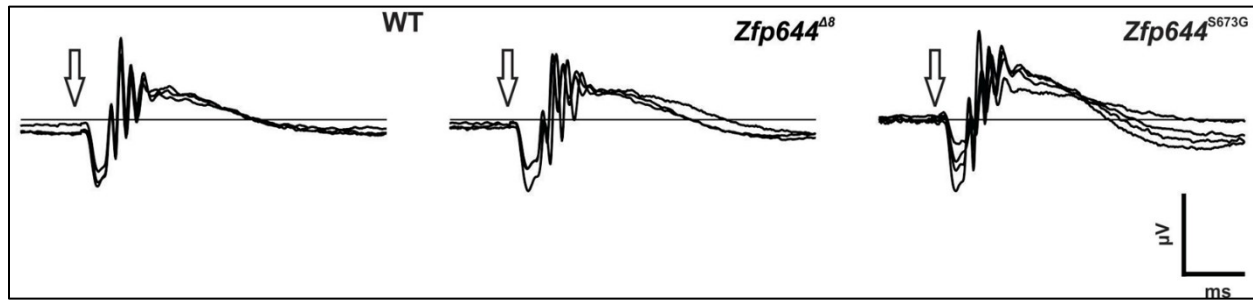


Figure 4.14. Functional analysis of retina showed no differences among genotypes. Function of retina was examined by ERG measurement in 21 weeks old animals and shows no difference between WT and transgenic animals. Example responses to single white flash (3.0 cd s/m²) are shown, arrows denote the time of stimulation. Scale bar 50 ms and 200 μ V. Figure is adapted from Szczerkowska et al. 2019

In addition, quantification of cell numbers in individual retinal layers (ganglion cells, outer layer cells and inner layer cells) did not reveal any significant differences (Fig.4.15.). These results suggest very low or no impact of Zpf644 on the function and morphology of retina.

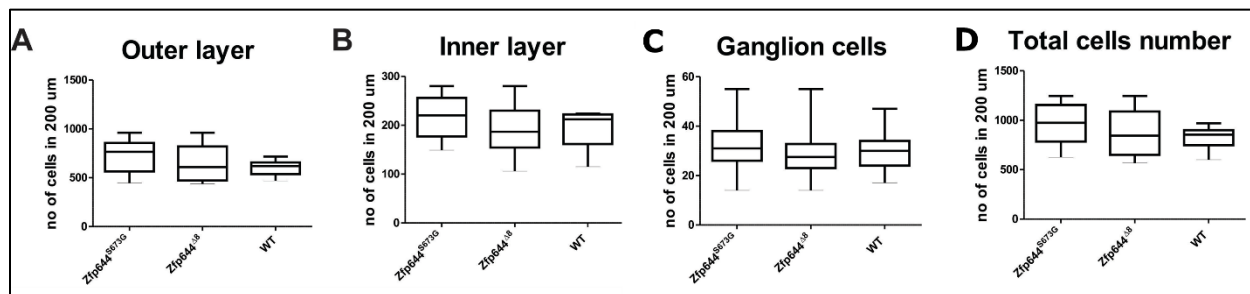


Figure 4.15. Evaluations of retina cell numbers showed no significant differences among genotypes. Cells were analyzed in four groups, in distance of 200 μ m: (A) cells in outer layer; (B) cells in inner layer; (C) ganglion cells; (D) and a total cells number. No significant differences were found. Figure is adapted from Szczerkowska et al.2019

To summarize this part of the study, we focused on evaluating the role of Zfp644 in vision. We created a mouse model mimicking human mutations associated with high myopia patients, as described previously. Additionally, we created a mouse model with a truncated form of the protein in order to analyze the impact of the protein in more detail. We carried out profound analyses of the eye and vision in these described models. We performed the expression analysis of an embryonic eye in crucial points of the eye development as well as in the adult organ. We then described the morphology of the eye as well as in the retina. We also analyzed the function of the retina by ERG analysis. As expected, no differences were found during this analysis. Myopia is a disease caused by elongation of the axial length of an eye. Therefore, we decided to measure different ocular parameters with ultrasound imaging method. This experiment allowed us to measure four ocular parameters i.e. axial length (AL), vitreous chamber depth (VCD), lens diameter (LD) and lens thickness (LT). We found significant difference in all of these, proving the causative role of Zfp644 in myopia.

4.5. Role of Zfp644 in mouse fertility

To further investigate the role of Zfp644 on mouse biological systems, we performed the analysis on already described *Zfp644^{Δ8}* mouse model and a novel full protein ablation mouse model, *Zfp644^{-/-}* (fig 4.1.C). Analysis of expression of the *Zfp644* protein in mouse reproductive system, performed in both a qualitative and quantitative way, revealed the expression in all parts of the murine reproductive system (Fig. 4.3).

***Zfp644^{Δ8}* influence the correct estrus phasing in female mice, but not the female reproductive system development.**

To reveal the impact of Zfp644 on the mouse reproductive system, first, the breeding performance was investigated. Homozygous mice were bred with control animals (with previously confirmed breeding performance) for a period of four months. Data collected from that experiment, did not show any differences between males from neither of the created transgenic lines. Moreover, females from the *Zfp644^{-/-}* line were also breeding successfully. However, when *Zfp644^{Δ8}* females were compared with control animals severe abnormalities were found. The breeding performance, size of the litter and viability of new born pups are highly reduced (Fig.4.16.E). Our analysis showed, that during the four months long breeding experiment, none of homozygous *Zfp644^{Δ8}* female produced a living offspring, while their controls had an average of three litters in that time. Moreover, we noticed a higher number of unsuccessful matting in *Zfp644^{Δ8}* females. Finally, we were able to trace pregnancy in *Zfp644^{Δ8}* females, however it occurs very rarely and the litter size is dramatically reduced to one, rarely two embryos (compared to an average of 12 in wild type controls). We also noticed that the pregnancy is prolonged. Wild type controls in our facility usually delivers between 18 to 20 days after fertilization, but *Zfp644^{Δ8}* females deliver between 20 to 22 days after fertilization. This observation suggests hormonal miss regulation in *Zfp644^{Δ8}* females. We were able to follow the birth of a small number of litters (due to low number of successful matting), and noticed, that pups are born alive and milk was spotted in their stomach. However, shortly after birth, the female sacrificed the pups. Therefore, we hypothesized, that the observed phenotype might be related to either disrupted hormonal homeostasis in mice or a malformation in the reproductive system. To confirm our hypothesis, we decided that a profound analysis of uterus (Fig. 4.16.A) and ovaries (Fig.4.16.B) in transgenic

and control females was required. We did not find any malformations in these organs. To further investigate the basis of the described phenotype, we analyzed the maturation of ovarian follicles. Follicles were divided into five groups, from primordial (less matured) to large antral follicles, which are the most matured, which are the next to be potentially released during ovulation. Surprisingly, no difference was found in ovarian morphometry analysis, suggesting no developmental malformations are a cause of the phenotype. Taking into account that *Zfp644*^{Δ8} females are subfertile, and in the case of pregnancy, the number of embryos is significantly lower, we decided to analyze the endometrium in pre- and post- implantation stages. We mated females with previously vasectomized males (to keep as much similarity between *Zfp644*^{Δ8} and control animals) and analyzed the size of the endometrium after three and four days after fertilization. Five females in each of three groups were analyzed, but no difference was observed (Fig.4.16.F, G). Based on these findings, we decided to further analyze the estrus cycle in *Zfp644*^{-/-} *Zfp644*^{Δ8} control females. As presented on a representative graph (Fig.4.16.D) *Zfp644*^{-/-} and control cycling does not differ much. However we can notice the high irregularity in *Zfp644*^{Δ8} females. Not only the phases change in an unexpected order, but also their length is not consistent and does not correspond with a normal cycle length. This data suggests, that a potential cause of the observed phenotype might be irregular cycling and/or lack or rare ovulation occurrence. The data taken together highly suggests that the cause of *Zfp644*^{Δ8} female subfertility is not a developmental malformation, but rather an irregularity in hormonal homeostasis.

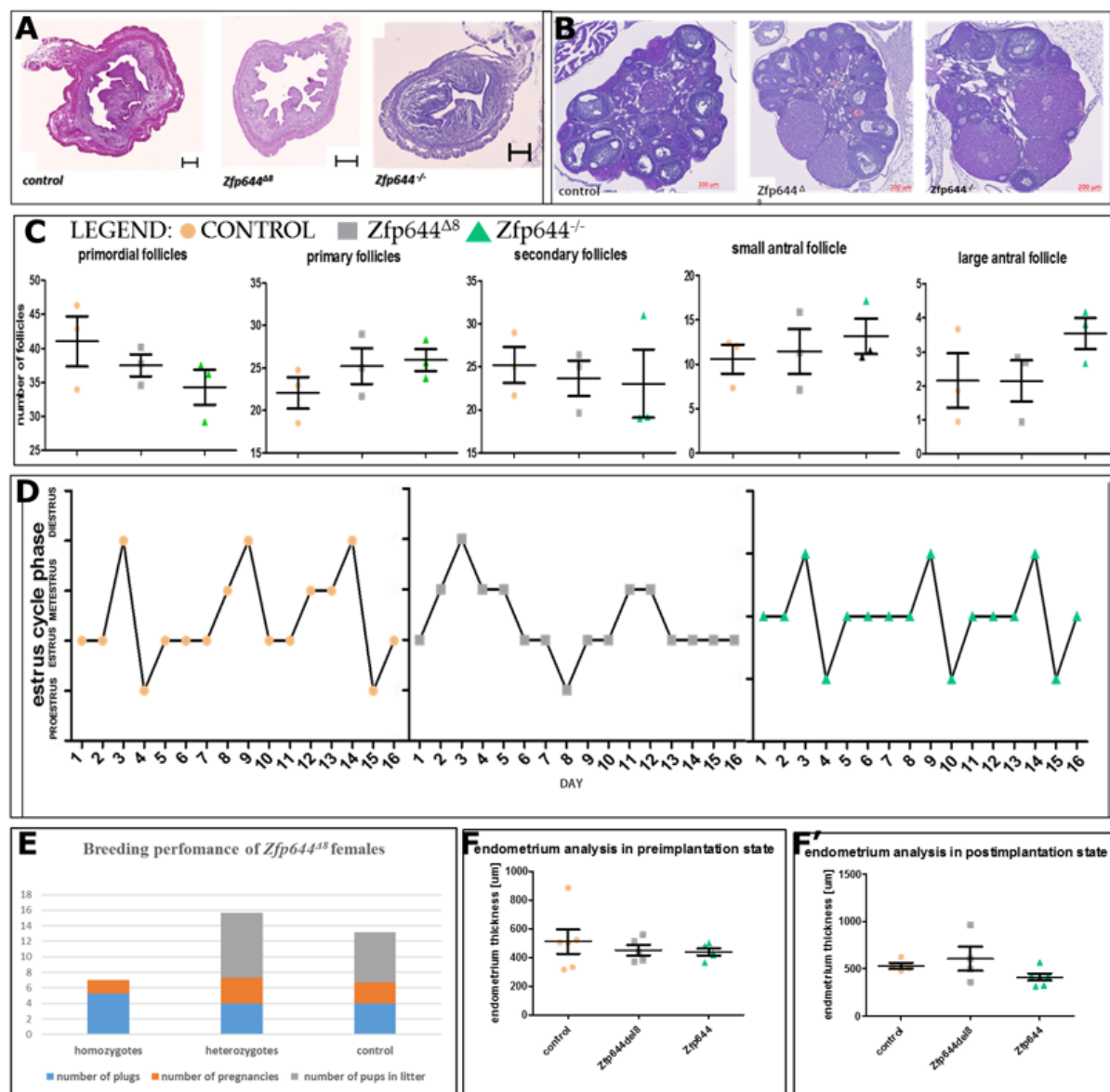


Figure 4.16. Strong abnormalities of estrus cycle and breeding performance were found in *Zfp644*^{Δ8} females. Morphological analysis of uterus (A) and ovaries (B) of *Zfp644*^{Δ8}, *Zfp644*^{-/-} and control animals showed no differences between genotypes. Scale bar 200 μm. No difference was found in morphological analysis. (C) Morphometry of ovaries of *Zfp644*^{Δ8}, *Zfp644*^{-/-} and control animals showed no difference between genotypes. (D) Analysis of estrus cycle in both transgenic mouse models and control animals revealed strong dysregulation in *Zfp644*^{Δ8} females. (E) Breeding performance of *Zfp644*^{Δ8} females during 4 month long experiment showed sever drop in breeding performance in *Zfp644*^{Δ8} females. Comparison of endometrium thickness in pre- and post-implantation stadium in *Zfp644*^{Δ8}, *Zfp644*^{-/-} and control animals. (F) Analysis of endometrium thickness in preimplantation stage. No significant difference was found. (F') Analysis of endometrium in post implantation stage. No significant difference was found.

***Zfp644*^{Δ8} subfertility can be partial rescue by ovarian transplantation**

To confirm our hypothesis of fully functional ovaries we decided to design an ovary transplantation experiment. The ovarian transplantation was performed in order to rescue the phenotype (Fig.4.17). The experiment was performed in two groups. The first group consists of control animals as recipients of transplantation, and *Zfp644*^{Δ8} females as donors of ovaries. The second group, were *Zfp644*^{Δ8} females as recipients and control females as donors. The experimental set up is also presented on a scheme below. Breeding performance after the transplantation in each group is presented on bar plots.

We were able to partially rescue the phenotype, by transplantation of *Zfp644*^{Δ8} ovaries and perform successful breeding and weaning of offspring. As could be expected based on data presented in the previous chapter, transplantation of control ovaries did not cause any improvement in breeding performance of *Zfp644*^{Δ8} females. The results of the transplantation experiment and the presented data taken together clearly suggest the causative effect of hormones and not developmental malformations of female reproductive system.

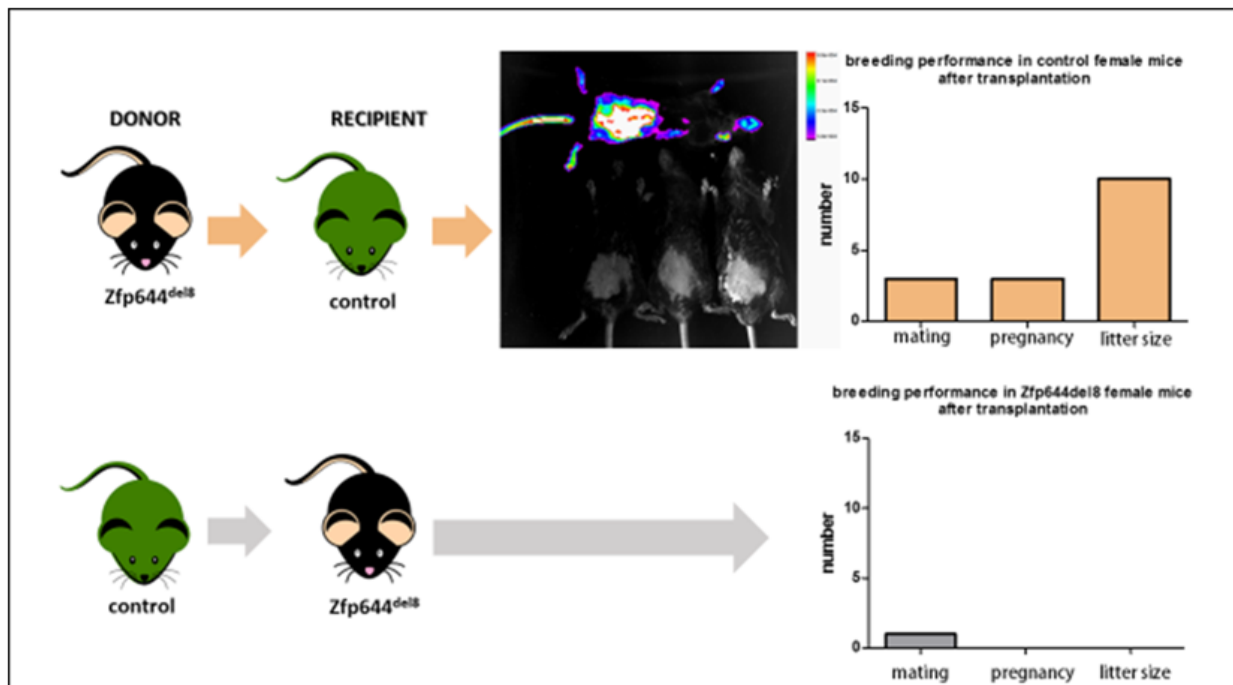


Figure 4.17. Ovarian transplantation rescue the fertility phenotype in *Zfp644*^{Δ8} females. Representative graph of rescue experiment; on the left side of the figure and results presented as an average on bar plots presented on the right side of the figure. Green color of control mouse represents the mouse with green fluorescent protein,

ubiquitously expressed, that could be visible on attached image. The fluorescence help to quickly identify the origin (donor or acceptor) of pups, further confirm by genotyping.

***Zfp644*^{Δ8} disrupt correct prolactin circulating levels during estrus cycle and pregnancy.**

To further analyze the hormonal parameters in female mice, we examined the plasma levels of five female sex hormones necessary for correct phase changes in mice as well as successful fertilization. The examined hormones were: progesterone, 17-β-estradiol, LH, FSH and prolactin in each of the four estrus cycle phases. A significant difference was found between the genotypes and estrus cycle phases only in *Zfp644*^{Δ8} females, but not in *Zfp644*^{-/-} or control animals. (Fig.4.17.A). Moreover, an interesting tendency in prolactin levels was found (Fig.4.17.B). Between proestrus and estrous phases, a peak of prolactin should be observed. This general rule, can be easily observed in both control and *Zfp644*^{-/-} plasma analysis presented on the graph. However, *Zfp644*^{Δ8} female's plasma levels suggest an opposite trend in prolactin cycling (Fig 4.17.B). These findings suggest dysregulation in release of the prolactin hormone. We decided to analyze the mammary gland, as this organ is influenced by prolactin the most during pregnancy. First the examination of the mammary gland of nulliparous female at 9 weeks of age was performed (Fig.4.17.C). Here we present a representative picture of *Zfp644*^{Δ8}, *Zfp644*^{-/-} and control females. Similar to analysis of morphology of uterus and ovaries, also mammary gland did not show any malformations between the groups. To further investigate if the observed dysregulation of prolactin levels in *Zfp644*^{Δ8} females might influence the role of mammary glands in pregnancy, we decided to examine the size of mammary gland in pregnant females. As presented before (Fig.4.17.E) *Zfp644*^{Δ8} females are, although rarely, able to get pregnant, therefore analysis of mammary glands at E18.5 was challenging but possible (Fig.4.17.D-E). The results, presented by the representative image of each examined group as well as quantitative representation of the phenotype are striking. We observed not only a significantly smaller area of mammary gland, but also a loss of the structure of the ducts. Moreover, expressed by color coding, depth of the ducts is severely depleted in *Zfp644*^{Δ8} female's organs. It was previously described, that estrogen, progesterone and prolactin are the three main hormones influencing growth and development of mammary gland. Estrogen is almost exclusively crucial for development. However progesterone and prolactin, whose tight cooperation was reported not only in mammary glands, are more significant during the reproductive cycle and even more

during the pregnancy. The presented results might suggest a growing significance of progesterone during the pregnancy of *Zfp644*^{Δ8} mice and should be further examined. To fully exclude developmental malformations as a cause of mammary gland failure during the pregnancy, we prepared organoids from mammary gland of control and both *Zfp644* transgenic mouse lines. In organoid culture, all conditions were kept the same. To simplify, we can say that in organoid culture, unlike mammary gland *in vivo*, all necessary substrates, such as hormones, were the same for each group. Therefore the growth of organoids is based only on the abilities of the organ itself. Analysis of growth, as well as the performed lactation assay did not reveal any changes between the groups, which might suggest the importance of prolactin inheritance in the animals, which is impossible to observe in organoid culture (data not shown).

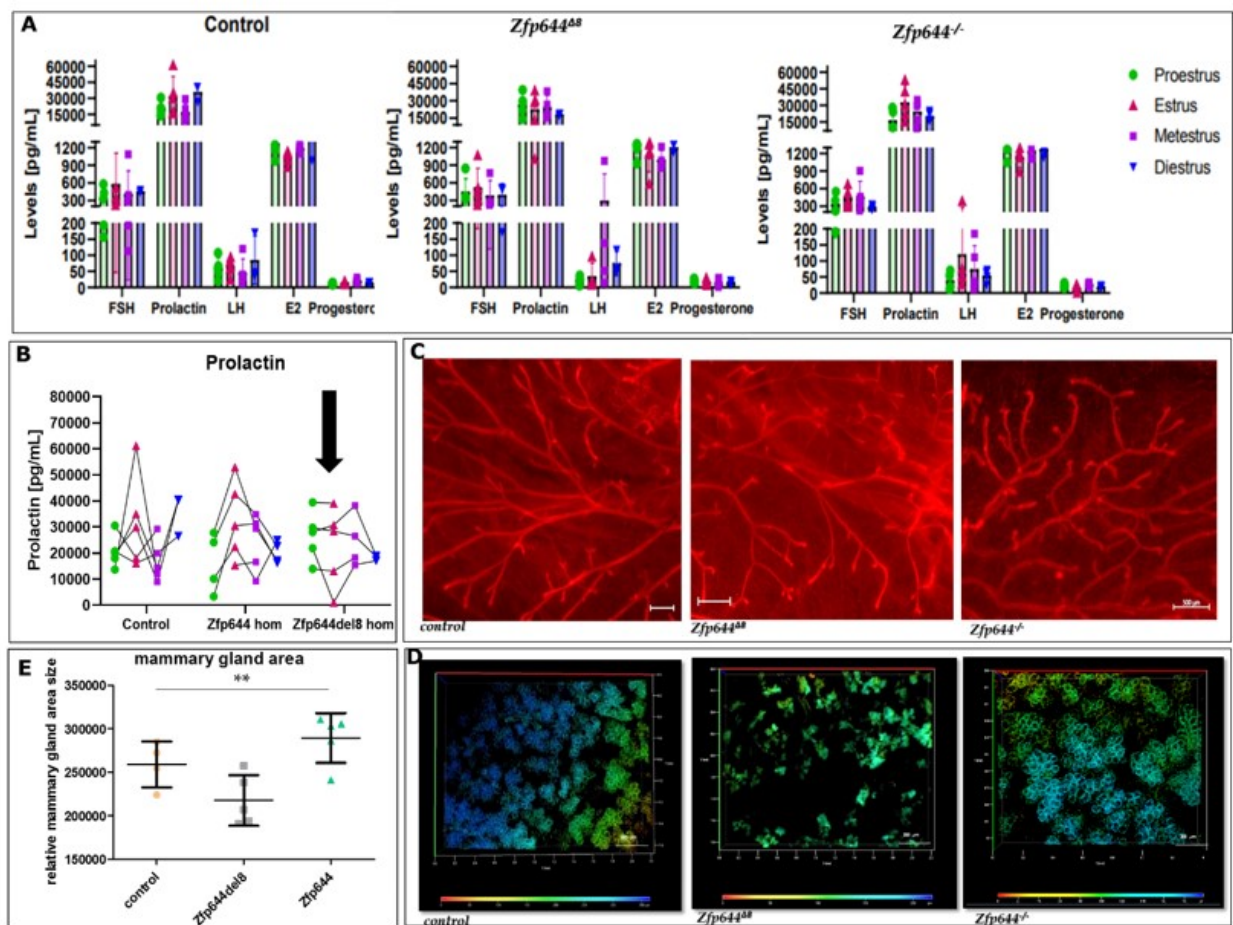


Figure 4.18. Analysis of hormonal levels and mammary gland in pregnant females shows significant differences in *Zfp644*^{Δ8} animals. (A) Analysis of hormonal levels in different estrus phases. Data was analyzed with Mixed

ANOVA Interaction that for control $p=0.0069$; for $Zfp644^{-/-}$ $p=0.0010$ and for $Zfp644^{A8}$ $p=0.2593$. **(B)** Detailed analysis of plasma level of prolactin during different phases of murine estrous cycle. **(C)** Representative images of mammary gland of nulliparous females at 9 weeks of age. Scale bar 500 μm . **(D)** Representative images of mammary gland collected from pregnant females 18 days after fertilization. Scale bar 200 μm . Depth of the ducts is color coded. **(E)** Analysis of quantification of size of mammary gland of pregnant females. Data analyzed with one way ANOVA showed significant difference between the means of examined groups $p = 0.0067$.

Progesterone replacement therapy rescues the subfertility phenotype in $Zfp644^{A8}$ females.

To further understand the impact of hormonal misbalance in $Zfp644^{A8}$ females, we performed the rescue experiment with hormonal replacement therapy. It was previously described that both prolactin and progesterone are highly connected, especially during pregnancy¹⁰⁵. Our promising data of mammary gland examination showing the potential influence of hormonal balance on a late pregnancy development of the glands directed us to further analyze the pregnancy suppression. The role of progesterone in maintaining the pregnancy and its significance in infertility treatment are commonly discussed and used in human medicine. Therefore, we decided to test progesterone and 17- β -estradiol (as a negative control) pellets with release in 60 days. Placebo pellets with same time release were used as controls. Moreover, combination therapy with both 17- β -estradiol and progesterone pellets simultaneously implanted were used. During this time females were mated at least twice and, in the case of pregnancy, monitored until weaning of a litter. The hormonal replacement therapy with use of progesterone resulted in a rescue of $Zfp644^{A8}$ female sub-fertility. Results are presented on a scheme below (Fig.4.19).





SUCCEFUL MATTING						
			Control	Zfp644 ^{Δ8}	Zfp644 ^{-/-}	
	+	E2	→	-	-	-
	+	P4	→	+	+	+
	+	E2 + P4	→	-	-	-
	+	placebo	→	+	-	+

Figure 4.19. Hormonal replacement therapy can be applies as a rescue of the fertility phenotype in *Zfp644*^{Δ8} females. Experimental set up and results of mattings. The proposed rescue experiment by hormonal replacement therapy with progesterone (P4) resulted in successful mattings and weaning of the offspring. The effect was not visible when 17-β-estradiol (E2) nor placebo were used.

***Zfp644* depletion do not result in difference in H3K9 demethylation in mouse**

Olsen et al.¹² suggested that depletion of ZNF644 results in a decrease of H3K9 demethylation, independently of G9a (expression not changed). Our experiments on cells proved that concept (data not shown). However, the analysis of methylation in cells could be translated to *Zfp644* full knockout (*Zfp644*^{-/-}) mouse model, however not to *Zfp644*^{Δ8} mice. Therefore, we decided to conduct a similar analysis of total demethylation level in MEFS cells derived from both the examined *Zfp644* mutant mouse lines. The results did not show any difference in H3K9 demethylation marker between *Zfp644*^{Δ8}, *Zfp644*^{-/-} and control cell lines. The data suggest, that the total expression of H3K9 demethylation in the examined mouse derived cell lines is not affected (Fig.4.20). These findings could support our hypothesis that *Zfp644* is substituted by another factor in the living organism.

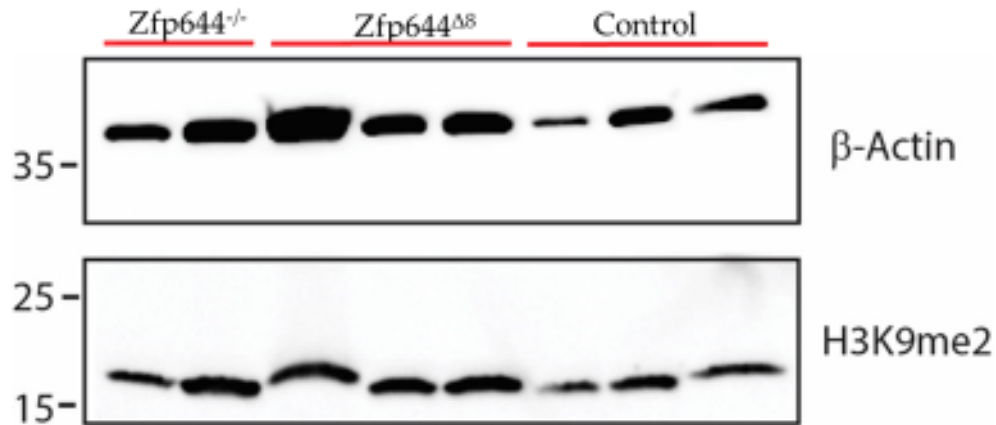


Figure 4.20. H3K9 demethylation pattern in MEFS cells derived from *Zfp644* transgenic mouse models shows no differences between the genotypes. Data kindly provided by P.Kaspar.

To examine if the observed trend remains visible also in adult animals, we tested the expression of H3K9me2 marker in testes samples from 16 week old males from each transgenic group (Fig.4.21.). We found the expression of H3K9me2 were similar in all samples; similarly as in MEFS cells.

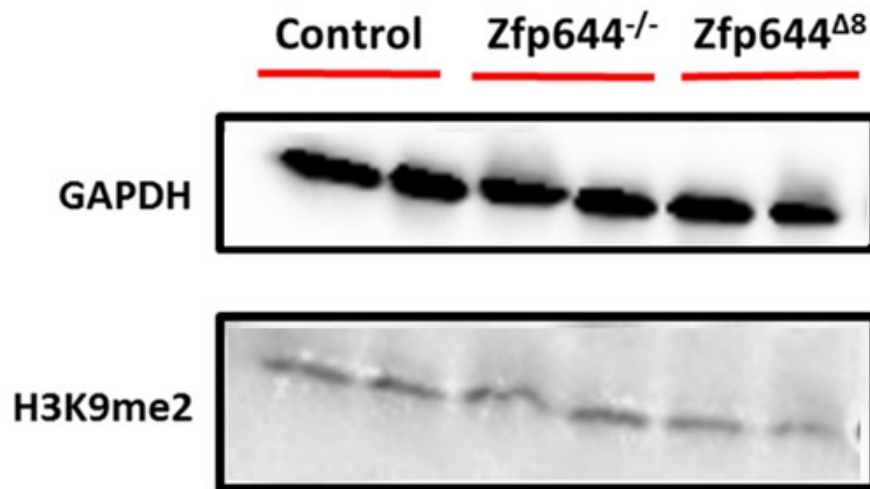


Figure 4.21. G9a protein expression and H3K9 demethylation pattern in testes samples from adult males from each of *Zfp644* transgenic mouse models shows no differences between the genotypes.

Moreover, we examined the methylation pattern in samples collected from pregnant females nine days after mating occurred. Mammary glands from females were collected and methylation pattern marker was examined. Again, we did not find any differences in the expression of total H3K9 demethylation marker between examined groups. The slight differences that can be observed in H3K9me2 marker were caused by a different amount of loaded protein (visible on a GAPDH expression).

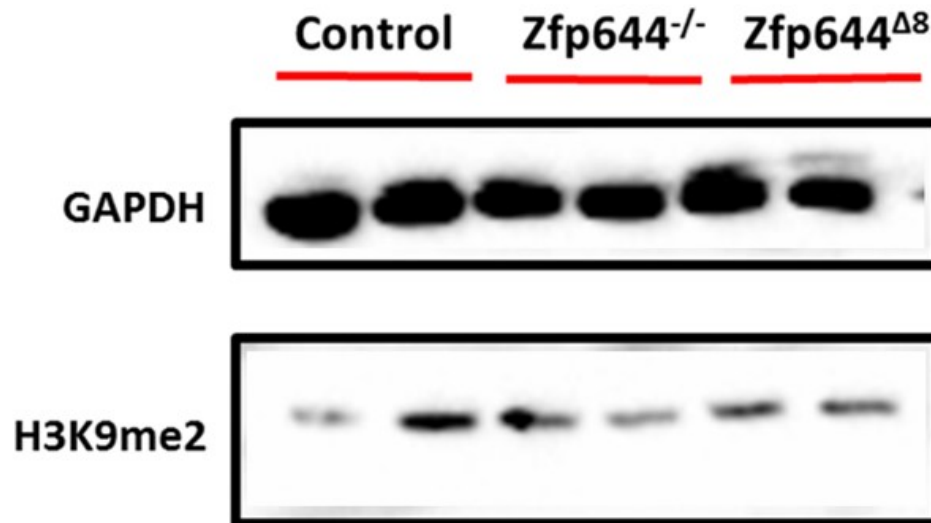


Figure 4.22. H3K9 demethylation pattern in mammary glands samples from pregnant females from each of *Zfp644* transgenic mouse models shows no differences between the genotypes.

Taken together all results suggest, that depletion of *Zfp644* or its truncated form, do not influence total H3K9 demethylation rate. However, to elucidate the impact of the mutations on single genes further analysis would need to be completed. Currently, we are preparing mouse organ samples from both *Zfp644* mouse transgenic lines for chromatin immunoprecipitation experiments. Until now, the experiment could not be performed due to lack of an anti- *Zfp644* antibody. Recently, the tagged recombinant protein of ZNF644 (full length and one imitating *Zfp644*^{Δ8} situation; explained in following chapter) was prepared following the cooperation with other laboratory. We plan to use both of these constructs for chromatin immunoprecipitation analysis. We believe, that results of this experiment could shed a light on a detailed methylation profile of single genes. The results of this analyses was not available before this thesis was submitted.

***Zfp644*⁴⁸ might interfere the protein-protein or protein-DNA interactions in mice**

To reveal the molecular mechanism behind the observed phenotype, we hypothesized that *Zfp644*⁴⁸ mutation in mice led to either a difference in methylation of a single or a couple of genes, but not the total methylation status or disruption in binding of a partner. We employed an *in silico* approach and analyzed publically available ChIPseq data from HEK293T cells on G9a, ZNF644¹ and ER (estrogen receptor). Schematic representation of the results is presented on a Venn diagram (Fig.4.23). As presented before, a significant overlap between G9a and ZNF644 suggests the strong co-operation between the transcription factor and the methylation complex. Among others, a few genes from the overlapping area are highlighted. Disruption of their expression could be a potential cause of the observed phenotype. However, further experiments are necessary to reveal this. Interestingly, we found an overlap of peaks common for all three examined proteins. PPP5C and DHRS9 are both related to steroid hormones. Moreover, presented previously data from RNAseq (Fig.4.6) showed significant differences in genes related to hormonal balance or fertility, such as Gper1, Ghrh, Bcar1, Ovgp1. This data might support our hypothesis of disrupted expression and/or binding of a single or a small amount of genes due to *Zfp644*⁴⁸ mutation.

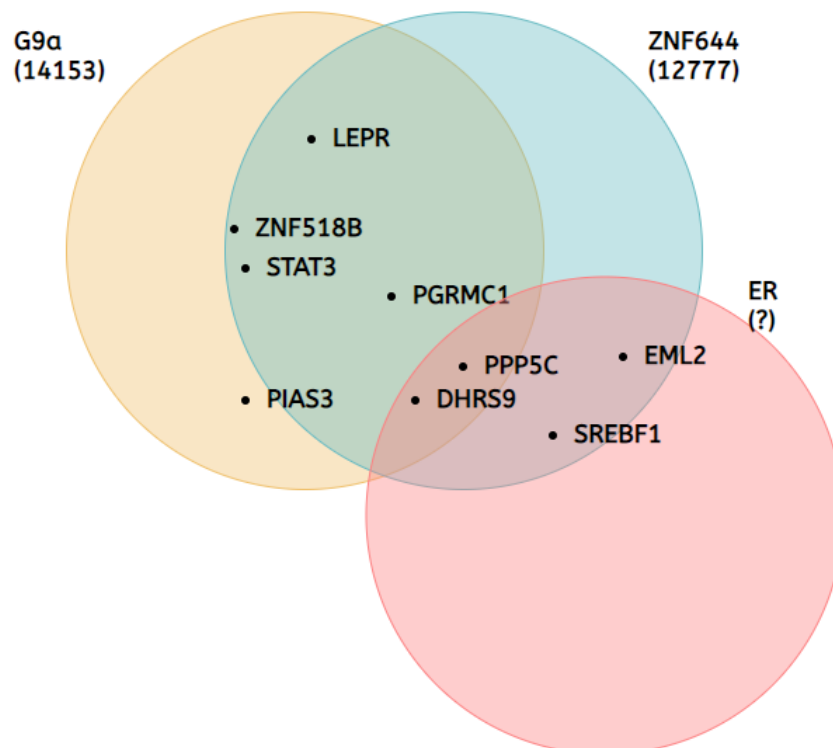


Figure 4.23. Analysis of ChipSeq data from G9a, ZNF644 and ER from HEK293T cells shows many genes that are impacted by all three investigated genes: G9a, ZNF644 and estrogen receptor. Moreover, we found that many genes are related to hormonal balance and fertility, suggesting possible co-operation between the genes and ZNF644 gene.

Revealing of protein-protein interactions of Zfp644 was challenging due to the lack of antibody that could serve for immunoprecipitation. Currently, the recombinant proteins of both full length ZNF644 and one that mimics the *Zfp644*^{Δ8} mutation present in mouse were prepared. The preliminary results suggest that both proteins are the correct size and might serve for further studies on protein-protein interactions. The proteins have a tag on both the N- and C- termini. On the C-terminus there is streptavidin, and on the N-terminus either a GST or His tag is present. We plan to use these recombinant proteins for pull down studies that could help to elucidate the protein-protein interactions of ZNF644 and the differences between the full length and the potentially truncated form mimicking the *Zfp644*^{Δ8} mutation. The results of this analyses were not available before this thesis was submitted. What caught our attention, when analyzing the ZNF644^{Δ8} recombinant protein, a lot of complexes with DNA were observed. Knowing, that five out of eight zinc fingers remained in that construct, we could assume that many unspecific bindings to DNA occurred. This could explain why we observe the phenotype in *Zfp644*^{Δ8} and not in *Zfp644*^{-/-} mice. However, further experiments to prove that would be necessary.

As the protein-protein interactions seems to be crucial for understanding of molecular mechanism behind the observed phenotype, we decided to perform immunoprecipitation by a G9a antibody (Fig.4.24). We used MEFS cells derived from both *Zfp644* mutant mouse lines and compared them with control samples. Moreover, when analyzed, results from MEFS cells were compared to IgG controls to remove the unspecific bindings. Interestingly, we found overexpression of Cbx5 transcription factor in *Zfp644*^{-/-} samples, when compared to wild type controls. This could suggest, in agreement with our hypothesis, that in the case of complete depletion of *Zfp644* in mouse, another transcription factor is substituting and fulfilling the role of the missing *Zfp644*. However these findings are only preliminary results. It needs to be clearly stated that even though the method seems to be working correctly (G9a, GLP and Wiz were pulled down in all samples), the Zfp644 was not discovered in any of the samples. Moreover, almost

no zinc finger proteins were visible in the results of the experiments, suggesting that the condition of the experiment should be improved. Currently, we decided to use the same samples for RNAseq analysis, to see the differences between the groups with a more sensitive method. The results of this analyses were not available before this thesis was submitted.

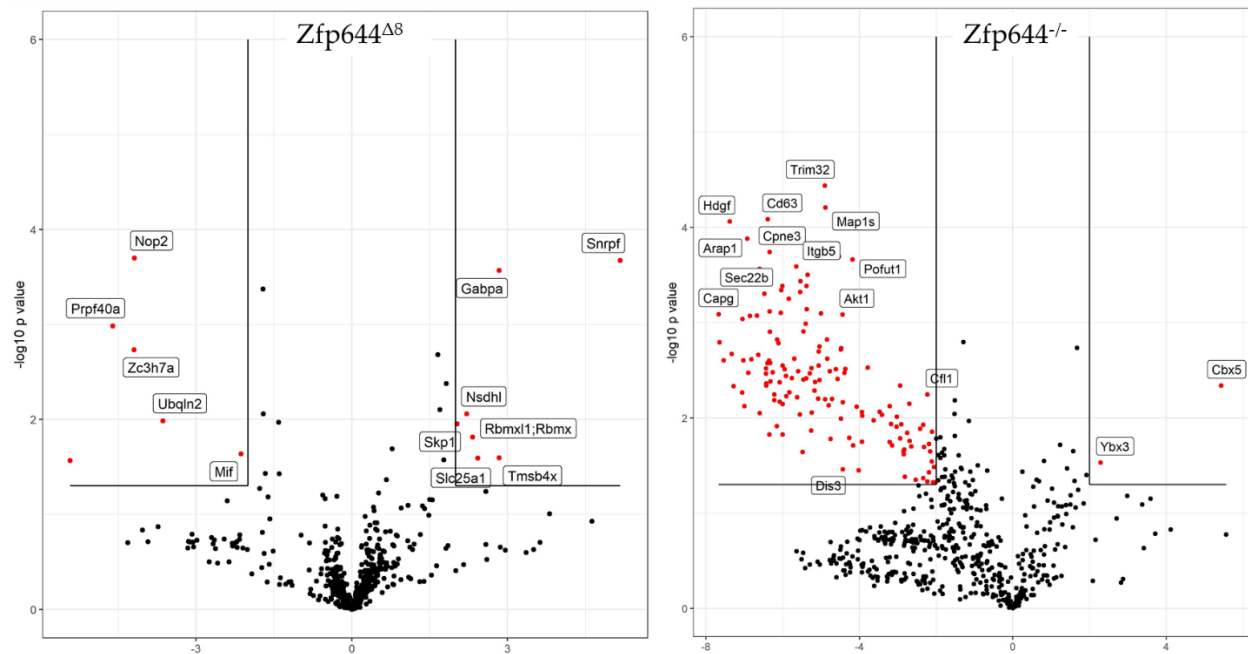


Figure 4.24. Significantly expressed genes found in immunoprecipitation by G9a antibody. Analyses were done on MEFS cells derived from *Zfp644* $\Delta 8$ (left side) and *Zfp644* $^{-/-}$ (right side) mutants. Proteins with significance difference in expression are presented in the boxes, the left side of the plot indicates the downregulation and the right side of the plot – the upregulation. The amount of differently expressed proteins is much lower in *Zfp644* $\Delta 8$ derived MEFS cells. Among the other proteins highlighted in *Zfp644* $^{-/-}$ analysis, *Cbx5* seems to be the most promising for further investigation. Data kindly provided by P.Kaspar.

To summarize, this part of the study was focused on describing the infertility phenotype found in *Zfp644* $\Delta 8$ females and further analysis of the molecular mechanism behind it. We were able to describe an impact of *Zfp644* and its mutation (*Zfp644* $\Delta 8$) on the development of the female reproductive system in mouse. Moreover, our profound breeding analyses showed severe decrease in breeding performance of female mice, potentially caused by hormonal misbalance, mainly

by prolactin and progesterone. Finally, we proposed two rescue experiments which helps to restore female subfertility in mouse. Our data taken together suggest, that the observed phenotype is caused not by malformations of the female reproductive system in mouse, but irregularities in hormonal homeostasis. Finally, we took multiple attempts to elucidate the molecular mechanism behind the observed phenotype. We did not find differences in total H3K9 demethylation expression in MEFS cells, nor in adult mouse samples. *In silico* analyses and performed IP experiments were not enough to elucidate the role of truncation (*Zfp644*^{Δ8}) and the difference between the truncation and full protein ablation (*Zfp644*^{-/-}). This question remains open at the time of handing over the thesis and are further commented on in the Discussion section. Moreover, the manuscript of fertility study was prepared and include at the end of the thesis. It would be revised and filled with new data before possible submission in the future.

4.6. Role of WIZ in embryonic development

Wiz is a transcription factor working with G9a/GLP complex simultaneously with, the main focus of this thesis, ZNF644. In this complement study, our aim was to elucidate the role of Wiz knockout on mouse development as well as the impact on methylation status in embryonic development. The data is fully presented in the attached publication (Bukova et al. 2021). Here, only the most relevant data is shown.

Wiz deficiency causes growth retardation and craniofacial defects

Novel Wiz knockout model was created by CRISPR/Cas9 technology and analyzed by a standardized search¹³⁹ for embryonic lethality, as suggested in previous studies¹⁶. The analyzed genotype distribution did not show any significant differences until E18.5, however dead *Wiz*^{-/-} embryos were observed from stage E12.5. Moreover, strong growth retardation at E18.5 was observed, which results in almost 25% lower Crown Rump Length (CRL) before birth compared to WT embryos.

The analysis of embryos revealed malformation visible from embryonic stage E14.5. The most striking abnormality was delayed horizontalization in *Wiz*^{-/-} palatal shelves which remained lateral to the tongue (Fig.4.25.A), which was never observed even in later stages. Additional analyses of embryos at E18.5 revealed more severe craniofacial defects, including shorter snout morphology and the underdevelopment of eyelids. From the *Wiz*^{-/-} embryos harvested at E18.5 approximately 60% showed full cleft palate and 40% showed incomplete palatal shelf fusion (Fig.4.25.B).

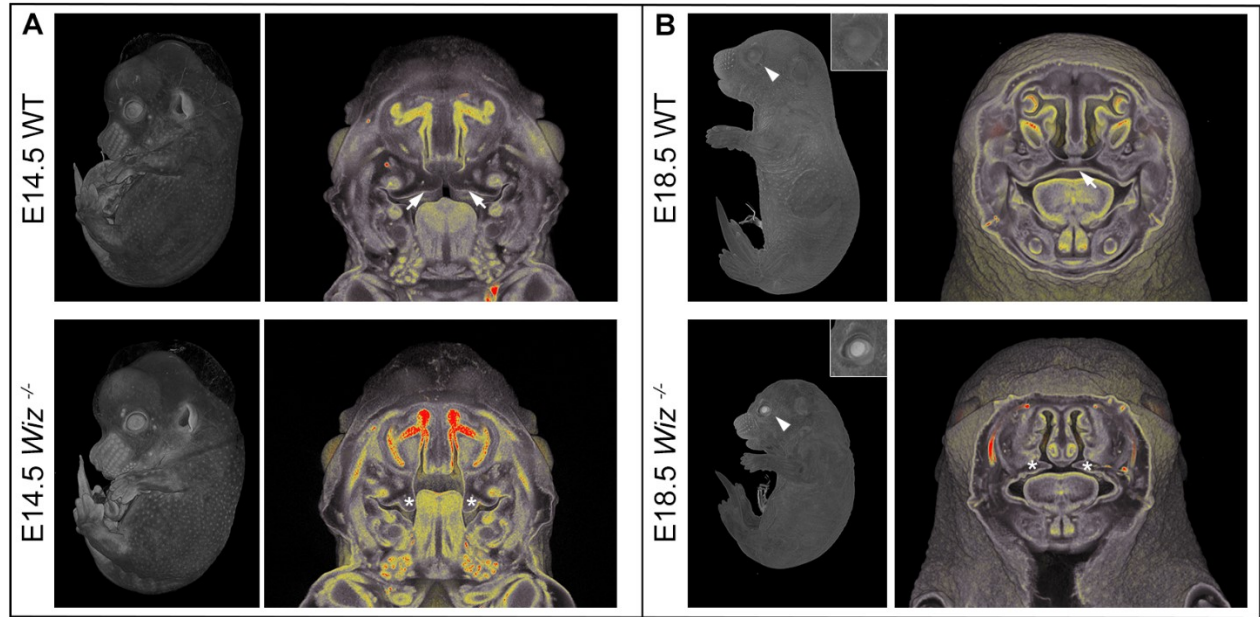


Figure 4.25. *Wiz* deficiency leads to developmental defects especially in craniofacial area, growth retardation, and embryonic subviability. MicroCT images of embryos at different embryonic stage: **(A)** E14.5 embryos. White arrows point to palatal shelves of WT embryo in proper horizontal position on top of the tongue. White asterisks indicate palatal shelves of *Wiz*^{-/-} embryo remaining in vertical position along the tongue. **(B)** E18.5 embryos. White arrowhead points to the eyelids, properly developed in WT and cleft in *Wiz*^{-/-} embryo. Detail of the eye is showed in the top right corner. White arrow points to fully fused and formed palate of WT embryo. White asterisks indicate severely hypomorphic palatal shelves of *Wiz* KO embryo. Figure is adapted from Bukova et al. 2021.

WIZ is expressed in palatal shelves and overlaps with G9a/GLP and suppress the methylation pattern in developing palate epithelium.

To study the impact of *Wiz* knockout on craniofacial development, analysis of expression of *Wiz*, *G9a* and *GLP* proteins with *in situ* hybridization on histological sections of developing palate at E13.5 and E14.5 were as performed. Nuclear localization of *Wiz* in palatal shelf was detected, both in neural crest derived mesenchyme and in palatal shelf epithelium with a stronger expression in the epithelial layer which later form the roof of oral cavity (Fig.4.26.A, arrows). Moreover, analysis of *G9a* and *GLP* expression showed an overlapping pattern with *Wiz* and an increased expression at the oral side of palatal shelves (Fig.4.26.B-C).

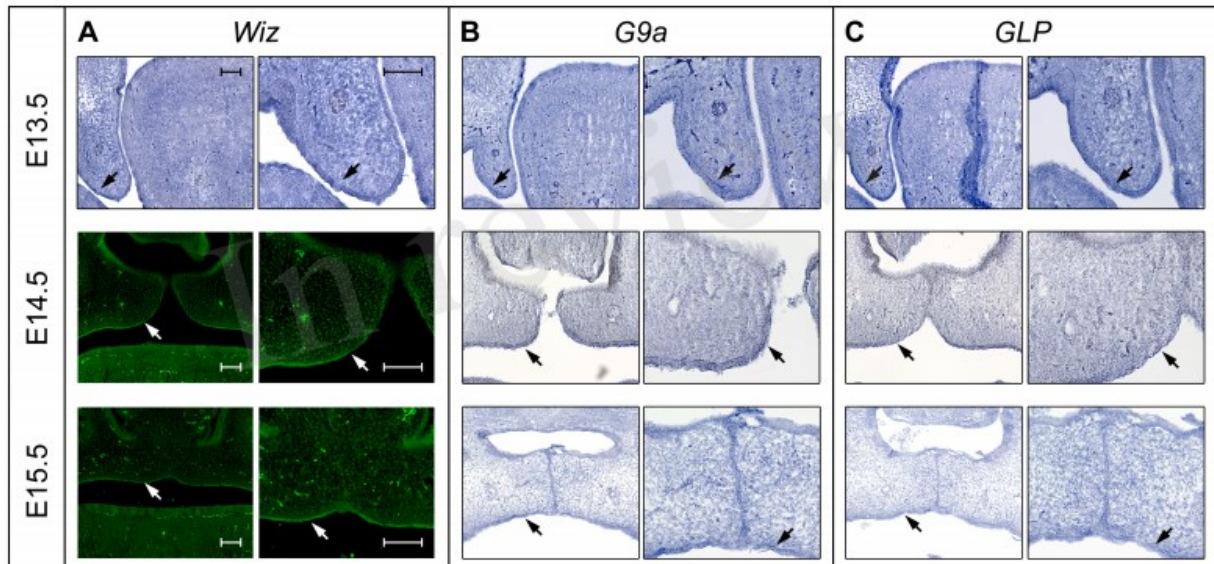


Figure 4.26. Expression pattern of Wiz, G9a and GLP on palatal sections shows an overlapping pattern of G9a/GLP expression with Wiz. *In situ* hybridization on palatal sections and immunofluorescent stained palatal sections of E13.5 WT (upper panels), E14.5 (middle panels), and E15.5 (lower panels) palatal sections. **(A)** strong expression of Wiz in the epithelia on oral side of palatal shelves (black and white arrows). Expression pattern of **(B)** G9a and **(C)** GLP showing an overlapping pattern of G9a/GLP expression with Wiz (black arrows). Scale bar represents 100 μ m and applies for all images. Figure is adapted from Bukova et al. 2021.

To further address, whether co-expression of components of the complex can affect the methylation pattern the following experiments were performed. Published data suggest that the main focus of the complex is mono- and demethylation of H3K9, thus histological sections of embryos between E13.5 and E15.5 were compared for the pattern, as this period is crucial for palatal development. Observations of stages E13.5 and E14.5 revealed a decrease of the signal in the *Wiz*^{-/-} epithelium compared to positive areas in WT (Fig.4.27.A,B, arrows) corresponding to the future oral surface of the shelves both before and after horizontalization. Observations of the epithelial layer of palatal roof after fusion in WT versus shelf epithelium of *Wiz*^{-/-} embryos at E15.5 showed a severe reduction of mono- and demethylation marks (Fig.4.27.C, arrows). As presented on the expression analysis (Fig.4.3), stronger expression of the complex's components in palatal shelf epithelium corresponds to a more severe decrease in methylation marks expression, suggesting the role of Wiz and G9a/GLP during palate development. Nevertheless, the precise molecular mechanism of this action needs further examination, likely at single cell level and by unbiased transcriptomics.

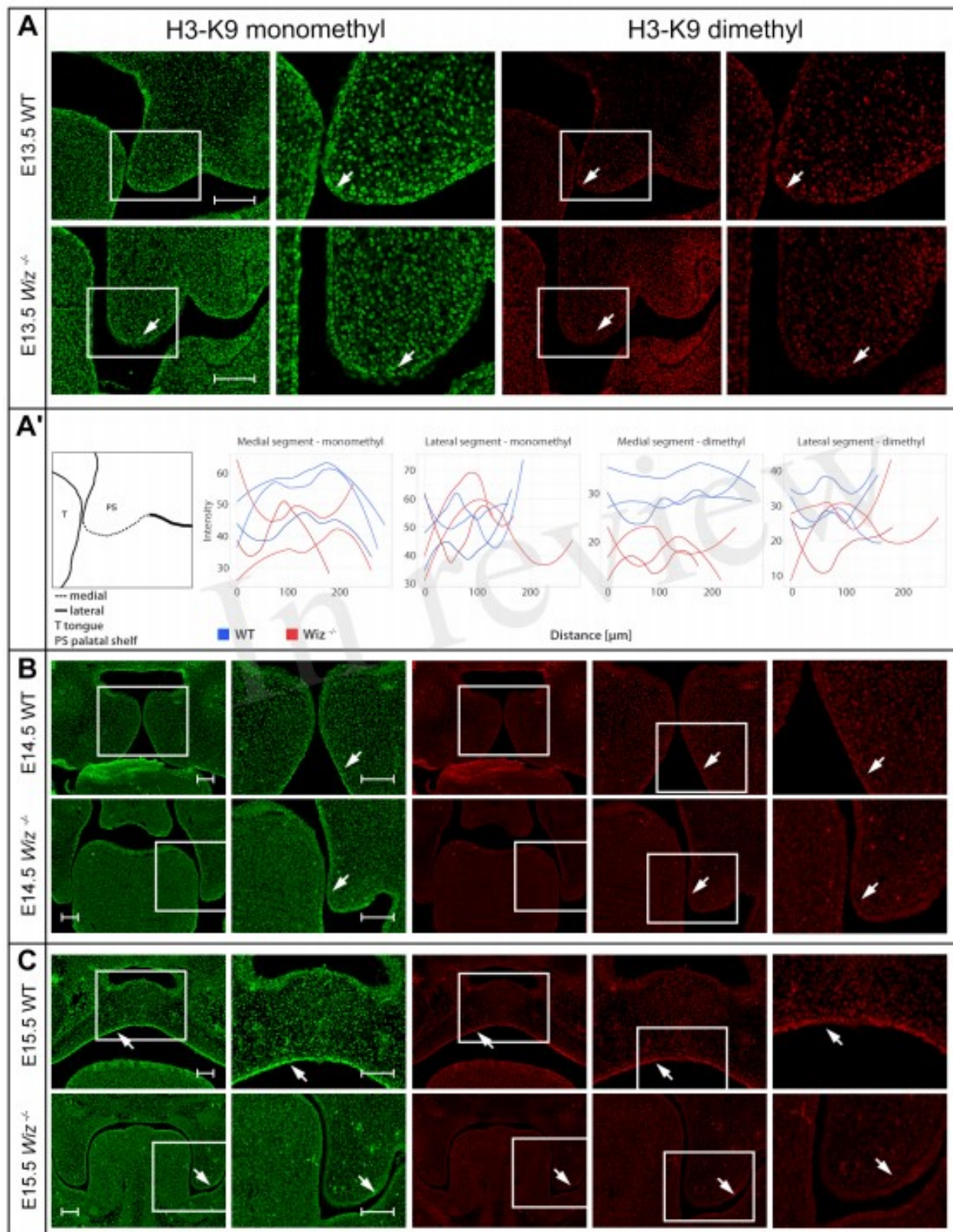


Figure 4.27. Analysis of H3K9 methylation pattern in palatal shelves suggests the role of Wiz and G9a/GLP in palate development. Immunofluorescent double stained palatal sections of (A) E13.5, (B) E14.5, (C) E15.5. WT (upper panels) and Wiz^{-/-} (lower panels) embryos for mono- and dimethylated H3-K9. Second column for each staining displays detailed image from the first column labeled with white rectangle. In (B,C), last column represents magnified images from the area labeled with white rectangle in previous column. (A') Quantification of methylation marks in E13.5 palatal sections. A schematic cartoon showing medial and lateral segments used for quantification can be appreciated on the left. Graphic representation of spectral intensity quantification for medial and lateral segments of mono- and dimethylated H3-K9, respectively are shown in the rest of panel. Figure is adapted from Bukova et al. 2021

In conclusion, the methylation pattern of H3K9 in the developing mouse craniofacial area was followed and showed its suppression in developing palatal shelves. Moreover, the impact of Wiz protein knockout on G9a/GLP complex action in craniofacial development was analyzed. Co-expression of G9a/GLP complex and Wiz protein in the palatal shelf was described. Furthermore, analysis of the embryo development in order of Wiz knockout in mice and reported malformations in orofacial areas, especially epithelia of developing palatal shelves were performed. The connection between epigenetic chromatin modification and craniofacial defects is very complex, therefore further research to reveal the detailed mechanism and the specific cell population involved in the palatal process would be interesting to provide. The data still provides an open door for further analysis of cleft palate mechanism and the involvement of methylation in the process.

5. Discussion

5.1. Main results of the thesis

Three mouse models were designed and produced to conduct the study into *Zfp644* function. We analyzed the expression profile of *Zfp644* in both a quantitative and qualitative way. We found that *Zfp644* is ubiquitously expressed in adult mouse samples derived from both sexes. We also reported the presence of *Zfp644* in mouse embryos and the developing murine eye (Fig.4.3). Our first aim was to evaluate the impact of mutations in the *Zfp644* gene on developing a high myopia phenotype. As described before, during GWAS studies, 12 mutations in *ZNF644* gene have been found and connected to patients with high myopia. To further elucidate the role of Zinc Finger Protein 644, we applied TALEN technology to create a mouse model mimicking one of the human mutations found in patients with high myopia. To complement the study, we also created a mouse model with a potentially truncated form of the protein. These are the first transgenic mouse models of *Zfp644* to be described. Study of the impact of *Zfp644* on an animal model has only been conducted previously on a zebrafish model deficient for *znf644*¹². To investigate the molecular mechanism of *ZNF644*, Olsen et al.¹² established two different morphant models (MO) of *znf644*, based on two *znf644* isoforms (a and b) whose phenotype was severe and included changes in the developing retina, midbrain, and eye size. Both *znf644a*-MO and *znf644b*-MO showed signs of microphthalmia and disrupted midbrain morphology. Therefore, we conducted a profound study including the analysis of morphology and thickness of retina, as well as other *in vivo* examinations of eyes, e.g. OCT or ERG analysis. No impact of the mutations in *Zfp644* on mouse was found in described examinations. The data suggest that *Zfp644* mutations the described in the study has a much milder or even no effect when compared to phenotype observed in lower animals.

As the main focus of the study was to elucidate the impact of *Zfp644* mutations on the myopia development, we proceeded with detailed vision analysis. The most straight forward results of myopia examinations were obtained by *in vivo* analysis of ocular parameters by ultrasound imaging. Axial length (AL), vitreous chamber depth (VCD), lens diameter (LD) and lens thickness (LT) were analyzed in both models. We showed that both *Zfp644* mouse models carry the signs of myopia and the phenotype is stronger in *Zfp644*^{Δ8} mice, than in the point mutation model. Moreover, we also showed that the measured ocular parameters are significantly different in heterozygote animals when compared to WT animals, which corresponds with genetic conditions reported previously^{6,9}.

The created mouse models, seems to be an useful tool for further myopia studies, as the number of mouse models, that can be used for myopia studies is limited^{97, 140, 98, 99, 100, 101}. The myopia in mice could be studied also after induction by e.g. goggles^{141, 142} but in contrast to the myopia presented by us in *Zfp644* transgenic models, no developmental or genetic factors can be studied in that case.

The presented data focused on visual examination, did not reveal the molecular mechanism of *Zfp644*. To further continue the study, we decided to create and include into the examinations third mouse model with functional ablation of *Zfp644* protein. The difference between the models was described in detail in previous chapter and showed on figures (Fig.4.1 and Fig.4.2). There are two, suggested, main differences between the *Zfp644*^{Δ8} and *Zfp644*^{-/-} models. The truncated form is longer and maintains five zinc finger motifs (none in *Zfp644*^{-/-} model) and G9a binding that is not preserved in functional ablation model. It must be stressed that the described differences are still a prediction. We did confirm the sequence of *Zfp644* in our mouse models by sequencing, and based on our prediction in available literature however not in an experimental way.

Moreover, a working antibody for Zfp644 is not available, making the experimental set up even more challenging. The troubleshooting will be discussed in further sections of the chapter.

As the Laboratory of Transgenic Models of Disease of IMG remains in close co-operation with Czech Center for Phenogenomics, all described Zfp644 transgenic models went through the phenotyping pipeline described in chapter 4.3 and illustrated by Figure 4.4. Based on the results of the phenotyping and the observed severe decrease in weight in *Zfp644*⁴⁸ animals, the possibility of a metabolic phenotype was examined. Based on unbiased data (RNAseq of uterus) we decided for examination of the leptin receptor. The data seemed even more promising, as a similar effect of upregulation of the leptin receptor in a mouse organism was described before by Lou and colleagues¹³⁴. However no significant differences in *Zfp644*⁴⁸ animals were found in any of the examined parameters (leptin level in plasma, leptin receptor expression on a genetic and protein level), when compared with wild type or *Zfp644*^{-/-} animals. Next, the profound analysis of metabolism were performed on a large group of animals and repeated at five time points. The analysis of the body composition of *Zfp644*⁴⁸ animals, that were part of the experiment, revealed striking differences in fat content in *Zfp644*⁴⁸ animals. However, the analysis of metabolic rate did not show any significant difference in *Zfp644*⁴⁸ animals. We conclude that the weight decrease observed in *Zfp644*⁴⁸ animals is not caused by higher metabolic rate nor the leptin receptor upregulation in the animals.

Further analysis of biological systems in *Zfp644* transgenic animals revealed the subfertility in *Zfp644*⁴⁸ females. During the vision study, we noticed that *Zfp644*^{S673G} mice have a stronger phenotype manifestation in males. The mechanism of this phenomenon is not easy to explain but we hypothesized, that it could suggest a potential role of steroid hormones signaling in regulation of ZNF644, although published human case reports suggested no gender specificity

in any of the mutation variants of ZNF644^{6, 7, 8, 9}. Nevertheless, the tight connection to female sex hormones in mice is supported by work of Davis et al.¹⁴³, in which upregulated *Zfp644* expression was observed in 8 week-old ovariectomized mice, following treatment with estradiol, a steroidal sex hormone. Moreover, G9a protein and H3K9 methylation are tightly connected to fertility and hormonal balance as well¹¹¹. Therefore, the cross talk between *Zfp644* and sex specific hormone homeostasis is the major interest of the following study on female fertility in the *Zfp644* transgenic mice. The study included a comparison between *Zfp644*^{Δ8}, *Zfp644*^{-/-} and control animals.

We performed a breeding performance analysis in *Zfp644* transgenic mouse models, and revealed that *Zfp644*^{Δ8} homozygous females are subfertile. We conducted profound analysis of the female reproductive system in mice, and found no organs malformations in any of the examined mouse models. However, the performed analysis of female's sex hormones revealed a significant difference between the genotypes and estrus cycle phases only in *Zfp644*^{Δ8} females, but not in *Zfp644*^{-/-} or in control animals. Moreover, we were not able to observe the peak of prolactin, visible in *Zfp644*^{-/-} and control females, during estrus cycle examinations in *Zfp644*^{Δ8} females. Based on the presented data, we suggested that the observed dysregulation of sex specific hormones results in an arrest of growth of mammary gland during pregnancy. Indeed, we observed loss of size and structure in mammary glands at 18 days after fertilization. Finally, we proposed two rescue experiments: 1) the transplantation of ovaries and 2) a hormonal replacement therapy. Both were successful, providing even stronger evidence supporting the hypothesis, that female specific sex hormones are the cause of the observed phenotype. Interestingly, analysis of publicly available ChipSeq data¹ seems to support the hypothesis of G9a and H3K9 methylation involvement in the formation of the subfertility phenotype.

Both G9a and ZNF644 were analyzed in HEK293T cells and over 12 000 enriched peaks were identified for each protein. A majority of the peaks from both G9a and ZNF644 overlap. We were able to identify enriched peaks in prolactin (PRL), prolactin realizing peptide (PRLH) and prolactin receptor (PRLR) with both ZNF644 and G9a. However, we examined the methylation rate in adult male samples and samples from pregnant females, we did not find any differences between the genotypes. Nevertheless, we must take into consideration the possibility, that differences in methylation of a single or small number of genes might not be visible in an expression study of methylation marker. The problem is further commented in the troubleshooting chapter.

Based on presented data we decided to suggest a molecular mechanism explaining the difference between *Zfp644^{Δ8}* and *Zfp644^{-/-}* animals. As explained in previous chapters, the *Zfp644^{Δ8}* mouse model is a potentially truncated form of the protein. We hypothesize that it preserves the ability to bind to G9a and five out of eight zinc finger motifs present in full length protein. That might result in more promiscuous binding of DNA and potentially, also unspecific binding of DNA might occur. This could further result in silencing of nonspecifically bound targets. That could be one of possible explanations of the observed phenotype's presence only in *Zfp644^{Δ8}* and not in the functional ablation mouse model.

In contrast the *Zfp644^{-/-}* model is suggested to serve as a functional ablation with no possibility to bind G9a. We hypothesize that in this situation, G9a/GLP complex preserve its possibility to bind with another interacting partner taking over or substituting for Zfp644, as many other G9a/GLP partners were described. This could not be possible in case of *Zfp644^{Δ8}* because, as we hypothesize, this mutation still binds G9a simultaneously stopping the ability of other proteins to bind G9a in its presence. Schematic representation of the proposed molecular

mechanism is presented on a diagram below (Fig.6.1). Based on published data, we determine a potential Zinc Finger Protein, described to bind to the G9a/GLP complex and the Wiz protein¹⁴⁴. The candidate is another transcription factor, ZNF518B. Its presence is related to cancer^{145,146,147} however the mechanism was not fully described. Moreover, ZNF518B binds to the promotor region of multiple members of the STAT protein family (<https://www.genecards.org/cgi-bin/carddisp.pl?gene=ZNF518B&keywords=znf518b>) known as influencers of female sex hormones and important players in female reproduction and mammary gland development. We also found during the analysis of ChipSeq data [Bian, 2015] that STAT3 is a common peak for both G9a and ZNF644. Moreover analysis showed PIAS3, the inhibitor of STAT3, as a protein related to G9a. All data taken together might support suggested molecular mechanism, however further experiments are necessary to confirm the hypothesis.

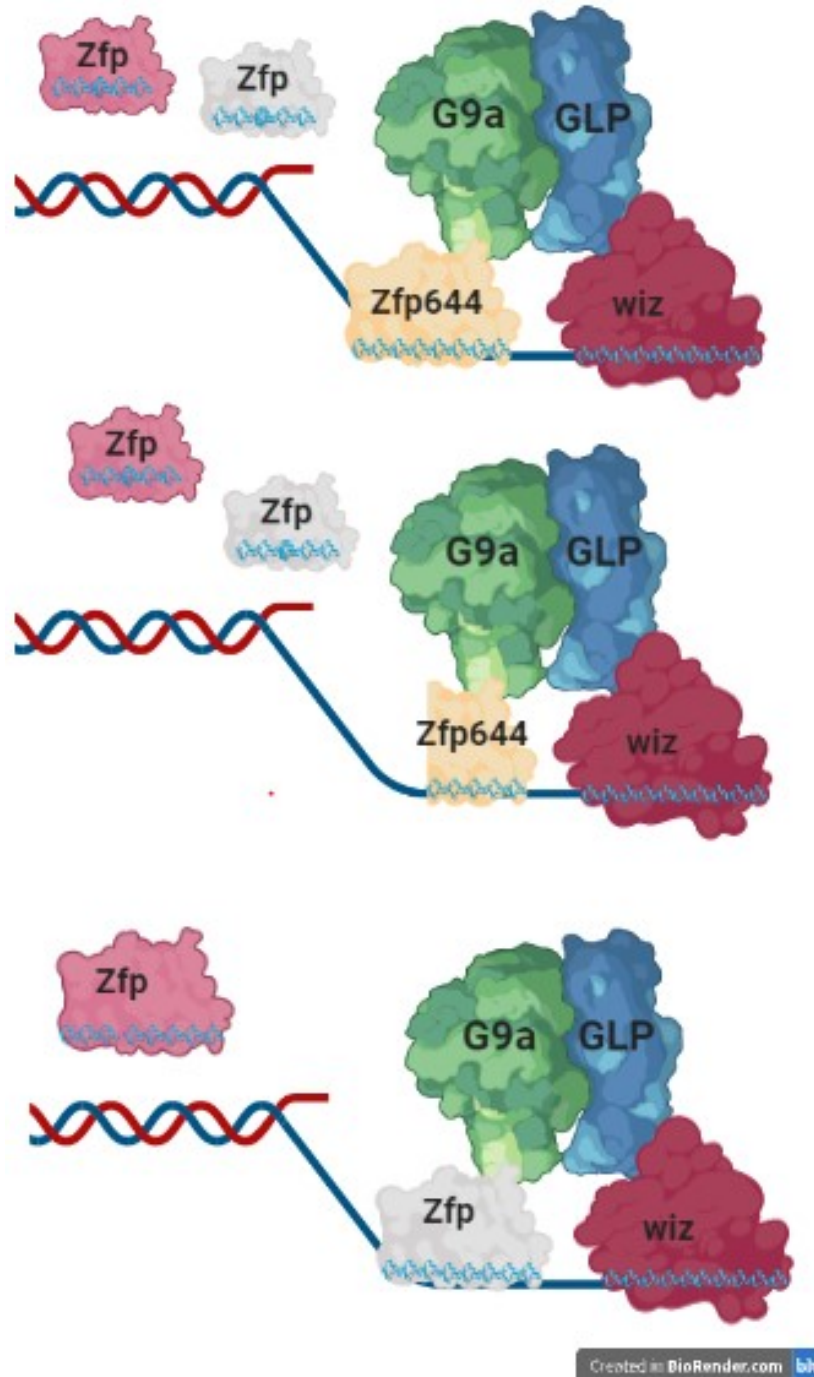


Figure 6.1. Illustration of potential molecular mechanism in *Zfp644* transgenic mouse models. The top panel shows a physiological situation where full length *Zfp644* protein is present, working in the complex and binding to DNA. Other zinc finger proteins are also present in the close proximity to the complex. The middle panel shows the hypothetical situation that might occur in *Zfp644*⁴⁸ mice. When truncated form of *Zfp644* protein is present and still bound to the complex and DNA, other zinc finger proteins are present in close distance to the complex, however, not bound to it. The lower panel shows a hypothetical situation that might occur in *Zfp644*^{-/-} mice. The missing *Zfp644* is substituted by other zinc finger protein. Figure was created with BioRender tool.

5.2. The role of Wiz protein in G9a/GLP complex.

The complementary project was focused on the role of Wiz in the G9a/GLP complex. The knockout mouse model of Wiz protein and impact of the mutation on a mouse organism was described.

It was shown, that simultaneously with ZNF644, WIZ transcription factor binds to the G9a/GLP complex^{1,13}. The G9a/GLP complex independently regulates both H3K9 and DNA methylation, resulting in transcriptional silencing²⁵. It has been proposed that either WIZ or ZNF644 is sufficient for targeting the G9a/GLP complex to specific loci for H3K9 methylation¹. However, multiple other G9a-associated molecules containing zinc finger motifs have been reported, such as PRDIBF1¹⁴⁸ or ZNF217¹⁴⁹ or, mentioned above ZNF518B¹⁴⁴. This might explain why the functional ablation of Wiz is not embryonically lethal as early as G9a or GLP themselves. However, the role of WIZ seems to be more profound than the role of ZNF644 in the complex, as no lethality in *Zfp644* knockout was reported. Moreover, double knockout mice of *Wiz* and *Zfp644*⁴⁸ were analyzed for embryonic lethality and the severity was not changed, when compared to *Wiz* embryos. On the other hand, as we suggested in the previous chapter, the possibility of substituting the *Zfp644* in case of its absence by other proteins with G9a binding ability, however, no similar evidence for Wiz was found in available literature.

The performed examinations of *Wiz* knockout embryos, in order to analyze the impact of the protein on methylation, suggest that Wiz deficiency causes disruption of methylation known to be driven by the G9a/GLP methylation complex. The analysis showed lethality at E18.5. Morphological malformations in *Wiz* knockout homozygous mice were revealed. Analysis of embryos between E14.5 to E18.5 showed that the most severe malformations include a shorter snout, cleft pellets and cleft eyelids. Moreover, the histone methylation pattern

was analyzed to understand the impact of *Wiz* knockout on G9a/GLP function. Based on presented data, we could conclude that the histone methylation pattern is suppressed. We suggest that *Wiz* plays a role in G9a/GLP methylation complex, especially in craniofacial development.

5.3. Troubleshooting

The G9a/GLP machinery, seems to be one of the most described factors in epigenetic regulation. Recently described partner of the methylation complex, Zinc Finger Protein 644, is gaining interest not only as a factor in human myopia, but also in a broader view. Here we discussed the role of *Zfp644* mutations on mouse vision, metabolism and female fertility. However, the molecular mechanism was not elucidated.

We met many obstacles when conducting the research to reveal the *Zfp644* molecular mechanism. First, we were missing the mouse antibody against *Zfp644*. We made the attempt to produce our own monoclonal antibody, however it was unsuccessful. The antibody possessed very strong unspecific binding, which we were not able to downscale and therefore the antibody was not useful. Thanks to Dr. Bian, we got the anti-ZNF644 antibody that he used in his study¹. Unfortunately, we were able to only use the antibody for WB showing missing protein for *Zfp644*⁴⁸ samples (Fig. 4.2.D). Shortly after the antibody we obtained had lost specificity and we were not able to use it for further experiments. In order to be able to do any kind of pull down experiment, expression studies or binding assays we decided to create the plasmid containing, for human cell lines, ZNF644 and tag (e.g. FLAGtag or Myctag). We took several different attempts with ZNF644 tagged at the N-termini, starting from how it was described previously in ZNF644 studies, CMV promotor, through a lentiviral inducible system and ending up with transposon system. All the attempts ended with higher or smaller failure. In conclusion not enough protein expression of ZNF644 was found in any of the experiments.

Currently, we are working on tagging the C-termini (as it was described previously) however we are concerned that it might disrupt the G9a binding ability of ZNF644. The results of these experiments are not available at the moment of submitting the thesis.

While facing the overexpression issue we worked on a different solution for revealing the differences between the full length protein, truncated form and the functional ablation. As described in chapter 5.4. we tried pull downs by G9a antibody from MEFS cells derived from different *Zfp644* transgenic mouse lines. The method and experiment itself worked well, as we were able to see the G9a, GLP and Wiz proteins were all pulled down (but controls with IgG). However, the Zfp644 was not detected in any sample. Moreover, almost no zinc finger protein were visible in the obtained data analysis, suggesting harsh conditions for such experiment. Even though, we got a promising upregulation of Cbx5 protein in *Zfp644*^{-/-} samples, that could suggest substitution for missing Zfp644 protein, we must be extremely careful with making conclusions based on only this experiment. We decided to proceed the samples to more sensitive method and sent them for RNA Seq analysis. At the moment, the results of the experiment are unknown. Simultaneously, we also cooperated with an external laboratory in order to create recombinant proteins of full length and truncated form of the protein. We hope that tags on N-termini would help us to perform pull-down experiments in mouse samples and put us closer to reveal the molecular mechanism behind the observed phenotype in *Zfp644* transgenic animals.

As suggested in Chapter 5.4, the total methylation rate in mouse samples do not seem to be affected. The natural next step would be performing ChipSeq experiment on the animals. Unfortunately, again the lack of antibody is a show stopper. We discussed the possibility of performing the ChipSeq using the G9a antibody, however the results would not be straight forward and would still raise further questions. We could take under consideration a situation,

where G9a is not the only partner of ZNF644, therefore the performed analysis would still not bring the answers for which we were hoping. Finally, we could also target the DNA bound by ZNF644 and check, if it is methylated, however for such analysis we would need strong, confirmed by different experiments and targets.

Nevertheless, the project is still ongoing and we look forward for solving the molecular mechanism behind the observed phenotype in *Zfp644*^{*Δ8*} animals. Hopefully, the experiments that are being performed simultaneously with the thesis writing would bring us closer to revealing the role of Zinc Finger 644 in G9a/GLP complex.

6. Summary

The presented work on Zfp644 and Wiz as two major zinc finger protein working with the G9a/GLP methylation machinery, was focused on revealing their biological function.

Aims were set as followed:

- **Clarify the role of Zfp644 in the development of myopia disease in vivo using murine models.** Based on single point mutation selected from GWAS studies, we were able to conclude, that the mutations of Zfp644 are causative of myopia phenotype in mice.
- **Reveal the physiological role and a molecular function of Zfp644 in mouse organism and explain the role of the transcription factor in female reproduction.** The physiological role of Zfp644 on a mouse organism was described. The female subfertility phenotype in *Zfp644*^{Δ8} animals was followed and described in details. Nevertheless, further experiments are necessary to reveal the molecular mechanism behind the observed phenotype.
- **The aim of a complementary project was to describe a role of Wiz in G9a/GLP complex.** The function of Wiz in mouse development was described. The impact of the protein knockout on craniofacial development as well as on methylation pattern of H3K9 in the developing mouse craniofacial area was followed and described.

Publications and author contributions

Doctoral thesis contains the following publications:

Szczerkowska KI, Petrezselyova S, Lindovsky J, Palkova M, Dvorak J, Makovicky P, Fang M, Jiang C, Chen L, Shi M, Liu X, Zhang J, Kubik-Zahorodna A, Schuster B, Beck IM, Novosadova V, Prochazka J, Sedlacek R. Myopia disease mouse models: a missense point mutation (S673G) and a protein-truncating mutation of the *Zfp644* mimic human disease phenotype. Cell Biosci. 2019 Feb 21;9:21. doi: 10.1186/s13578-019-0280-4. PMID: 30834109; PMCID: PMC6385473.

- Expression analysis of gene and protein, sequencing, analysis of thickness of the retina as well as quantification of cells in retinal layers, visualization and writing of the original manuscript and creating the figures in the articles were performed by the first author

Bukova I, Szczerkowska KI, Prochazkova M, Beck IM, Prochazka J and Sedlacek R (2021) Loss of Wiz Function Affects Methylation Pattern in Palate Development and Leads to Cleft Palate. Front. Cell Dev. Biol. 9:620692. doi: 10.3389/fcell.2021.620692

- Initiation of the project and help with revising the manuscript

.....
Assoc. Prof. Radislav Sedlacek, Ph.D

Supervisor

References

- 1 Bian, C., Chen, Q. & Yu, X. The zinc finger proteins ZNF644 and WIZ regulate the G9a/GLP complex for gene repression. *Elife* **4**, doi:10.7554/eLife.05606 (2015).
- 2 Wang, S., Sun, S., Li, Z., Zhang, R. & Xu, J. Accurate De Novo Prediction of Protein Contact Map by Ultra-Deep Learning Model. *PLoS Comput Biol* **13**, e1005324, doi:10.1371/journal.pcbi.1005324 (2017).
- 3 Wang, S., Li, W., Zhang, R., Liu, S. & Xu, J. CoinFold: a web server for protein contact prediction and contact-assisted protein folding. *Nucleic Acids Res* **44**, W361-366, doi:10.1093/nar/gkw307 (2016).
- 4 Ma, J., Wang, S., Wang, Z. & Xu, J. Protein contact prediction by integrating joint evolutionary coupling analysis and supervised learning. *Bioinformatics* **31**, 3506-3513, doi:10.1093/bioinformatics/btv472 (2015).
- 5 Jumper, J. *et al.* Highly accurate protein structure prediction with AlphaFold. *Nature* **596**, 583-589, doi:10.1038/s41586-021-03819-2 (2021).
- 6 Shi, Y. *et al.* Exome sequencing identifies ZNF644 mutations in high myopia. *PLoS Genet* **7**, e1002084, doi:10.1371/journal.pgen.1002084 (2011).
- 7 Tran-Viet, K. N. *et al.* Study of a US cohort supports the role of ZNF644 and high-grade myopia susceptibility. *Mol Vis* **18**, 937-944 (2012).
- 8 Xiang, X. *et al.* New ZNF644 mutations identified in patients with high myopia. *Mol Vis* **20**, 939-946 (2014).
- 9 Jiang, D. *et al.* Detection of mutations in LRPAP1, CTSH, LEPREL1, ZNF644, SLC39A5, and SCO2 in 298 families with early-onset high myopia by exome sequencing. *Invest Ophthalmol Vis Sci* **56**, 339-345, doi:10.1167/iovs.14-14850 (2014).
- 10 Wang, H. *et al.* Association of ZNF644, GRM6, and CTNND2 genes with high myopia in the Han Chinese population: Jiangsu Eye Study. *Eye (Lond)* **30**, 1017-1022, doi:10.1038/eye.2016.8 (2016).
- 11 Dungrawala, H. *et al.* The Replication Checkpoint Prevents Two Types of Fork Collapse without Regulating Replisome Stability. *Mol Cell* **59**, 998-1010, doi:10.1016/j.molcel.2015.07.030 (2015).
- 12 Olsen, J. B. *et al.* G9a and ZNF644 Physically Associate to Suppress Progenitor Gene Expression during Neurogenesis. *Stem Cell Reports* **7**, 454-470, doi:10.1016/j.stemcr.2016.06.012 (2016).
- 13 Ueda, J., Tachibana, M., Ikura, T. & Shinkai, Y. Zinc finger protein Wiz links G9a/GLP histone methyltransferases to the co-repressor molecule CtBP. *J Biol Chem* **281**, 20120-20128, doi:10.1074/jbc.M603087200 (2006).
- 14 Matsumoto, K. *et al.* Molecular cloning and distinct developmental expression pattern of spliced forms of a novel zinc finger gene wiz in the mouse cerebellum. *Brain Res Mol Brain Res* **61**, 179-189, doi:10.1016/s0169-328x(98)00216-2 (1998).
- 15 Simon, J. M. *et al.* A Role for Widely Interspaced Zinc Finger (WIZ) in Retention of the G9a Methyltransferase on Chromatin. *J Biol Chem* **290**, 26088-26102, doi:10.1074/jbc.M115.654459 (2015).
- 16 Daxinger, L. *et al.* An ENU mutagenesis screen identifies novel and known genes involved in epigenetic processes in the mouse. *Genome Biol* **14**, R96, doi:10.1186/gb-2013-14-9-r96 (2013).

- 17 Rea, S. *et al.* Regulation of chromatin structure by site-specific histone H3 methyltransferases. *Nature* **406**, 593-599, doi:10.1038/35020506 (2000).
- 18 Chin, H. G. *et al.* Sequence specificity and role of proximal amino acids of the histone H3 tail on catalysis of murine G9A lysine 9 histone H3 methyltransferase. *Biochemistry* **44**, 12998-13006, doi:10.1021/bi0509907 (2005).
- 19 Chin, H. G. *et al.* Automethylation of G9a and its implication in wider substrate specificity and HP1 binding. *Nucleic Acids Res* **35**, 7313-7323, doi:10.1093/nar/gkm726 (2007).
- 20 Rathert, P. *et al.* Protein lysine methyltransferase G9a acts on non-histone targets. *Nat Chem Biol* **4**, 344-346, doi:10.1038/nchembio.88 (2008).
- 21 Pless, O. *et al.* G9a-mediated lysine methylation alters the function of CCAAT/enhancer-binding protein-beta. *J Biol Chem* **283**, 26357-26363, doi:10.1074/jbc.M802132200 (2008).
- 22 Sampath, S. C. *et al.* Methylation of a histone mimic within the histone methyltransferase G9a regulates protein complex assembly. *Mol Cell* **27**, 596-608, doi:10.1016/j.molcel.2007.06.026 (2007).
- 23 Collins, R. E. *et al.* The ankyrin repeats of G9a and GLP histone methyltransferases are mono- and dimethyllysine binding modules. *Nat Struct Mol Biol* **15**, 245-250, doi:10.1038/nsmb.1384 (2008).
- 24 Collins, R. & Cheng, X. A case study in cross-talk: the histone lysine methyltransferases G9a and GLP. *Nucleic Acids Res* **38**, 3503-3511, doi:10.1093/nar/gkq081 (2010).
- 25 Tachibana, M., Matsumura, Y., Fukuda, M., Kimura, H. & Shinkai, Y. G9a/GLP complexes independently mediate H3K9 and DNA methylation to silence transcription. *EMBO J* **27**, 2681-2690, doi:10.1038/emboj.2008.192 (2008).
- 26 Tachibana, M. *et al.* Histone methyltransferases G9a and GLP form heteromeric complexes and are both crucial for methylation of euchromatin at H3-K9. *Genes Dev* **19**, 815-826, doi:10.1101/gad.1284005 (2005).
- 27 Tachibana, M. *et al.* G9a histone methyltransferase plays a dominant role in euchromatic histone H3 lysine 9 methylation and is essential for early embryogenesis. *Genes Dev* **16**, 1779-1791, doi:10.1101/gad.989402 (2002).
- 28 Nagano, T. *et al.* The Air noncoding RNA epigenetically silences transcription by targeting G9a to chromatin. *Science* **322**, 1717-1720, doi:10.1126/science.1163802 (2008).
- 29 Wagschal, A. *et al.* G9a histone methyltransferase contributes to imprinting in the mouse placenta. *Mol Cell Biol* **28**, 1104-1113, doi:10.1128/MCB.01111-07 (2008).
- 30 Shinkai, Y. & Tachibana, M. H3K9 methyltransferase G9a and the related molecule GLP. *Genes Dev* **25**, 781-788, doi:10.1101/gad.2027411 (2011).
- 31 Rahman, Z., Bazaz, M. R., Devabattula, G., Khan, M. A. & Godugu, C. Targeting H3K9 methyltransferase G9a and its related molecule GLP as a potential therapeutic strategy for cancer. *J Biochem Mol Toxicol* **35**, e22674, doi:10.1002/jbt.22674 (2021).
- 32 Wozniak, R. J., Klimecki, W. T., Lau, S. S., Feinstein, Y. & Futscher, B. W. 5-Aza-2'-deoxycytidine-mediated reductions in G9A histone methyltransferase and histone H3 K9 di-methylation levels are linked to tumor suppressor gene reactivation. *Oncogene* **26**, 77-90, doi:10.1038/sj.onc.1209763 (2007).
- 33 Shankar, S. R. *et al.* G9a, a multipotent regulator of gene expression. *Epigenetics* **8**, 16-22, doi:10.4161/epi.23331 (2013).

- 34 Fritsch, L. *et al.* A subset of the histone H3 lysine 9 methyltransferases Suv39h1, G9a, GLP, and SETDB1 participate in a multimeric complex. *Mol Cell* **37**, 46-56, doi:10.1016/j.molcel.2009.12.017 (2010).
- 35 Mozzetta, C. *et al.* The histone H3 lysine 9 methyltransferases G9a and GLP regulate polycomb repressive complex 2-mediated gene silencing. *Mol Cell* **53**, 277-289, doi:10.1016/j.molcel.2013.12.005 (2014).
- 36 Wu, H. *et al.* Structural biology of human H3K9 methyltransferases. *PLoS One* **5**, e8570, doi:10.1371/journal.pone.0008570 (2010).
- 37 Huang, J. *et al.* G9a and Glp methylate lysine 373 in the tumor suppressor p53. *J Biol Chem* **285**, 9636-9641, doi:10.1074/jbc.M109.062588 (2010).
- 38 Lee, J. S. *et al.* Negative regulation of stress-induced matrix metalloproteinase-9 by Sirt1 in skin tissue. *Exp Dermatol* **19**, 1060-1066, doi:10.1111/j.1600-0625.2010.01129.x (2010).
- 39 Chang, C. C., Wu, M. J., Yang, J. Y., Camarillo, I. G. & Chang, C. J. Leptin-STAT3-G9a Signaling Promotes Obesity-Mediated Breast Cancer Progression. *Cancer Res* **75**, 2375-2386, doi:10.1158/0008-5472.CAN-14-3076 (2015).
- 40 Chang, Y. F. *et al.* STAT3 induces G9a to exacerbate HER3 expression for the survival of epidermal growth factor receptor-tyrosine kinase inhibitors in lung cancers. *BMC Cancer* **19**, 959, doi:10.1186/s12885-019-6217-9 (2019).
- 41 Siouda, M. *et al.* CDYL2 Epigenetically Regulates MIR124 to Control NF-kappaB/STAT3-Dependent Breast Cancer Cell Plasticity. *iScience* **23**, 101141, doi:10.1016/j.isci.2020.101141 (2020).
- 42 Di Yorio, M. P., Bilbao, M. G., Biagini-Majorel, A. M. & Faletti, A. G. Ovarian signalling pathways regulated by leptin during the ovulatory process. *Reproduction* **146**, 647-658, doi:10.1530/REP-13-0257 (2013).
- 43 Watson, C. J. Stat transcription factors in mammary gland development and tumorigenesis. *J Mammary Gland Biol Neoplasia* **6**, 115-127, doi:10.1023/a:1009524817155 (2001).
- 44 Thorn, S. R., Giesy, S. L., Myers, M. G., Jr. & Boisclair, Y. R. Mammary ductal growth is impaired in mice lacking leptin-dependent signal transducer and activator of transcription 3 signaling. *Endocrinology* **151**, 3985-3995, doi:10.1210/en.2010-0029 (2010).
- 45 Robker, R. L. *et al.* Identification of sites of STAT3 action in the female reproductive tract through conditional gene deletion. *PLoS One* **9**, e101182, doi:10.1371/journal.pone.0101182 (2014).
- 46 Amjadi, F. *et al.* The uterine immunological changes may be responsible for repeated implantation failure. *J Reprod Immunol* **138**, 103080, doi:10.1016/j.jri.2020.103080 (2020).
- 47 Redon, C. *et al.* Histone H2A variants H2AX and H2AZ. *Curr Opin Genet Dev* **12**, 162-169, doi:10.1016/s0959-437x(02)00282-4 (2002).
- 48 Gong, F. & Miller, K. M. Histone methylation and the DNA damage response. *Mutat Res Rev Mutat Res* **780**, 37-47, doi:10.1016/j.mrrev.2017.09.003 (2019).
- 49 Murray, K. The Occurrence of Epsilon-N-Methyl Lysine in Histones. *Biochemistry* **3**, 10-15, doi:10.1021/bi00889a003 (1964).
- 50 Greer, E. L. & Shi, Y. Histone methylation: a dynamic mark in health, disease and inheritance. *Nat Rev Genet* **13**, 343-357, doi:10.1038/nrg3173 (2012).

- 51 Hawkins, R. D. *et al.* Distinct epigenomic landscapes of pluripotent and lineage-committed human cells. *Cell Stem Cell* **6**, 479-491, doi:10.1016/j.stem.2010.03.018 (2010).
- 52 Pauler, F. M. *et al.* H3K27me3 forms BLOCs over silent genes and intergenic regions and specifies a histone banding pattern on a mouse autosomal chromosome. *Genome Res* **19**, 221-233, doi:10.1101/gr.080861.108 (2009).
- 53 Wen, B., Wu, H., Shinkai, Y., Irizarry, R. A. & Feinberg, A. P. Large histone H3 lysine 9 dimethylated chromatin blocks distinguish differentiated from embryonic stem cells. *Nat Genet* **41**, 246-250, doi:10.1038/ng.297 (2009).
- 54 Black, J. C., Van Rechem, C. & Whetstine, J. R. Histone lysine methylation dynamics: establishment, regulation, and biological impact. *Mol Cell* **48**, 491-507, doi:10.1016/j.molcel.2012.11.006 (2012).
- 55 Guelen, L. *et al.* Domain organization of human chromosomes revealed by mapping of nuclear lamina interactions. *Nature* **453**, 948-951, doi:10.1038/nature06947 (2008).
- 56 Liu, T. *et al.* Broad chromosomal domains of histone modification patterns in *C. elegans*. *Genome Res* **21**, 227-236, doi:10.1101/gr.115519.110 (2011).
- 57 Lachner, M., O'Sullivan, R. J. & Jenuwein, T. An epigenetic road map for histone lysine methylation. *J Cell Sci* **116**, 2117-2124, doi:10.1242/jcs.00493 (2003).
- 58 Martin, C. & Zhang, Y. The diverse functions of histone lysine methylation. *Nat Rev Mol Cell Biol* **6**, 838-849, doi:10.1038/nrm1761 (2005).
- 59 Nakayama, J., Rice, J. C., Strahl, B. D., Allis, C. D. & Grewal, S. I. Role of histone H3 lysine 9 methylation in epigenetic control of heterochromatin assembly. *Science* **292**, 110-113, doi:10.1126/science.1060118 (2001).
- 60 Elgin, S. C. & Grewal, S. I. Heterochromatin: silence is golden. *Curr Biol* **13**, R895-898, doi:10.1016/j.cub.2003.11.006 (2003).
- 61 Kleefstra, T. *et al.* Disruption of the gene Euchromatin Histone Methyl Transferase1 (EHMTase1) is associated with the 9q34 subtelomeric deletion syndrome. *J Med Genet* **42**, 299-306, doi:10.1136/jmg.2004.028464 (2005).
- 62 Kleefstra, T. *et al.* Loss-of-function mutations in euchromatin histone methyl transferase 1 (EHMT1) cause the 9q34 subtelomeric deletion syndrome. *Am J Hum Genet* **79**, 370-377, doi:10.1086/505693 (2006).
- 63 Siderius, L. E. *et al.* X-linked mental retardation associated with cleft lip/palate maps to Xp11.3-q21.3. *Am J Med Genet* **85**, 216-220 (1999).
- 64 Laumonnier, F. *et al.* Mutations in PHF8 are associated with X linked mental retardation and cleft lip/cleft palate. *J Med Genet* **42**, 780-786, doi:10.1136/jmg.2004.029439 (2005).
- 65 Dodge, J. E., Kang, Y. K., Beppu, H., Lei, H. & Li, E. Histone H3-K9 methyltransferase ESET is essential for early development. *Mol Cell Biol* **24**, 2478-2486, doi:10.1128/MCB.24.6.2478-2486.2004 (2004).
- 66 Jambhekar, A., Dhall, A. & Shi, Y. Roles and regulation of histone methylation in animal development. *Nat Rev Mol Cell Biol* **20**, 625-641, doi:10.1038/s41580-019-0151-1 (2019).
- 67 Kuroki, S. *et al.* Epigenetic regulation of mouse sex determination by the histone demethylase Jmjd1a. *Science* **341**, 1106-1109, doi:10.1126/science.1239864 (2013).
- 68 Peters, A. H. *et al.* Loss of the Suv39h histone methyltransferases impairs mammalian heterochromatin and genome stability. *Cell* **107**, 323-337, doi:10.1016/s0092-8674(01)00542-6 (2001).

- 69 Liu, X. M. *et al.* Loss of oocyte Rps26 in mice arrests oocyte growth and causes premature ovarian failure. *Cell Death Dis* **9**, 1144, doi:10.1038/s41419-018-1196-3 (2018).
- 70 Jonard, S. & Dewailly, D. The follicular excess in polycystic ovaries, due to intra-ovarian hyperandrogenism, may be the main culprit for the follicular arrest. *Hum Reprod Update* **10**, 107-117, doi:10.1093/humupd/dmh010 (2004).
- 71 Hosseini, E. *et al.* Role of epigenetic modifications in the aberrant CYP19A1 gene expression in polycystic ovary syndrome. *Arch Med Sci* **15**, 887-895, doi:10.5114/aoms.2019.86060 (2019).
- 72 de Jong, P. Myopia: its historical contexts. *Br J Ophthalmol* **102**, 1021-1027, doi:10.1136/bjophthalmol-2017-311625 (2018).
- 73 Holden, B. A. *et al.* Global Prevalence of Myopia and High Myopia and Temporal Trends from 2000 through 2050. *Ophthalmology* **123**, 1036-1042, doi:10.1016/j.ophtha.2016.01.006 (2016).
- 74 Morgan, I. G., Ohno-Matsui, K. & Saw, S. M. Myopia. *Lancet* **379**, 1739-1748, doi:10.1016/S0140-6736(12)60272-4 (2012).
- 75 Williams, K. M. *et al.* Prevalence of refractive error in Europe: the European Eye Epidemiology (E(3)) Consortium. *Eur J Epidemiol* **30**, 305-315, doi:10.1007/s10654-015-0010-0 (2015).
- 76 Vitale, S., Sperduto, R. D. & Ferris, F. L., 3rd. Increased prevalence of myopia in the United States between 1971-1972 and 1999-2004. *Arch Ophthalmol* **127**, 1632-1639, doi:10.1001/archophthalmol.2009.303 (2009).
- 77 Lopes, M. C., Andrew, T., Carbonaro, F., Spector, T. D. & Hammond, C. J. Estimating heritability and shared environmental effects for refractive error in twin and family studies. *Invest Ophthalmol Vis Sci* **50**, 126-131, doi:10.1167/iovs.08-2385 (2009).
- 78 Young, T. L., Metlapally, R. & Shay, A. E. Complex trait genetics of refractive error. *Arch Ophthalmol* **125**, 38-48, doi:10.1001/archophth.125.1.38 (2007).
- 79 Wojciechowski, R. Nature and nurture: the complex genetics of myopia and refractive error. *Clin Genet* **79**, 301-320, doi:10.1111/j.1399-0004.2010.01592.x (2011).
- 80 Foster, P. J. & Jiang, Y. Epidemiology of myopia. *Eye (Lond)* **28**, 202-208, doi:10.1038/eye.2013.280 (2014).
- 81 Verhoeven, V. J. *et al.* Education influences the role of genetics in myopia. *Eur J Epidemiol* **28**, 973-980, doi:10.1007/s10654-013-9856-1 (2013).
- 82 Saw, S. M., Gazzard, G., Shih-Yen, E. C. & Chua, W. H. Myopia and associated pathological complications. *Ophthalmic Physiol Opt* **25**, 381-391, doi:10.1111/j.1475-1313.2005.00298.x (2005).
- 83 Fujimoto, M., Hangai, M., Suda, K. & Yoshimura, N. Features associated with foveal retinal detachment in myopic macular retinoschisis. *Am J Ophthalmol* **150**, 863-870, doi:10.1016/j.ajo.2010.06.023 (2010).
- 84 de Jong, P. T. V. M. Myopia: its historical contexts. *British Journal of Ophthalmology* **102**, 1021-1027, doi:10.1136/bjophthalmol-2017-311625 (2018).
- 85 Young, T. L. Dissecting the genetics of human high myopia: a molecular biologic approach. *Trans Am Ophthalmol Soc* **102**, 423-445 (2004).
- 86 Hawthorne, F. A. & Young, T. L. Genetic contributions to myopic refractive error: Insights from human studies and supporting evidence from animal models. *Exp Eye Res* **114**, 141-149, doi:10.1016/j.exer.2012.12.015 (2013).

- 87 Goldschmidt, E. & Jacobsen, N. Genetic and environmental effects on myopia development and progression. *Eye (Lond)* **28**, 126-133, doi:10.1038/eye.2013.254 (2014).
- 88 Verhoeven, V. J. *et al.* Visual consequences of refractive errors in the general population. *Ophthalmology* **122**, 101-109, doi:10.1016/j.ophtha.2014.07.030 (2015).
- 89 Fan, Q. *et al.* Genetic variants on chromosome 1q41 influence ocular axial length and high myopia. *PLoS Genet* **8**, e1002753, doi:10.1371/journal.pgen.1002753 (2012).
- 90 Li, J. & Zhang, Q. Insight into the molecular genetics of myopia. *Mol Vis* **23**, 1048-1080 (2017).
- 91 Zhang, D. W., Zhang, S. & Wu, J. Expression profile analysis to predict potential biomarkers for glaucoma: BMP1, DMD and GEM. *PeerJ* **8**, e9462, doi:10.7717/peerj.9462 (2020).
- 92 Lam, C. Y. *et al.* A genome-wide scan maps a novel high myopia locus to 5p15. *Invest Ophthalmol Vis Sci* **49**, 3768-3778, doi:10.1167/iovs.07-1126 (2008).
- 93 Hammond, C. J., Snieder, H., Gilbert, C. E. & Spector, T. D. Genes and environment in refractive error: the twin eye study. *Invest Ophthalmol Vis Sci* **42**, 1232-1236 (2001).
- 94 Lyhne, N., Sjolie, A. K., Kyvik, K. O. & Green, A. The importance of genes and environment for ocular refraction and its determiners: a population based study among 20-45 year old twins. *Br J Ophthalmol* **85**, 1470-1476, doi:10.1136/bjo.85.12.1470 (2001).
- 95 Cai, X. B., Shen, S. R., Chen, D. F., Zhang, Q. & Jin, Z. B. An overview of myopia genetics. *Exp Eye Res* **188**, 107778, doi:10.1016/j.exer.2019.107778 (2019).
- 96 Song, Y. *et al.* Enlargement of the Axial Length and Altered Ultrastructural Features of the Sclera in a Mutant Lumican Transgenic Mouse Model. *PLoS One* **11**, e0163165, doi:10.1371/journal.pone.0163165 (2016).
- 97 Pardue, M. T., McCall, M. A., LaVail, M. M., Gregg, R. G. & Peachey, N. S. A naturally occurring mouse model of X-linked congenital stationary night blindness. *Invest Ophthalmol Vis Sci* **39**, 2443-2449 (1998).
- 98 Park, H. *et al.* Retinal degeneration increases susceptibility to myopia in mice. *Mol Vis* **19**, 2068-2079 (2013).
- 99 Chakraborty, R., Lacy, K. D., Tan, C. C., Park, H. N. & Pardue, M. T. Refractive index measurement of the mouse crystalline lens using optical coherence tomography. *Exp Eye Res* **125**, 62-70, doi:10.1016/j.exer.2014.05.015 (2014).
- 100 Tkatchenko, A. V. *et al.* APLP2 Regulates Refractive Error and Myopia Development in Mice and Humans. *PLoS Genet* **11**, e1005432, doi:10.1371/journal.pgen.1005432 (2015).
- 101 Hudson, D. M. *et al.* Post-translationally abnormal collagens of prolyl 3-hydroxylase-2 null mice offer a pathobiological mechanism for the high myopia linked to human LEPREL1 mutations. *J Biol Chem* **290**, 8613-8622, doi:10.1074/jbc.M114.634915 (2015).
- 102 Navel, V., Beze, S. & Dutheil, F. COVID-19, sweat, tears... and myopia? *Clin Exp Optom* **103**, 555, doi:10.1111/cxo.13086 (2020).
- 103 McNally, S. & Stein, T. Overview of Mammary Gland Development: A Comparison of Mouse and Human. *Methods Mol Biol* **1501**, 1-17, doi:10.1007/978-1-4939-6475-8_1 (2017).
- 104 Topper, Y. J. & Freeman, C. S. Multiple hormone interactions in the developmental biology of the mammary gland. *Physiol Rev* **60**, 1049-1106, doi:10.1152/physrev.1980.60.4.1049 (1980).

- 105 Neville, M. C., McFadden, T. B. & Forsyth, I. Hormonal regulation of mammary differentiation and milk secretion. *J Mammary Gland Biol Neoplasia* **7**, 49-66, doi:10.1023/a:1015770423167 (2002).
- 106 Briskin, C. *et al.* Prolactin controls mammary gland development via direct and indirect mechanisms. *Dev Biol* **210**, 96-106, doi:10.1006/dbio.1999.9271 (1999).
- 107 Briskin, C. *et al.* A paracrine role for the epithelial progesterone receptor in mammary gland development. *Proc Natl Acad Sci U S A* **95**, 5076-5081, doi:10.1073/pnas.95.9.5076 (1998).
- 108 Humphreys, R. C., Lydon, J., O'Malley, B. W. & Rosen, J. M. Mammary gland development is mediated by both stromal and epithelial progesterone receptors. *Mol Endocrinol* **11**, 801-811, doi:10.1210/mend.11.6.9891 (1997).
- 109 Hennighausen, L. & Robinson, G. W. Think globally, act locally: the making of a mouse mammary gland. *Genes Dev* **12**, 449-455, doi:10.1101/gad.12.4.449 (1998).
- 110 Richert, M. M., Schwertfeger, K. L., Ryder, J. W. & Anderson, S. M. An atlas of mouse mammary gland development. *J Mammary Gland Biol Neoplasia* **5**, 227-241, doi:10.1023/a:1026499523505 (2000).
- 111 Zhang, X. *et al.* G9a-mediated methylation of ERalpha links the PHF20/MOF histone acetyltransferase complex to hormonal gene expression. *Nat Commun* **7**, 10810, doi:10.1038/ncomms10810 (2016).
- 112 Avgustinova, A. *et al.* Repression of endogenous retroviruses prevents antiviral immune response and is required for mammary gland development. *Cell Stem Cell*, doi:10.1016/j.stem.2021.04.030 (2021).
- 113 Lee, J. H. *et al.* Signal transducer and activator of transcription-3 (Stat3) plays a critical role in implantation via progesterone receptor in uterus. *FASEB J* **27**, 2553-2563, doi:10.1096/fj.12-225664 (2013).
- 114 Yoo, J. Y. *et al.* Protein Inhibitor of Activated STAT3 (PIAS3) Is Down-Regulated in Eutopic Endometrium of Women with Endometriosis. *Biol Reprod* **95**, 11, doi:10.1095/biolreprod.115.137158 (2016).
- 115 Zegers-Hochschild, F. *et al.* The International Glossary on Infertility and Fertility Care, 2017. *Hum Reprod* **32**, 1786-1801, doi:10.1093/humrep/dex234 (2017).
- 116 Jenkins, J. *et al.* European Classification of Infertility Taskforce (ECIT) response to Habbema *et al.*, 'Towards less confusing terminology in reproductive medicine: a proposal'. *Hum Reprod* **19**, 2687-2688, doi:10.1093/humrep/deh499 (2004).
- 117 Hull, M. G. & Cahill, D. J. Female infertility. *Endocrinol Metab Clin North Am* **27**, 851-876, doi:10.1016/s0889-8529(05)70044-x (1998).
- 118 Baird, D. T. Endocrinology of female infertility. *Br Med Bull* **35**, 193-198, doi:10.1093/oxfordjournals.bmb.a071569 (1979).
- 119 Mesen, T. B. & Young, S. L. Progesterone and the luteal phase: a requisite to reproduction. *Obstet Gynecol Clin North Am* **42**, 135-151, doi:10.1016/j.ogc.2014.10.003 (2015).
- 120 Matzuk, M. M. & Lamb, D. J. The biology of infertility: research advances and clinical challenges. *Nat Med* **14**, 1197-1213, doi:10.1038/nm.f.1895 (2008).
- 121 Liu, J. L., Wang, T. S. & Zhao, M. Genome-Wide Association Mapping for Female Infertility in Inbred Mice. *G3 (Bethesda)* **6**, 2929-2935, doi:10.1534/g3.116.031575 (2016).

- 122 Hanson, B. *et al.* Female infertility, infertility-associated diagnoses, and comorbidities: a review. *J Assist Reprod Genet* **34**, 167-177, doi:10.1007/s10815-016-0836-8 (2017).
- 123 Cermak, T. *et al.* Efficient design and assembly of custom TALEN and other TAL effector-based constructs for DNA targeting. *Nucleic Acids Res* **39**, e82, doi:10.1093/nar/gkr218 (2011).
- 124 Doyle, E. L. *et al.* TAL Effector-Nucleotide Targeter (TALE-NT) 2.0: tools for TAL effector design and target prediction. *Nucleic Acids Res* **40**, W117-122, doi:10.1093/nar/gks608 (2012).
- 125 Kasparek, P. *et al.* Efficient gene targeting of the Rosa26 locus in mouse zygotes using TALE nucleases. *FEBS Lett* **588**, 3982-3988, doi:10.1016/j.febslet.2014.09.014 (2014).
- 126 Wilkinson, D. G. & Nieto, M. A. Detection of messenger RNA by in situ hybridization to tissue sections and whole mounts. *Methods Enzymol* **225**, 361-373, doi:10.1016/0076-6879(93)25025-w (1993).
- 127 Livak, K. J. & Schmittgen, T. D. Analysis of relative gene expression data using real-time quantitative PCR and the 2(-Delta Delta C(T)) Method. *Methods* **25**, 402-408, doi:10.1006/meth.2001.1262 (2001).
- 128 Nguyen-Ngoc, K. V. *et al.* 3D culture assays of murine mammary branching morphogenesis and epithelial invasion. *Methods Mol Biol* **1189**, 135-162, doi:10.1007/978-1-4939-1164-6_10 (2015).
- 129 Zudaire, E., Gambardella, L., Kurcz, C. & Vermeren, S. A computational tool for quantitative analysis of vascular networks. *PLoS One* **6**, e27385, doi:10.1371/journal.pone.0027385 (2011).
- 130 Byers, S. L., Wiles, M. V., Dunn, S. L. & Taft, R. A. Mouse estrous cycle identification tool and images. *PLoS One* **7**, e35538, doi:10.1371/journal.pone.0035538 (2012).
- 131 Cora, M. C., Kooistra, L. & Travlos, G. Vaginal Cytology of the Laboratory Rat and Mouse: Review and Criteria for the Staging of the Estrous Cycle Using Stained Vaginal Smears. *Toxicol Pathol* **43**, 776-793, doi:10.1177/0192623315570339 (2015).
- 132 Hoff, J. "Methods of Blood Collection in the Mouse." (2000).
- 133 Mina, A. I. *et al.* CalR: A Web-Based Analysis Tool for Indirect Calorimetry Experiments. *Cell Metab* **28**, 656-666 e651, doi:10.1016/j.cmet.2018.06.019 (2018).
- 134 Lou, P. H. *et al.* Reduced body weight and increased energy expenditure in transgenic mice over-expressing soluble leptin receptor. *PLoS One* **5**, e11669, doi:10.1371/journal.pone.0011669 (2010).
- 135 John, S. W. *et al.* Essential iris atrophy, pigment dispersion, and glaucoma in DBA/2J mice. *Invest Ophthalmol Vis Sci* **39**, 951-962 (1998).
- 136 Brown, A. S., Zhang, M., Cucevic, V., Pavlin, C. J. & Foster, F. S. In vivo assessment of postnatal murine ocular development by ultrasound biomicroscopy. *Curr Eye Res* **30**, 45-51, doi:10.1080/02713680490894315 (2005).
- 137 Bentley, E., Miller, P. E. & Diehl, K. A. Use of high-resolution ultrasound as a diagnostic tool in veterinary ophthalmology. *J Am Vet Med Assoc* **223**, 1617-1622, 1599, doi:10.2460/javma.2003.223.1617 (2003).
- 138 Greco, A. *et al.* Ultrasound biomicroscopy in small animal research: applications in molecular and preclinical imaging. *J Biomed Biotechnol* **2012**, 519238, doi:10.1155/2012/519238 (2012).
- 139 Dickinson, M. E. *et al.* High-throughput discovery of novel developmental phenotypes. *Nature* **537**, 508-514, doi:10.1038/nature19356 (2016).

- 140 Pardue, M. T. *et al.* High susceptibility to experimental myopia in a mouse model with a retinal on pathway defect. *Invest Ophthalmol Vis Sci* **49**, 706-712, doi:10.1167/iovs.07-0643 (2008).
- 141 Tejedor, J. & de la Villa, P. Refractive changes induced by form deprivation in the mouse eye. *Invest Ophthalmol Vis Sci* **44**, 32-36 (2003).
- 142 Schaeffel, F., Burkhardt, E., Howland, H. C. & Williams, R. W. Measurement of refractive state and deprivation myopia in two strains of mice. *Optom Vis Sci* **81**, 99-110 (2004).
- 143 Davis, A. M., Mao, J., Naz, B., Kohl, J. A. & Rosenfeld, C. S. Comparative effects of estradiol, methyl-piperidino-pyrazole, raloxifene, and ICI 182 780 on gene expression in the murine uterus. *J Mol Endocrinol* **41**, 205-217, doi:10.1677/JME-08-0029 (2008).
- 144 Maier, V. K. *et al.* Functional Proteomic Analysis of Repressive Histone Methyltransferase Complexes Reveals ZNF518B as a G9A Regulator. *Mol Cell Proteomics* **14**, 1435-1446, doi:10.1074/mcp.M114.044586 (2015).
- 145 Gimeno-Valiente, F. *et al.* ZNF518B gene up-regulation promotes dissemination of tumour cells and is governed by epigenetic mechanisms in colorectal cancer. *Sci Rep* **9**, 9339, doi:10.1038/s41598-019-45411-9 (2019).
- 146 Gimeno-Valiente, F. *et al.* Epigenetic Mechanisms Are Involved in the Oncogenic Properties of ZNF518B in Colorectal Cancer. *Cancers (Basel)* **13**, doi:10.3390/cancers13061433 (2021).
- 147 Riffo-Campos, A. L. *et al.* In silico RNA-seq and experimental analyses reveal the differential expression and splicing of EPDR1 and ZNF518B genes in relation to KRAS mutations in colorectal cancer cells. *Oncol Rep* **36**, 3627-3634, doi:10.3892/or.2016.5210 (2016).
- 148 Gyory, I., Wu, J., Fejer, G., Seto, E. & Wright, K. L. PRDI-BF1 recruits the histone H3 methyltransferase G9a in transcriptional silencing. *Nat Immunol* **5**, 299-308, doi:10.1038/ni1046 (2004).
- 149 Banck, M. S. *et al.* The ZNF217 oncogene is a candidate organizer of repressive histone modifiers. *Epigenetics* **4**, 100-106, doi:10.4161/epi.4.2.7953 (2009).
- 150 Watson, Z. L. *et al.* Histone methyltransferases EHMT1 and EHMT2 (GLP/G9A) maintain PARP inhibitor resistance in high-grade serous ovarian carcinoma. *Clin Epigenetics* **11**, 165, doi:10.1186/s13148-019-0758-2 (2019).
- 151 Link, P. A. *et al.* Distinct roles for histone methyltransferases G9a and GLP in cancer germ-line antigen gene regulation in human cancer cells and murine embryonic stem cells. *Mol Cancer Res* **7**, 851-862, doi:10.1158/1541-7786.MCR-08-0497 (2009).
- 152 Pirouz, M., Pilarski, S. & Kessel, M. A critical function of Mad2l2 in primordial germ cell development of mice. *PLoS Genet* **9**, e1003712, doi:10.1371/journal.pgen.1003712 (2013).
- 153 Schones, D. E., Chen, X., Trac, C., Setten, R. & Paddison, P. J. G9a/GLP-dependent H3K9me2 patterning alters chromatin structure at CpG islands in hematopoietic progenitors. *Epigenetics Chromatin* **7**, 23, doi:10.1186/1756-8935-7-23 (2014).
- 154 Bukova, I. *et al.* Loss of Wiz Function Affects Methylation Pattern in Palate Development and Leads to Cleft Palate. *Front Cell Dev Biol* **9**, 620692, doi:10.3389/fcell.2021.620692 (2021).

- 155 Szczerkowska, K. I. *et al.* Myopia disease mouse models: a missense point mutation (S673G) and a protein-truncating mutation of the Zfp644 mimic human disease phenotype. *Cell Biosci* **9**, 21, doi:10.1186/s13578-019-0280-4 (2019).
- 156 Wainberg, M. *et al.* A genome-wide atlas of co-essential modules assigns function to uncharacterized genes. *Nat Genet* **53**, 638-649, doi:10.1038/s41588-021-00840-z (2021).
- 157 Takeda, K. *et al.* Targeted disruption of the mouse Stat3 gene leads to early embryonic lethality. *Proc Natl Acad Sci U S A* **94**, 3801-3804, doi:10.1073/pnas.94.8.3801 (1997).

List of Abbreviation

ZNF644	human Zinc Finger Protein 644
Zfp644	mouse Zinc Finger Protein 644
WIZ	Widely-Interspaced Zinc Finger-Containing Protein
G9a	euchromatic histone-lysine <i>N</i> -methyltransferase 2, EHMT2
GLP	euchromatic histone-lysine <i>N</i> -methyltransferase 1, EHMT1
GWAS	A genome-wide association study
IVF	<i>in vitro</i> fertilization
ART	Assisted reproductive technology
SET domain	Su(var)3-9–Enhancer of zeste–Trithorax domain
TAD domain	A topologically associating domain
HKMT	histone lysine methyltransferase
PTM	post-translational modifications
DDR	DNA damage response
HMT	histone methyltransferase
HDM	histone demethylase
CtBP	C-terminal-binding protein
HRT	Hormone replacement therapy
OCT	Optical coherence tomography
ERG	Electroretinography
USG	Ultrasonography
LOCKs	Large Organized Chromatin K modifications
CCP	Czech Center for Phenogenomics

List of Figures

List of Figures

Figure 1.1. Intrinsic disorder profile of ZNF644 protein

Figure 1.2. 3D model of full length Zfp644 protein

Figure 1.3. Mutation spectrum of ZNF644 in patients with high myopia up to now

Figure 1.4. ZNF644 and WIZ binding through TAD domains to G9a and GLP respectively

Figure 1.5. Graphical explanation of domains organization in G9a and GLP

Figure 1.6. Schematic representation of chromatin structure as well as histones and DNA available to epigenetic marks

Figure 1.7. Comparison of normal and myopic eye

Figure 1.8. Schematic explanation of female reproductive system

Figure 1.9. Vaginal smear cytology reflects underlying endocrine events

Figure 1.10. Representative comparison of lactiferous ducts morphology and hormonal profile in different stages in female mice

Figure 4.1. Graphical explanation of Zfp644 mutant models created in R. Sedlacek group

Figure 4.2. Generation of mutant mice used in the study

Figure 4.3. Expression analysis of Zfp644, Wiz, G9a and GLP

Figure 4.4. Graphical expression of phenotyping results of Zfp644 mutant mice and Wiz mouse model generated in Czech Center of Phenogenomics shows significant differences in numerous biological systems

Figure 4.5. Analysis of weight of *Zfp644* transgenic mice shows sever weight decrease in *Zfp644*⁴⁸ animals

Figure 4.6. RNAseq analysis of uterus of *Zfp644*⁴⁸ females shows upregulation of the leptin receptor

Figure 4.7. Analysis of expression of the leptin receptor and leptin level in plasma shows no differences among genotypes

Figure 4.8. Analysis of body composition parameters: lean mass, fat content and bone mass shows tendency for lower fat content in *Zfp644*⁴⁸ males

Figure 4.9. Analysis of metabolic rate in *Zfp644*^{Δ8} homozygous males shows no differences between genotypes

Figure 4.10. Schematic representation of ChipSeq data from HEK293T cells shows the leptin receptor binding in both G9a and ZNF644 analyses

Figure 4.11. Analysis of ocular parameters measurement with an ultrasound

Figure 4.12. Typical view of the fundus with the optic disc and blood vessels showed no differences among genotypes

Figure 4.13. Morphology of retina showed no differences among genotypes

Figure 4.14. Functional analysis of retina showed no differences among genotypes

Figure 4.15. Evaluations of retina cell numbers showed no significant differences among genotypes

Figure 4.16. Strong abnormalities of estrus cycle and breeding performance were found in *Zfp644*^{Δ8} females

Figure 4.17. Ovarian transplantation rescue the fertility phenotype in *Zfp644*^{Δ8} females

Figure 4.18. Analysis of hormonal levels and mammary gland in pregnant females shows significant differences in *Zfp644*^{Δ8} animals

Figure 4.19. Hormonal replacement therapy can be applied as a rescue of the fertility phenotype in *Zfp644*^{Δ8} females

Figure 4.20. H3K9 demethylation pattern in MEFS cells derived from *Zfp644* transgenic mouse models shows no differences between the genotypes

Figure 4.21. G9a protein expression and H3K9 demethylation pattern in testes samples from adult males from each of *Zfp644* transgenic mouse models shows no differences between the genotypes

Figure 4.22. H3K9 demethylation pattern in mammary glands samples from pregnant females from each of *Zfp644* transgenic mouse models shows no differences between the genotypes

Figure 4.23. Analysis of ChipSeq data from G9a, ZNF644 and ER from HEK293T cells shows many genes that are impacted by all three investigated genes: G9a, ZNF644 and estrogen receptor

Figure 4.24. Significantly expressed genes found in immunoprecipitation by G9a antibody.

Figure 4.25. *Wiz* deficiency leads to developmental defects especially in craniofacial area, growth retardation, and embryonic subviability

Figure 4.26. Expression pattern of *Wiz*, G9a and GLP on palatal sections shows an overlapping pattern of G9a/GLP expression with *Wiz*

Figure 4.27. Analysis of H3K9 methylation pattern in palatal shelves suggests the role of Wiz and G9a/GLP in palate development

Figure 6.1. Illustration of potential molecular mechanism in Zfp644 transgenic mouse models

List of Tables

Table 1. Summary of the results of ophthalmologic ultrasound measurements on WT, HET and HOM Zfp644^{S673G} eyes.


Table 2. Summary of the results of ophthalmologic ultrasound measurements on WT, HET and HOM Zfp644^{Δ8} eyes.

RESEARCH

Open Access



Myopia disease mouse models: a missense point mutation (S673G) and a protein-truncating mutation of the *Zfp644* mimic human disease phenotype

Katarzyna I. Szczerkowska¹, Silvia Petrezselyova^{1,2}, Jiri Lindovsky², Marcela Palkova², Jan Dvorak¹, Peter Makovicky², Mingyan Fang^{3,4,5}, Chongyi Jiang^{4,5}, Lingyan Chen^{4,5}, Mingming Shi^{4,5}, Xiao Liu^{4,5}, Jianguo Zhang^{4,5}, Agnieszka Kubik-Zahorodna², Bjoern Schuster², Inken M. Beck^{2,6}, Vendula Novosadova², Jan Prochazka^{1,2} and Radislav Sedlacek^{1,2*} 

Abstract

Zinc finger 644 (*Zfp644* in mouse, *ZNF644* in human) gene is a transcription factor whose mutation S672G is considered a potential genetic factor of inherited high myopia. *ZNF644* interacts with G9a/GLP complex, which functions as a H3K9 methyltransferase to silence transcription. In this study, we generated mouse models to unravel the mechanisms leading to symptoms associated with high myopia. Employing TALEN technology, two mice mutants were generated, either with the disease-carrying mutation (*Zfp644*^{S673G}) or with a truncated form of *Zfp644* (*Zfp644*^{Δ8}). Eye morphology and visual functions were analysed in both mutants, revealing a significant difference in a vitreous chamber depth and lens diameter, however the physiological function of retina was preserved as found under the high-myopia conditions. Our findings prove that *ZNF644/Zfp644* is involved in the development of high-myopia, indicating that mutations such as, *Zfp644*^{S673G} and *Zfp644*^{Δ8} are causative for changes connected with the disease. The developed models represent a valuable tool to investigate the molecular basis of myopia pathogenesis and its potential treatment.

Keywords: Myopia, Mouse model, Genetics, Zinc finger 644, Vision, Eye

Introduction

Myopia, the most common vision-related disease, is caused by a refractive error [1–3] based on elongation of the axial length of eyes, i.e. by an enlargement of vitreous and anterior chambers and by thinning of lenses but not by retinal dysfunction [1–6]. It is estimated that by the year 2020 myopia will affect 2.5 billion people [3]. The prevalence is increasing over the last few decades [7, 8]. Myopia is dependent on multiple factors such as

environmental influences, educational level, diet, or genetics [2, 4, 5, 9–12].

Recently, new genetic factors have been identified to be involved in myopia development [2, 13, 14], calling for new models mimicking the human disease. Among them, *ZNF644* was identified as a potential factor causing inherited myopia in different populations [13, 15–18]. Biological functions and the meaning of mutations found in *ZNF644* are still unclear. So far, twelve mutations have been reported in *ZNF644* to be involved in high myopia in humans, a majority of them are localised in exon three [16]. *ZNF644* is a protein that binds to G9a (euchromatic histone-lysine *N*-methyltransferase 2, EHMT2) as a part of H3K9 methylation complex together with GLP (euchromatic histone-lysine *N*-methyltransferase

*Correspondence: radislav.sedlacek@img.cas.cz

¹ Laboratory of Transgenic Models of Diseases, Institute of Molecular Genetics CAS, Prumyslova 595, Vestec, 252 50 Prague, Czech Republic
Full list of author information is available at the end of the article



© The Author(s) 2019. This article is distributed under the terms of the Creative Commons Attribution 4.0 International License (<http://creativecommons.org/licenses/by/4.0/>), which permits unrestricted use, distribution, and reproduction in any medium, provided you give appropriate credit to the original author(s) and the source, provide a link to the Creative Commons license, and indicate if changes were made. The Creative Commons Public Domain Dedication waiver (<http://creativecommons.org/publicdomain/zero/1.0/>) applies to the data made available in this article, unless otherwise stated.

1, EHMT1) [19]. It was shown that ZNF644 and WIZ, another zinc finger protein (Widely-Interspaced Zinc Finger-Containing Protein), interact with G9a and GLP complex respectively. WIZ and ZNF644 are responsible for targeting the G9a/GLP complex to specific DNA loci are also crucial for the regulation of G9a function during transcription [20]. It was also shown that ZNF644 in complex with G9a is present at Active Replication Forks. Knockdown of *ZNF644* in a cell culture results in reduced cell proliferation and higher sensitivity to replication stress as well as an increase of DNA damage in replicating cells [21]. Studies in fish showed that ZNF644 with G9a/GLP complex are responsible for histone methylation critical for gene silencing during neuronal differentiation in retinal neuron differentiation [22].

Examination of myopia in humans is established and employs methods such as optical coherence tomography (OCT), electroretinography (ERG) or ultrasonography (USG) [23–26]. However, investigation of signs of myopia in mouse models is challenging due to the size of eyes [14, 27–29]. It was shown that a 5.4–6.5 μm change in axial length corresponds to one diopter change in refractive error in the eyes of C57BL/6 mice [30]. Change in ocular axial length as small as 100 μm shows high myopia in C57BL/6 mice, thus the selected examination method must be very precise. In this work, we used ophthalmologic examinations known from human medical practice adapted for ophthalmological examinations of large animals [31, 32] and mice [33, 34].

Altogether, we developed and characterized two mouse mutant models of *Zfp644*. *Zfp644*^{S673G} that mimics the mutation S672G found in human and *Zfp644* ^{Δ 8}, which produces a truncated protein product due to a termination codon at position AA673. We experimentally demonstrated that S673G mutation in *Zfp644* is causative of a myopia phenotype and showed that large changes in *Zfp644*, such as protein truncation, causes a more severe phenotype. All these results point to the important regulatory role of ZNF644 in myopia development. Both *Zfp644* mutant models offer new genetic tools for depicting molecular regulatory pathways involved in development of myopia and may shed more light on its potential treatment.

Materials and methods

Models generation

All animal models and experiments used in this study were ethically reviewed and performed in accordance with European directive 2010/63/EU and were approved by the Czech Central Commission for Animal Welfare.

TALENs targeting exon 3 of *Zfp644* gene were designed using TAL Effector Nucleotide Targeter 2.0 (<https://tale-n.cac.cornell.edu/>) [35, 36] design tool and assembled

using Golden Gate cloning method. Left TALENs were designed with 16 RVDs (NN NN NI NG HD NI NI NN HD NG HD NI HD NI NN NG) followed by 16 nt spacer region and right TALENs with 15 RVDs (NN NG NN NN HD HD NN HD NG NG NI NG NN NI NI NI NG). Both TALEN plasmids were used for production of TALEN encoding mRNA as described previously [37].

TALENs mRNA was mixed with a synthetic oligodeoxynucleotide encoding mutated *Zfp644* sequence (5'AGG ATGCTAAACGGACATTTGGATCATCCAGCCAGAGCGGTAACCTTCAGCAAGTTCCACAAGAGACCACATAGAATACAAAAAGCCCGG 3'). Targeting constructs were microinjected into male pronuclei of zygotes from C57BL/6N mice. Two lines of transgenic animals were obtained: 1/*Zfp644*^{S673G} with desired mutation and 2/*Zfp644* ^{Δ 8} allele with the frame shift mutation leading to a STOP codon. The animals were further maintained on C57BL/6N background. For genotyping DNA extracted from tails of 3 weeks old C57BL/6N mice using the Quick Extract DNA Extraction Solution 1.0 Kit (Illumina, USA) was used as template for PCR with following primers (forward primer for *Zfp644* ^{Δ 8} 5'-ATCAAGCTCACA GTCAAGTAATTTT-3'; forward primer for *Zfp644*^{S673G} 5'-TCAGCAAGTTCCACAAGAGACC-3'; reverse primer for both alleles: 5'-TTGTTGGTCAGTGCTGCTCTTAAC-3').

Histology

The mice were euthanized by cervical dislocation. Eyes were sampled immediately, inserted into labelled histological cartridges, fixed in Davidson's solution for 24 h, put into 70% ethanol solution to process using an automated tissue processor (Leica ASP 6025, Leica Microsystems, Germany), and embedded in paraffin blocks using a Leica EG 1150H paraffin embedding station (Leica Microsystems, Germany). Sections of 3–5 μm were cut using a microtome (Leica RM2255, Leica Microsystems, Germany) on standard glass slides (Waldemar Knittel, GmbH, Germany). Eye samples were cut under the stereomicroscope view control and only medial cuts with optic nerve were selected for morphometry. Sections were stained with haematoxylin–eosin and mounted using Ventana Symphony H&E Slide Stainer (Ventana Medical Systems, Inc., USA). The second set of samples were cut and fixed on salinized slides (Thermo Scientific, USA) and used for immunohistochemical procedures.

RNA in situ hybridization

Digoxigenin-labeled RNA probes (DIG RNA labeling Kit, Roche, Germany) for In Situ Hybridization (ISH) were generated by in vitro transcription from plasmid contained fragment of murine *Zfp644*. Procedure were carried out according to standard protocol [38] on E9.5

after fixation in 4% PFA in whole-mount and 2 μ m paraffin section for E12.5 and E14.5. Solutions used: Blocking solution (Roche, Germany), DIG-antibody (Roche, Germany), FastRed (SigmaAldrich, USA), DAPI mounting media (Molecular Probes, USA). For fluorescence and bright-field imaging, Zeiss ImagerZ2 (Zeiss, Germany) was used, for whole-mount Zeiss Apotome (Zeiss, Germany) was used.

Morphometric analysis

Samples were evaluated using a light-microscopic images obtained using a Carl Zeiss Axio Scope A1 (Zeiss, Germany) and the Axio Scan Z1 slide scanner (Zeiss, Germany).

qPCR analysis

RNA was isolated and used as a template for reverse transcription into cDNA with M-MLV Reverse Transcriptase (Promega, USA). Quantitative PCR (qPCR) reactions were performed using the TATAA SYBR[®] GrandMaster[®] Mix (TATAA Biocenter Sweden) in CycloLightCycler[®] 480 Instrument II (Roche, Germany). Expression levels of the genes of interest were normalized to levels of *Hprt1* and *Ppia* and are presented as levels relative to wild type control. Primers were designed and ordered from (TATAA Biocenter), sequences are available upon request. All experiments were performed independently in triplicates on 3 different specimens ($n \geq 3$) per group.

Optical coherence tomography (OCT)

Both retinal fundi of 15 Zfp644^{S673G} and 21 Zfp644 ^{Δ 8} homozygous mice with 25 respective controls were examined. All animals were 16 weeks old. All mice were anaesthetized with 20% Zoletil–tiletamin 0.03 g/kg and zolazepam 0.03 mg/g (Virbac, France). Pupils of eyes were dilated using eye-drops Atropin-POS 0.5% (Ursapharm, Czech Republic). To prevent the corneal dehydration, the aqueous eye gel Vidisic 1 \times 10 mg (Dr. Gerhard Mann Pharma, Germany) was applied on the eyes and subsequently, PMMA contact lens (Cantor&Nissel, UK) were placed on the eyes. For the image acquisition of the retinal fundus, optical coherence tomography (OCT Spectralis[™] Plus, HRA Spectralis System Heidelberg Engineering GmbH, Heidelberg, Germany) with a 30° lens was used. Mice were placed on a platform fixed in front of the OCT camera and the eye horizontally directed toward the camera; the fundus was focused and cross-sectional images were taken. The segmentation of retinal layers, retinal thickness, optic disc position and blood vessels pattern were analyzed from the high-resolution cross-sectional images using HRA/Spectralis Calculation Data Manager. The average of retinal thickness was calculated from values measured in the medial cross-section

in the distance of 2 mm to the nasal and temporal side of fundus from the optic disc (Additional file 1: Figure S2D).

Electroretinography (ERG)

ERG was performed under general anaesthesia as described above. Animals were kept on a heating pad at 37 °C with eyes protected against drying by applying transparent eye gel (Vidisic, Bausch + Lomb, Czech Republic). All measurements were done on the right eye 10 min after application of 0.5% solution of atropin (Ursapharm, Czech Republic). Animals were adapted to darkness for 12 h (over night) prior to the experiment. When the scotopic part of the stimulation protocol terminated, the mice were exposed to white background light (25 cd/m²) at least for 2 min before start of the photopic stimulation protocol. The ERG stimulation and recording setup (RETI-port for animal, Roland Consult, Germany) allowed single-flash stimuli to be applied to the whole retina by Ganzfeld equipped with LED diodes and Xenon lamp, luminances were logarithmically distributed between 0.003 and 100 cd s/m². A golden ring (3 mm in diameter) was placed on the cornea as the active electrode, a golden wire inserted in the animal's mouth served as the reference electrode. Each stimulus was repeated 7–10 times and an averaged signal was saved. The signal was band-pass filtered between 1 and 300 Hz and digitized with 2 kHz sampling frequency. The scotopic and photopic responses were inspected offline using a custom-made script in Matlab (MathWorks), a-wave parameters were measured in the original recording whereas b-wave parameters were quantified after removal of the oscillatory potentials from the recordings by low-pass filtering with 80 Hz cut-off frequency.

Ultrasound imaging (USG)

Ophthalmologic ultrasound measurements were performed on 12–14 weeks old mice. Ultrasound imaging was acquired by a Vevo 2100 Imaging System (FUJIFILM VisualSonics, Inc., Toronto, ON, Canada) equipped with a MS-550S transducer operating at a center frequency of 44 MHz. The MS550S has axial resolution of 40 μ m at its focal depth and allows revealing both the anterior and posterior structures of the mouse eye (Fig. 3a). For ophthalmic ultrasound imaging, mice were anesthetized with 1–2.5% isoflurane in oxygen (1 L/min) and body temperature was maintained at 37 °C. Care was taken to place the subjects in similar postures to ensure similar orientation. Sterile hypoallergenic ultrasound gel without any air bubbles was applied between the eye and the transducer and subsequently eyes were imaged. The eye structures were measured by manually delineating margins using Vevo[®]LAB V1.7.0. Software. The software then calculated the corresponding length of each eye.

Western blotting

Organs were collected from adult male mice and homogenized using beads in Tissue Lyzer II (Qiagen, Germany) in NETN400 Lysis buffer (0.5% NP-40, 50 mM Tris-HCl pH 8.0, 2 mM EDTA, 400 mM NaCl, 10 mM NaF, 50 mM β -glycerophosphate) containing protease inhibitors. Protein lysates were centrifuged at 4 °C at 3000 rpm for 5 min. The supernatant was carefully removed and pellets containing large plasma membrane pieces, DNA and nucleoli were diluted with NETN0 Lysis buffer (no containing salts) to 100 mM NaCl. Protein concentration of nuclear fractions were determined by Pierce BCA Protein Assay Kit (Thermo Scientific, USA). Samples were loaded on 8% SDS-PAGE gel and transferred onto nitrocellulose membrane (GE Healthcare Life Science, Germany). Membranes were blocked for at least 1 h in 5% milk in TBS-T before incubating overnight at 4 °C with the appropriate primary antibody. Antibodies used were anti-ZNF644 and anti-GAPDH (G9545, Sigma-Aldrich, USA). The anti-ZNF644 (raised against N-terminus AA50-602) was kindly provided by Xiaochun Yu. The following day, membranes were washed with TBS-T, incubated with appropriate secondary antibody (Sigma-Aldrich, USA) at room temperature for 1 h and then washed again with TBS-T. Membranes were developed using Pierce™ ECL Western Blotting substrate (Thermo Scientific™, USA) and images captured using a ChemiDoc™ detection system (Bio-Rad).

Statistical analyses

Statistical analysis from ultrasonography examination was performed using GraphPad Prism software version 7.0 (GraphPad, USA); data was analyzed with one-way ANOVA. Data from OTC examination was performed in R software version 3.3 (R Core Team, Austria) using linear mixed model. Data from qPCR was analyzed using Genex 6.1 (MultiD, Sweden); qPCR statistic, analysis and graphs was performed in R software version 3.3 (R Core Team, > Austria).

Results

Zfp644 is expressed in developing and adult mouse eye

To investigate the expression pattern of Zfp644 in embryonic development, we performed whole-mount ISH of mouse embryos at E9.5 (early development of mouse eye) and fluorescence ISH of mouse embryos at E12.5 (ocular tissues differentiation) and E14.5 (corneal development). The embryonic eyes exhibited a strong hybridization signal (Fig. 1a, c, d). We also noticed strong expression in the brain and in a cervical part of a developing nervous system but not in proximal nor distal parts of spinal cord (Fig. 1a). This study was performed also on adult eyes, showing the signal in the retina and lens (Fig. 1e, e"). The

level of Zfp644 expression in adult eyes was quantified in samples isolated from male and female eyes by qRT-PCR, which showed very interesting gender dependent pattern with a higher expression level in male eyes (Fig. 1h).

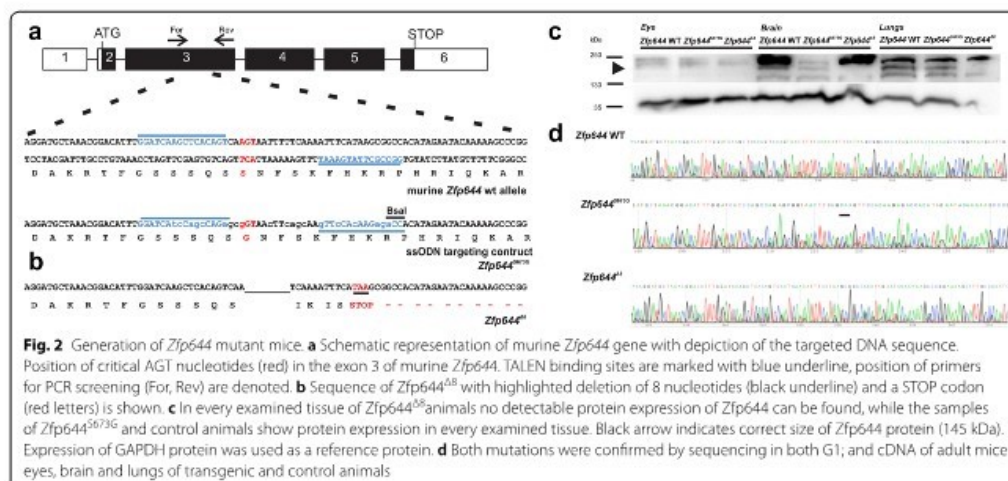
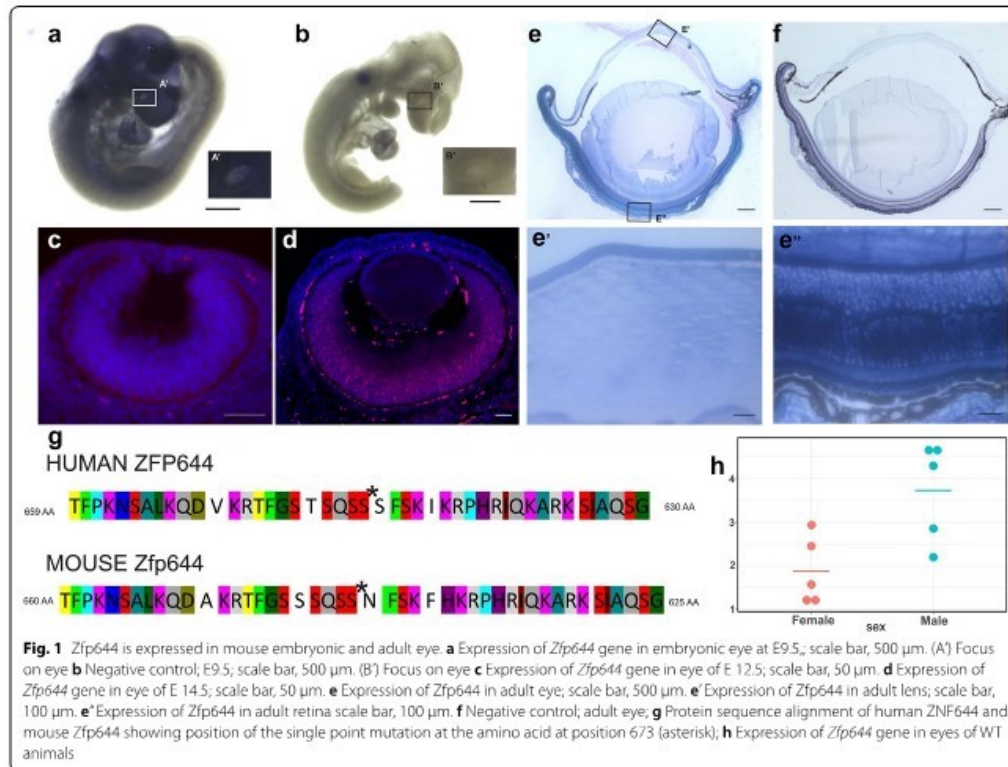
Generation of Zfp644 mutant models

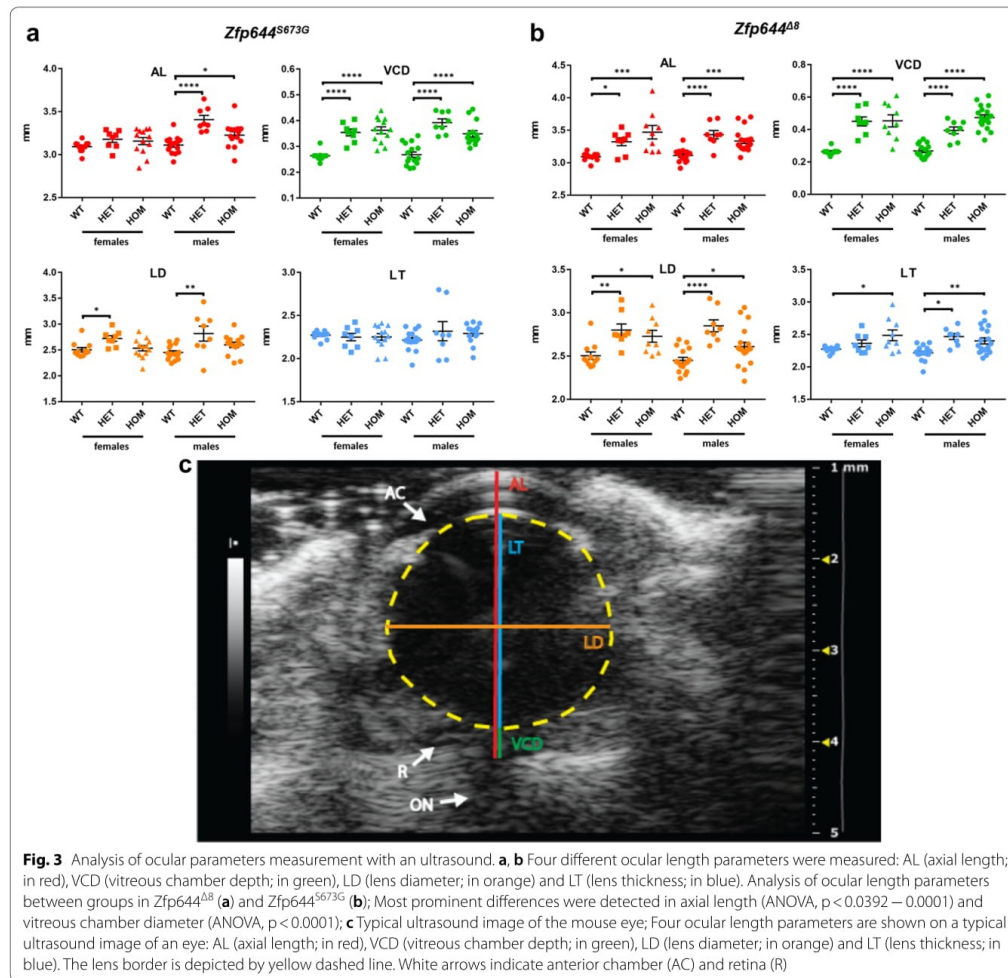
Due to a high similarity between murine and human nucleotide sequences (Fig. 1g), the first model mimics S672G mutation in *ZNF644* gene (S673G in mouse), described previously in a patient with the mutation suggested to be causative of inherited high myopia in humans (Fig. 2a). To generate the model, TALEN nucleases (TALENs) were used to specifically targeted the region in *Zfp644* gene in combination with single-stranded oligodeoxynucleotide (ssODN) carrying the desired mutation (Fig. 2a). In addition to the insertion of ssODN with the point mutation, we also obtained a mutant with deletion of eight amino acids resulting in formation of STOP codon at position AA673, which leads to a truncation of *Zfp644* (Fig. 2b). To confirm a formation of truncated form of the Zfp644 protein we performed a Western Blot analysis with anti-ZNF644 antibody (Fig. 2c). The expected size of Zfp644 protein is 145 kDa, as showed in Fig. 2c, a band this size was missing in all examined organs from Zfp644^{Δ8} animals. Both mutations were confirmed by sequencing also in G1 and cDNA of adult mice (Fig. 2d).

Mutations in Zfp644 lead to myopia caused by enlargement of the optical axis

Myopia is a vision-related disease caused by the elongation of the axial length of an eye. To investigate the impact of *Zfp644* mutations on multiple ocular parameters in vitro we employed an ultrasound imaging technique. High-frequency ultrasound imaging [39–42] was used to image posterior structures of the eye, and in particular, the retina and optical nerve was performed with the MS-550S transducer using an imaging depth of 6 to 7 mm with axial resolution of 40 μ m, thus providing a satisfied visibility for posterior eye features (Fig. 3c and Additional file 2: Figure S1). Ultrasound images of eyes with depicted ocular parameters measured in this study i.e. axial length (AL), vitreous chamber depth (VCD), lens diameter (LD) and lens thickness (LT) are shown in Fig. 3c. Ophthalmic ultrasound examinations were performed on homozygous and heterozygous Zfp644^{S673G} mice (Fig. 3a), Zfp644^{Δ8} mice (Fig. 3b), and the corresponding control (WT) mice at the age of 12–14 weeks.

In Zfp644^{S673G} animals (Fig. 3a and Additional file 3: Table S1), a significant difference in optical axis enlargement was observed only in males and, more strikingly, heterozygote constitution showed higher penetrance of a phenotype than homozygote males suggesting weak





dominant negative effect of S673G mutation with gender specific bias. Nevertheless, despite no significant difference was found in total axial length in females, a vitreous chamber depth was significantly different in both, the heterozygous and homozygous animals, without gender influence. Similar to *Zfp644*^{Δ8} animals, changes in lens diameter were most significant in heterozygous animals.

In *Zfp644*^{Δ8} animals, alteration of the axial length is caused by morphological changes in vitreous chamber depth as well as in lens thickness and diameter (Fig. 3b and Additional file 4: Table S2). Our analysis showed that every component of the optical axis is affected by the

mutation. Differences in individual ocular parameters result in enlargement of the optical axis, which results in a/the high myopia phenotype. A significant difference in all measured parameters between control and mutated mice was observed besides only one exception, the lens thickness in heterozygous females from *Zfp644*^{Δ8} mice, which showed no significant difference. However, a tendency towards a high median value in heterozygous animals was evident.

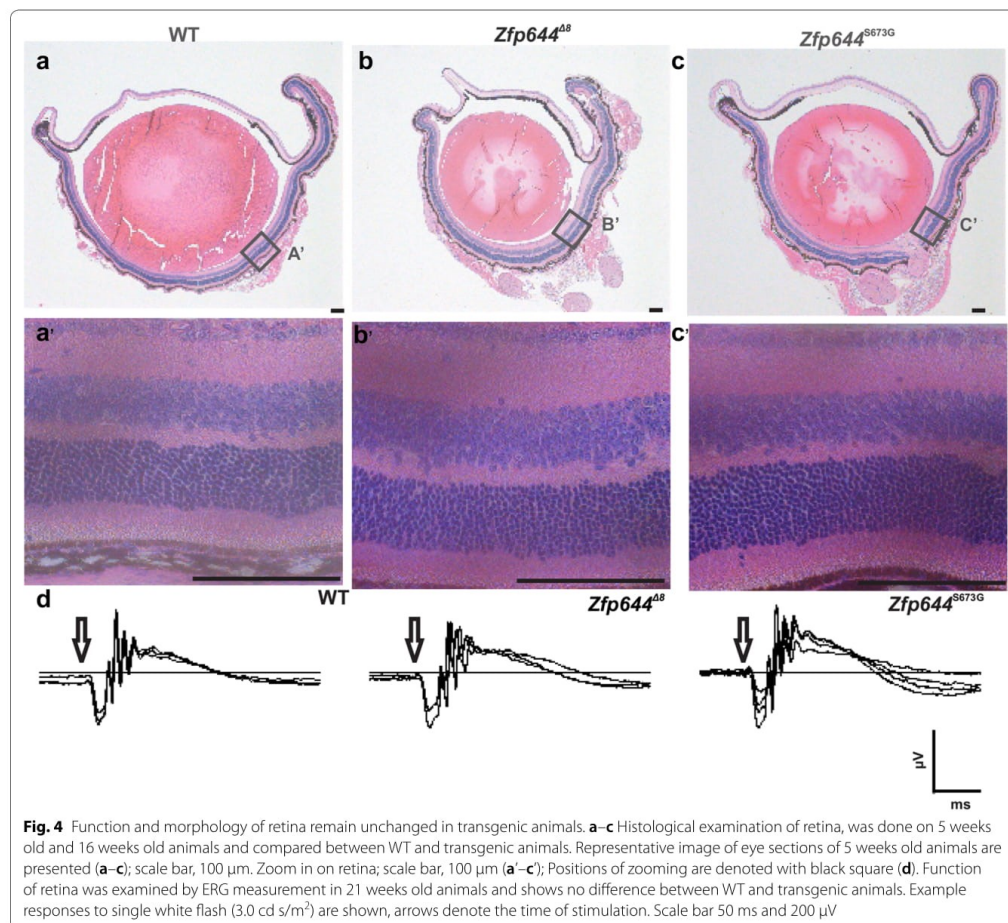
In summary the protein-truncated mutation, *Zfp644*^{Δ8}, caused a more severe phenotype than the point mutation, which is visible in both sexes and affects also

heterozygotes. In contrast, S673G is less penetrant and more pronounced in males, however mild changes leading to optical axis enlargement were observed also in females. Interestingly, in the case of S673G mutation, the eye morphology was affected more in heterozygous constitution in multiple parameters. Altogether, these results suggest dominant negative behavior of the mutated form of *Zfp644* and closely mimics the situation reported in human patients [13].

Morphology and function of the retina remains unchanged in the mutant models

As showed previously in the fish model, *ZNF644* exhibited a severe impact on retinal function and morphology

[20]. To confirm these findings, we examined morphology and function of retina in mouse *Zfp644* mutants. Both eyes of *Zfp644*^{S673G} (n=15) and *Zfp644*^{Δ8} (n=21) homozygous mutants at an age of 16 weeks were examined with OCT and compared with 25 age-matched wildtype controls. Retinal layer segmentation, optic disc position and blood vessel patterning was assessed. None of these parameters showed significant differences (Additional file 1: Figure S2A–C'). Histopathological examination of retinal structure also showed no significant difference (Fig. 4a–c'). However, in vivo imaging by OCT across the optic disc showed a significant difference in retinal thickness between control and transgenic animals (Additional file 1: Figure S2D–F). The distribution



of retinal thickness in transgenic animals showed a thinner retina than in control animals. However, examination of retinal thickness on morphology sections, of different sections of retina, did not show a significant difference, but a tendency in *Zfp644*^{Δ8} animals remain the same as difference found in OCT analysis (Additional file 1: Figure S2G). Overall, retinal thickness analysis showed a tendency to thin between control and transgenic animals. In order to provide functional validation of morphological findings we conducted electrophysiological measurements to assess the response of photoreceptors and other neurons to light stimulation by ERG. Amplitudes and implicit times of scotopic and photopic wave a (response of photoreceptors) and wave b (response of bipolar cells) respectively, were measured, however no abnormalities were found in the mutants (Fig. 4d and Additional file 5: Figure S4A–B). In addition, quantification of cell numbers in individual retina layers (ganglion cells, outer layer cells and inner layer cells) did not reveal any significant difference (Additional file 6: Figure S3A–D). These results suggest very low or no impact of *Zpf644* on the function and morphology of retina.

Discussion

Only a limited number of genetic mouse models of myopia have been generated so far. *Nob^{null}* mice, first described as a model for human night blindness [43], were found to be susceptible for a form of deprivation myopia [44–46]. Other models such as *Aplp2*-deficient mice [47], *P3h2^{u/n}* [48] or lumican transgenic mouse model [14] mimic the patient's phenotype only partially. Although, myopia can be studied in animals with disease induced during mouse life (e.g. by googles, no developmental, molecular nor genetic factor can be investigated [49, 50]).

In this study, we generated two novel mouse models *Zfp644*^{S673G} and *Zfp644*^{Δ8} that conclusively mimic human inherited high myopia. We showed that both mouse models carry signs of a myopia and the phenotype is stronger in mice with truncated *Zfp644* (*Zfp644*^{Δ8}) than in point mutation. Moreover, we also showed that measured ocular parameters are significantly different in heterozygote animals when compared to WT animals, which corresponds with genetic conditions reported previously [13, 17].

No *Zfp644*-deficient mouse model has been generated so far, and only a fish model deficient for *ZNF644* was previously described [22]. To investigate the molecular mechanism of *ZNF644*, Olsen et al. [22] prepared two different morphant models (MO) of *znf644*, based on two *znf644* isoforms (a and b) whose phenotype was severe and included changes in developing retina, midbrain, and eye size. Both *znf644a*-MO and *znf644b*-MO showed

signs of microphthalmia and disrupted midbrain morphology. Nevertheless, we could not reveal significant differences in retinal morphology, cell number in the retinal layers or in the electrophysiological responses of the retina, in any of *Zfp644* mutant mouse models.

An interesting feature of mouse *Zfp644*^{S673G} mutation is not only recapitulation of human disease but there is also stronger phenotype manifestation in males. The mechanism of this phenomenon is not easy to explain but it could be a result of a different basal level of *Zfp644* expression in male and female eyes. The candidacy of *Zfp644* in steroid hormones signaling is also supported by the work of Davis [51], in which upregulated *Zfp644* expression was observed in 8 week-old ovariectomized mice following treatment with estradiol, a steroidal sex hormone.

This could also suggest potential role of steroid hormones signaling in regulation of *ZNF644*, although published human case reports suggested no gender specificity in any of the mutation variants of *ZNF644* [13, 15–17].

Taking in account that myopia is not a retina related disease, the mouse model provides better opportunities to study the molecular role of *ZNF644* in human patients with inherited high myopia, then lower vertebrate model. Therefore, genetically modified mouse models presented in this study, are advantageous mammalian models to study genetic regulations causing inherited high myopia in humans and might serve as development base for testing of potential novel therapeutic strategies.

Additional files

Additional file 1: Figure S2. Typical view of the fundus with the optic disc and blood vessels in the WT (A), *Zfp644*^{S673G} (B) and *Zfp644*^{Δ8} (C). The white spot is a reflected light. A typical view of the retinal cross-sections thru the optic disc, respectively (A'–C'). ILM – internal limiting membrane, BM – Bruch's membrane. Scale bar; 200 μm. (D) Retinal thickness profile; position of the optic nerve is marked with a red arrow, green arrows indicate a distance in temporal and nasal retina where the retinal thickness values were collected. Retinal thickness was measured as an average of five measurements between green arrows on both temporal and nasal parts of fundus, starting from 0.5 μm from the middle of the optic disc, thru the nasal or temporal retina in 1.5 μm distance. (E) Thickness of the retina measured on morphological sections is showed in a box plot. (F) Linear distribution of the retinal thickness is showed in a plot. (G) Statistical analyses of retinal thickness distribution are showed in a box plot.

Additional file 2: Figure S1. Representative USG image of mice eyes. Both males and females eyes of every examined group are presented.

Additional file 3: Table S1. Summary of the results of ophthalmologic ultrasound measurements on WT, HET, and HOM *Zfp644*^{S673G} eyes. For each sex, medians, first and third quartile and p-values were calculated by one-way ANOVA analysis comparing WT, HET and HOM eyes.

Additional file 4: Table S2. Summary of the results of ophthalmologic ultrasound measurements on WT, HET, and HOM *Zfp644*^{Δ8} eyes. For each

sex, medians, first and third quartile and p-values were calculated by one-way ANOVA analysis comparing WT, HET and HOM eyes.

Additional file 5: Figure S4. Electroretinography. Whole-field electroretinography was recorded in animals adapted to darkness (scotopic condition) and the same animals adapted to light background (photopic condition). A) Example responses obtained in three different animals, Zfp644 WT, left column, Zfp644 S673G, middle column, and Zfp644 $\Delta 8$, right column, respectively. The time of light flash is marked with vertical dotted lines. Responses represent an averaged signal of seven to ten successive stimulations. B) Amplitude of the responses, top row, and their implicit time, bottom row, summarized for all animals and all flash luminances used. Circles represent result obtained in individual animals, lines show the mean values of each genotype, $n = 4$ (Zfp644 WT), $n = 3$ (Zfp644 S673G), $n = 5$ (Zfp644 $\Delta 8$). Neither the response of photoreceptors, as represented by the a-wave parameters, left column, nor the response of ON type of bipolar cells represented by b-wave, middle and right column, was significantly different between WT and mutated animals.

Additional file 6: Figure S3. Evaluations of retina cell numbers. Cells were counted in 200 μm . Four measurements are showed here: (A) cells in outer layer; (B) cells in inner layer; (C) ganglion cells; (D) and a total cells number. No significant differences were found.

Authors' contributions

JD, JP, and RS designed and supervise the study, and prepared manuscript. KS, SP, JL, MP, PM, AKZ, BS and IMB performed the experiments; MF was involved in experimental design and data analysis; CJ, LC, MS, XL, and JZ performed data analysis. VN performed statistics analysis. All authors read and approved the final manuscript.

Author details

¹ Laboratory of Transgenic Models of Diseases, Institute of Molecular Genetics CAS, Prumyslova 595, Vestec, 252 50 Prague, Czech Republic. ² Czech Centre for Phenogenomics, Institute of Molecular Genetics CAS, Prague, Czech Republic. ³ Division of Clinical Immunology, Department of Laboratory Medicine, Karolinska Institutet at Karolinska University Hospital Huddinge, Stockholm, Sweden. ⁴ BGI-Shenzhen, Shenzhen 518083, China. ⁵ China National GeneBank, BGI-Shenzhen, Shenzhen 518120, China. ⁶ Animal Research Center, Ulm University, Ulm, Germany.

Acknowledgements

We are grateful to Attila Juhasz, Jan Kucera, Petr Macek and members of the Transgenic and Archiving Module of CCP for excellent technical assistance and to Miles J. Raishbrook for proofreading the article.

Competing interests

The authors declare that they have no competing interests, either financial or nonfinancial, that could be perceived as prejudicing the impartiality of the research reported.

Availability of data and materials

Datasets were generated or analyzed during the current study. Data are available from the corresponding author on reasonable request.

Consent for publication

The content of the manuscript has been approved by all the authors.

Ethics approval and consent to participate

All animal models and experiments used in this study were ethically reviewed and performed in accordance with European directive 2010/63/EU and were approved by the Czech Central Commission for Animal Welfare.

Funding

The study was supported by the grant LH14276 (LH—KONTAKT II), by LM2015040 (Czech Centre for Phenogenomics), CZ.1.05/2.1.00/19.0395 ('Higher quality and capacity for transgenic models'), CZ.1.05/1.1.00/02.0109 (BIOCEV—Biotechnology and Biomedicine Centre of the Academy of Sciences and Charles University), LQ1604 (National Sustainability Program II project BIOCEV-FAR) funded by the Ministry of Education, Youth and Sports,

19-216965 by the Czech Science Foundation and the European Regional Development Fund and by RVO 68378050 by Academy of Sciences of the Czech Republic.

Publisher's Note

Springer Nature remains neutral with regard to jurisdictional claims in published maps and institutional affiliations.

Received: 18 January 2019 Accepted: 1 February 2019

Published online: 21 February 2019

References

- Lopes MC, Andrew T, Carbonaro F, Spector TD, Hammond CJ. Estimating heritability and shared environmental effects for refractive error in twin and family studies. *Invest Ophthalmol Vis Sci*. 2009;50(1):126–31.
- Young TL, Metlapally R, Shay AE. Complex trait genetics of refractive error. *Arch Ophthalmol*. 2007;125(1):38–48.
- Wojciechowski R. Nature and nurture: the complex genetics of myopia and refractive error. *Clin Genet*. 2011;79(4):301–20.
- Morgan IG, Ohno-Matsui K, Saw SM. Myopia. *Lancet*. 2012;379(9827):1739–48.
- Hawthorne FA, Young TL. Genetic contributions to myopic refractive error: insights from human studies and supporting evidence from animal models. *Exp Eye Res*. 2013;114:141–9.
- Pararajasegaram R. VISION 2020—the right to sight: from strategies to action. *Am J Ophthalmol*. 1999;128(3):359–60.
- Vitale S, Sperduto RD, Ferris FL 3rd. Increased prevalence of myopia in the United States between 1971–1972 and 1999–2004. *Arch Ophthalmol*. 2009;127(12):1632–9.
- Holden BA, Fricke TR, Wilson DA, Jong M, Naidoo KS, Sankaridurg P, et al. Global prevalence of myopia and high myopia and temporal trends from 2000 through 2050. *Ophthalmology*. 2016;123(5):1036–42.
- Young TL, Ronan SM, Drahozal LA, Wildenberg SC, Alvear AB, Oetting WS, et al. Evidence that a locus for familial high myopia maps to chromosome 18p. *Am J Hum Genet*. 1998;63(1):109–19.
- Young TL. Dissecting the genetics of human high myopia: a molecular biologic approach. *Trans Am Ophthalmol Soc*. 2004;102:423–45.
- Verhoeven VJ, Buitendijk GH, Consortium for Refractive E, Myopia, Rivadeneira F, Uitterlinden AG, et al. Education influences the role of genetics in myopia. *Eur J Epidemiol*. 2013;28(12):973–80.
- Goldschmidt E, Jacobsen N. Genetic and environmental effects on myopia development and progression. *Eye (Lond)*. 2014;28(2):126–33.
- Shi Y, Li Y, Zhang D, Zhang H, Li Y, Lu F, et al. Exome sequencing identifies ZNF644 mutations in high myopia. *PLoS Genet*. 2011;7(6):e1002084.
- Song Y, Zhang F, Zhao Y, Sun M, Tao J, Liang Y, et al. Enlargement of the axial length and altered ultrastructural features of the sclera in a mutant lumican transgenic mouse model. *PLoS ONE*. 2016;11(10):e0163165.
- Tran-Viet KN, St Germain E, Soler V, Powell C, Lim SH, Klemm T, et al. Study of a US cohort supports the role of ZNF644 and high-grade myopia susceptibility. *Mol Vis*. 2012;18:937–44.
- Xiang X, Wang T, Tong P, Li Y, Guo H, Wan A, et al. New ZNF644 mutations identified in patients with high myopia. *Mol Vis*. 2014;20:939–46.
- Jiang D, Li J, Xiao X, Li S, Jia X, Sun W, et al. Detection of mutations in LRPAP1, CTSB, LEPREL1, ZNF644, SLC39A5, and SCO2 in 298 families with early-onset high myopia by exome sequencing. *Invest Ophthalmol Vis Sci*. 2014;56(1):339–45.
- Wang H, Su S, Yang M, Hu N, Yao Y, Zhu R, et al. Association of ZNF644, GRM6, and CTNND2 genes with high myopia in the Han Chinese population: Jiangsu Eye Study. *Eye (Lond)*. 2016;30(7):1017–22.
- Simon JM, Parker JS, Liu F, Rothbart SB, Ait-Si-Ali S, Strahl BD, et al. A role for widely interspaced zinc finger (WIZ) in retention of the G9a methyltransferase on chromatin. *J Biol Chem*. 2015;290(43):26088–102.
- Bian C, Chen Q, Yu X. The zinc finger proteins ZNF644 and WIZ regulate the G9a/GLP complex for gene repression. *Elife*. 2015;4.
- Dungrawala H, Rose KL, Bhat KP, Mohini KN, Glick GG, Couch FB, et al. The replication checkpoint prevents two types of fork collapse without regulating replisome stability. *Mol Cell*. 2015;59(6):998–1010.

22. Olsen JB, Wong L, Deimling S, Miles A, Guo H, Li Y, et al. G9a and ZNF644 physically associate to suppress progenitor gene expression during neurogenesis. *Stem Cell Reports*. 2016;7(3):454–70.
23. Huang D, Swanson EA, Lin CP, Schuman JS, Stinson WG, Chang W, et al. Optical coherence tomography. *Science*. 1991;254(5035):1178–81.
24. Arrington JC, Bloom MB. Relations between the amplitudes of spontaneous saccades and visual responses. *J Opt Soc Am*. 1974;64(9):1263–71.
25. Shinar Z, Chan L, Orlinsky M. Use of ocular ultrasound for the evaluation of retinal detachment. *J Emerg Med*. 2011;40(1):53–7.
26. Dudea SM. Ultrasonography of the eye and orbit. *Med Ultrason*. 2011;13(2):171–4.
27. Pardue MT, Stone RA, Iuvone PM. Investigating mechanisms of myopia in mice. *Exp Eye Res*. 2013;114:96–105.
28. Park H, Qazi Y, Tan C, Jabbar SB, Cao Y, Schmid G, et al. Assessment of axial length measurements in mouse eyes. *Optom Vis Sci*. 2012;89(3):296–303.
29. Benavente-Perez A, Nour A, Troilo D. Axial eye growth and refractive error development can be modified by exposing the peripheral retina to relative myopic or hyperopic defocus. *Invest Ophthalmol Vis Sci*. 2014;55(10):6765–73.
30. Schmucker C, Schaeffel F. A paraxial schematic eye model for the growing C57BL/6 mouse. *Vision Res*. 2004;44(16):1857–67.
31. Hamidzadeh WA, Osuoben EP. Agreement between A-mode and B-mode ultrasonography in the measurement of ocular distances. *Vet Radiol Ultrasound*. 1999;40(5):502–7.
32. Meister U, Ohnesorge B, Korner D, Boeve MH. Evaluation of ultrasound velocity in enucleated equine aqueous humor, lens and vitreous body. *BMC Vet Res*. 2014;10:250.
33. Zhou X, Xie J, Shen M, Wang J, Jiang L, Qu J, et al. Biometric measurement of the mouse eye using optical coherence tomography with focal plane advancement. *Vision Res*. 2008;48(9):1137–43.
34. Kolesnikov AV, Kefalov VJ. Transretinal ERG recordings from mouse retina: rod and cone photoresponses. *J Vis Exp*. 2012. <https://doi.org/10.3791/3424>.
35. Cermak T, Doyle EL, Christian M, Wang L, Zhang Y, Schmidt C, et al. Efficient design and assembly of custom TALEN and other TAL effector-based constructs for DNA targeting. *Nucleic Acids Res*. 2011;39(12):e82.
36. Doyle EL, Boohar NJ, Standage DS, Voytas DF, Brendel VP, Vandyk JK, et al. TAL effector-nucleotide targeter (TALEN-NT) 2.0: tools for TAL effector design and target prediction. *Nucleic Acids Res*. 2012;40(Web Server issue):W117–22.
37. Kasperek P, Krausova M, Haneckova R, Kriz V, Zbodakova O, Korinek V, et al. Efficient gene targeting of the Rosa26 locus in mouse zygotes using TALE nucleases. *FEBS Lett*. 2014;588(21):3982–8.
38. Wilkinson DG, Nieto MA. Detection of messenger RNA by in situ hybridization to tissue sections and whole mounts. *Methods Enzymol*. 1993;225:361–73.
39. John SW, Smith RS, Savinova OV, Hawes NL, Chang B, Turnbull D, et al. Essential iris atrophy, pigment dispersion, and glaucoma in DBA/2J mice. *Invest Ophthalmol Vis Sci*. 1998;39(6):951–62.
40. Brown AS, Zhang M, Cucevic V, Pavlin CJ, Foster FS. In vivo assessment of postnatal murine ocular development by ultrasound biomicroscopy. *Curr Eye Res*. 2005;30(1):45–51.
41. Bentley E, Miller PE, Diehl KA. Use of high-resolution ultrasound as a diagnostic tool in veterinary ophthalmology. *J Am Vet Med Assoc*. 2003;223(11):1617–22, 599.
42. Greco A, Mancini M, Gargiulo S, Gramanzini M, Claudio PP, Brunetti A, et al. Ultrasound biomicroscopy in small animal research: applications in molecular and preclinical imaging. *J Biomed Biotechnol*. 2012;2012:519238.
43. Pardue MT, McCall MA, LaVail MM, Gregg RG, Peachey NS. A naturally occurring mouse model of X-linked congenital stationary night blindness. *Invest Ophthalmol Vis Sci*. 1998;39(12):2443–9.
44. Pardue MT, Faulkner AE, Fernandes A, Yin H, Schaeffel F, Williams RW, et al. High susceptibility to experimental myopia in a mouse model with a retinal on pathway defect. *Invest Ophthalmol Vis Sci*. 2008;49(2):706–12.
45. Park H, Tan CC, Faulkner A, Jabbar SB, Schmid G, Abey J, et al. Retinal degeneration increases susceptibility to myopia in mice. *Mol Vis*. 2013;19:2068–79.
46. Chakraborty R, Lacy KD, Tan CC, Park HN, Pardue MT. Refractive index measurement of the mouse crystalline lens using optical coherence tomography. *Exp Eye Res*. 2014;125:62–70.
47. Tkatchenko AV, Tkatchenko TV, Guggenheim JA, Verhoeven VJ, Hysi PG, Wojciechowski R, et al. APLP2 regulates refractive error and myopia development in mice and humans. *PLoS Genet*. 2015;11(8):e1005432.
48. Hudson DM, Joeng KS, Werther R, Rajagopal A, Weis M, Lee BH, et al. Post-translationally abnormal collagens of prolyl 3-hydroxylase-2 null mice offer a pathobiological mechanism for the high myopia linked to human LEPREL1 mutations. *J Biol Chem*. 2015;290(13):8613–22.
49. Tejedor J, de la Villa P. Refractive changes induced by form deprivation in the mouse eye. *Invest Ophthalmol Vis Sci*. 2003;44(1):32–6.
50. Schaeffel F, Burkhardt E, Howland HC, Williams RW. Measurement of refractive state and deprivation myopia in two strains of mice. *Optom Vis Sci*. 2004;81(2):99–110.
51. Davis AM, Mao J, Naz B, Kohl JA, Rosenfeld CS. Comparative effects of estradiol, methyl-piperidino-pyrazole, raloxifene, and ICI 182 780 on gene expression in the murine uterus. *J Mol Endocrinol*. 2008;41(4):205–17.

Ready to submit your research? Choose BMC and benefit from:

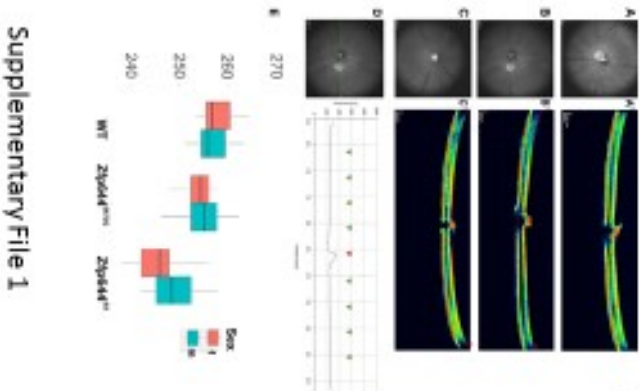
- fast, convenient online submission
- thorough peer review by experienced researchers in your field
- rapid publication on acceptance
- support for research data, including large and complex data types
- gold Open Access which fosters wider collaboration and increased citations
- maximum visibility for your research: over 100M website views per year

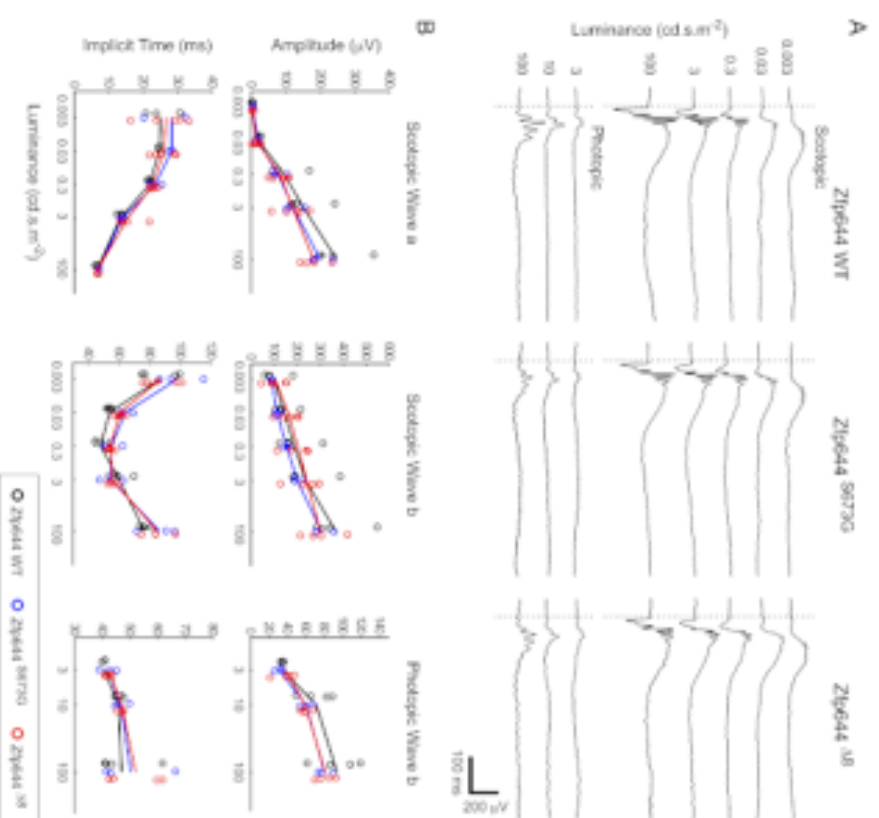
At BMC, research is always in progress.

Learn more biomedcentral.com/submissions

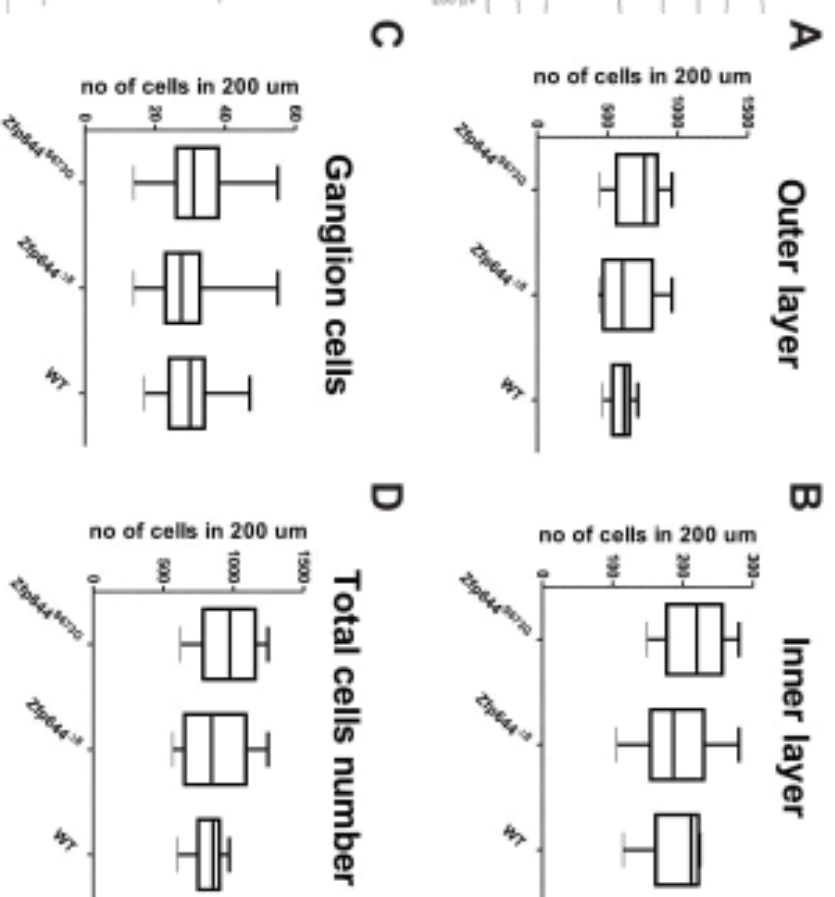


Supplementary file:





Supplementary File 3



Supplementary File 4



Loss of Wiz Function Affects Methylation Pattern in Palate Development and Leads to Cleft Palate

Ivana Bukova¹, Katarzyna Izabela Szczerkowska¹, Michaela Prochazkova¹, Inken M. Beck^{1,2}, Jan Prochazka^{1*} and Radislav Sedlacek^{1*}

¹ Laboratory of Transgenic Models of Diseases and the Czech Centre of Phenogenomics, Institute of Molecular Genetics of the Czech Academy of Sciences, Prague, Czechia, ² Animal Research Centre, Ulm University, Ulm, Germany

OPEN ACCESS

Edited by:

John Abramyan,
University of Michigan–Dearborn,
United States

Reviewed by:

Ratnam Sathiyanga Seelan,
University of Louisville, United States
Yu Lan,
Cincinnati Children's Hospital Medical
Center, United States

*Correspondence:

Jan Prochazka
jan.prochazka@img.cas.cz
Radislav Sedlacek
radislav.sedlacek@img.cas.cz

Specialty section:

This article was submitted to
Cell Growth and Division,
a section of the journal
Frontiers in Cell and Developmental
Biology

Received: 23 October 2020

Accepted: 26 April 2021

Published: 02 June 2021

Citation:

Bukova I, Szczerkowska KI,
Prochazkova M, Beck IM,
Prochazka J and Sedlacek R (2021)
Loss of Wiz Function Affects
Methylation Pattern in Palate
Development and Leads to Cleft
Palate.
Front. Cell Dev. Biol. 9:620692.
doi: 10.3389/fcell.2021.620692

WIZ (Widely Interspaced Zinc Finger) is associated with the G9a-GLP protein complex, a key H3K9 methyltransferase suggesting a role in transcriptional repression. However, its role in embryonic development is poorly described. In order to assess the loss of function of WIZ, we generated CRISPR/Cas9 WIZ knockout mouse model with 32 nucleotide deletion. Observing the lethality status, we identified the WIZ knockouts to be subviable during embryonic development and non-viable after birth. Morphology of developing embryo was analyzed at E14.5 and E18.5 and our findings were supported by microCT scans. Wiz KO showed improper development in multiple aspects, specifically in the craniofacial area. In particular, shorter snout, cleft palate, and cleft eyelids were present in mutant embryos. Palatal shelves were hypomorphic and though elevated to a horizontal position on top of the tongue, they failed to make contact and fuse. By comparison of proliferation pattern and histone methylation in developing palatal shelves we brought new evidence of importance WIZ dependent G9a-GLP methylation complex in craniofacial development, especially in palate shelf fusion.

Keywords: Wiz, G9a/GLP, histone methylation, cleft palate, development, craniofacial

INTRODUCTION

Cleft palate is one of the most common congenital defects observed at birth. Palatogenesis and secondary palate formation is a complex process that entails multiple events including growth, elevation, and fusion of palatal shelves. The palatal shelves consist mostly of neural crest cells derived mesenchyme (Ito et al., 2003). Palate formation is initiated around E11 in mice when primordia of palatal shelves emerge from the inner part of the maxillary processes. From E12, palatal shelves start growing vertically alongside the tongue, then elevate to a horizontal position above the tongue around E14. Further growth ensures that palatal shelves on both sides are able to meet and fuse (Gritli-Linde, 2007; Bush and Jiang, 2012; Kim et al., 2017).

There are multiple publications providing insight into the cellular processes underlying palatal formation and its defects. One of the various proposed mechanisms regulating palatal outgrowth appears to be coordination of epithelial-mesenchyme interactions by Shh (Lan and Jiang, 2009) and Fgf (Rice et al., 2004) signaling pathway crosstalk, by Bmp (Zhang et al., 2002) and Tgf- β signaling (Nakajima et al., 2018). The proteolysis of extracellular matrix proteins (Enomoto et al., 2010) or

epigenetic regulation such as DNA methylation (Kuriyama et al., 2008) have also been reported to contribute to palate formation.

One of the major methyltransferase mechanisms described to date represents G9a (Ehmt2- euchromatic histone lysine N-methyltransferase 2) and GLP (Ehmt1- euchromatic histone lysine N-methyltransferase 1) forming a heterodimeric complex. G9a and GLP deficiency leads to a dramatic reduction of mono- and dimethylated H3-K9 in ES cells, as well as severe growth retardation and embryonic lethality around day E9.5 (Tachibana et al., 2002, 2005). WIZ (Widely Interspaced Zinc Finger) was initially identified as a novel partner for this complex in various human and mouse cells types, including mouse ES cells. It was proposed WIZ helps with stability and specificity of this histone methylation complex (Ueda et al., 2006). Recently it was shown that WIZ and ZNF644, which both contain multiple zinc finger motifs, mediate the recruitment of the G9a/GLP histone methyltransferase complex to the specific gene loci by recognizing the DNA sequence and target H3-K9 methylation (Bian et al., 2015). The WIZ^{MommeD30} mutant model was previously prepared by ENU (N-ethyl-N-nitrosourea) mutagenesis providing insight in its function. Daxinger et al. (2013) described developmental delay and embryonic lethality of WIZ^{D30/D30} embryos between E10.5 and E12.5. WIZ has been proposed to share binding sites with transcriptional factor CTCF and to work as a transcriptional activator in neural tissue and necessary for normal behavior in mice (Isbel et al., 2016). Recently it was shown that WIZ forms a complex with CTCF and cohesin regulating DNA loop architecture and cell identity gene transcription (Justice et al., 2020).

Contrary to G9a and GLP KO (Tachibana et al., 2002, 2005), as shown in this study, functional ablation of WIZ in our case does not cause early embryonic lethality, although embryonic lethality becomes observable around E18.5, culminating in perinatal lethality of all WIZ^{-/-} individuals. Those that survive until birth exhibit cases of cleft palate and other defects in the orofacial area. WIZ is highly expressed in the developing palate, especially in the epithelial layer of palatal shelves, corresponding to expression of the G9a and GLP. We investigated the effect of WIZ deficiency on the palatogenesis process. The morphological changes of palatal shelves were accompanied by a decrease in H3-K9 methylation marks in palatal shelf epithelium, however, the general proliferation pattern in palatal shelves was not affected. We conclude that the role of WIZ is pivotal to methylation complex G9a/GLP, specifically in medial epithelium in palatal shelves where it is likely to be involved in epigenetic regulation of proper timing of palatal shelves horizontalization during palatogenesis (Figure 1A).

MATERIALS AND METHODS

Animals

WIZ knockout mouse model on a C57BL/6N background (Charles River Laboratories) used in this study was generated by targeting WIZ gene within a zinc-finger domain in exon 4 (transcript WIZ-001 ENSMUST00000087703) for frame-shift mutation by using CRISPR/Cas9 technique at Institute of

Molecular Genetics, Prague. This exon is in all transcript variants except WIZ-009 ENSMUST00000170603.2, a short variant not containing any functional domain of the protein. Selected gRNAs for microinjections had following sequences: WIZ forward 5'-TGTAATACGACTCACTATAGGCCTGCTTTGAGACACGAAAGTTTTAGAGCTAGAAATAGC-3' and WIZ reverse 5'-TGTAATACGACTCACTATAGGCCGAGATGTGAACGTGC GGTTTTAGAGCTAGAAATAGC-3'. gRNAs were introduced to the fertilized oocytes of C57BL/6N strain and transferred into pseudo pregnant foster mice. Overall 15 transfers were done, 8 pups born and analyzed using PCR, gel electrophoresis, and sequencing. In total 2 F0 mice displayed deletions in targeted sequence: animal 79874 (del 32 nt + mismatch of 4 nt) and animal 79877 (del 3 nt/del 9 nt in two alleles). Animal 79874 with 32 nucleotide deletion in exon 4 was chosen as a founder. Genotyping was performed using following primers: forward: 5'-CTTCTCTGAGCCTCAGTTTCC-3', reverse: 5'-GATGGCTTTGTTGACAGCAGG-3' with Ta 64°C. Heterozygous mice were bred in order to obtain the homozygous embryos. The day at which a vaginal plug was present was considered as day 0.5 of pregnancy (gestational/embryonic day E0.5). Female mice were sacrificed and embryos harvested at days E13.5, E14.5, E15.5, and E18.5. Yolk sacs were collected for genotyping and embryos were fixed in 4% Paraformaldehyde (PFA) for at least 24 h depending on the following procedure.

Embryo Viability

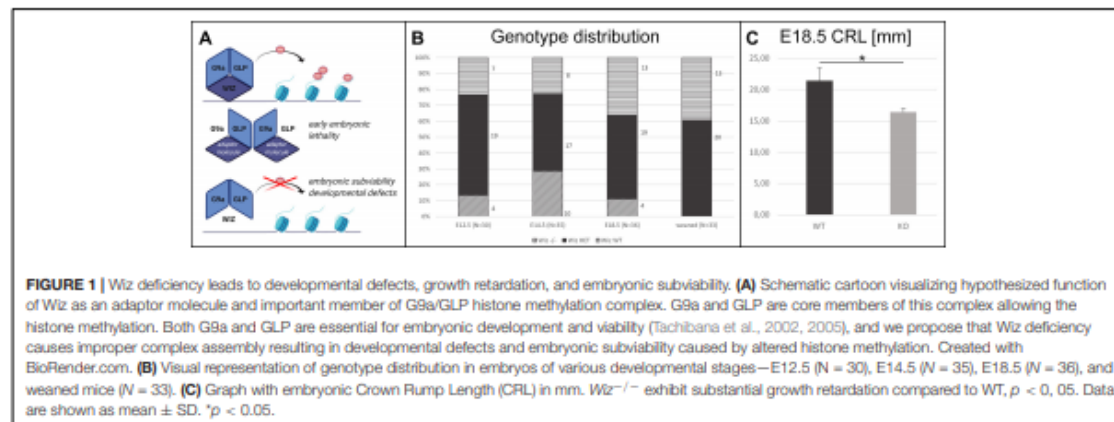
After no knockout offspring were successfully weaned from het × het crosses, embryo viability was assessed by systematic harvesting of embryos at E12.5, E14.5, and E18.5, observing them and genotyping. In total, 4 litters at E12.5 (30 embryos), 6 litters at E14.5 (35 embryos), and 6 litters at E18.5 (36 embryos) were harvested.

MicroCT—Samples Preparation and Scanning

Whole mount embryos were fixed for 7 days in 4% PFA. Samples were then processed for microCT scanning including incubation in contrast agent. Samples were stained for at least 10 days (E14.5) and 2 weeks (E18.5) with Lugol's Iodine solution. Stock solution (10 g KI and 5 g I2 in 100 ml H₂O) was diluted to a 25% working solution in H₂O to achieve neutral osmotic pressure and avoid tissue distortion. SkyScan 1272 high-resolution microCT (Bruker, Belgium) was set up for voxel size 2–3, 5 μm, and 1 mm Al filter. A 360° scan with 0.200° rotation step and three frames averaging setup was used for scanning. In total five WIZ^{-/-} and five WT embryos were scanned at E18.5 and four WIZ^{-/-} and two WT embryos at E14.5. Crown Rump Length (CRL) was measured on five WIZ^{-/-} and five WT E18.5 embryos using ImageJ software. Frontal midline section from 3D reconstruction was used for the measurement.

Histology

Whole embryos were fixed for 24 h in 4% PFA and further processed for paraffin embedding. The 10 μm thick frontal sections through the palate area were mounted on Superfrost



Plus slides. The sections were then deparaffinized in 100% Xylene and rehydrated using an alcohol range (100%–70%–30%) for immunofluorescence or *in situ* hybridization staining.

For the immunofluorescence staining, frontal paraffin sections from E13.5–E15.5 *Wiz* WT and *Wiz* KO embryos were deparaffinized, antigen retrieval was performed with HIER Citrate buffer pH6 (Zytomed) for 15 min at 110°C. Sections were washed with Phosphate-buffered saline (PBS), permeabilized in 0.1% Triton-X at room temperature, and blocked with 2, 5% ready to use Normal Goat Serum (Vector Laboratories) for 1 h. Primary antibodies were diluted in EnVision FLEX Antibody Diluent (Agilent) and applied overnight at 4°C. Primary Ab Anti-Histone H3 (mono methyl K9) antibody—ChIP Grade (Abcam, ab9045) was used at 1:250 dilution and Anti-Histone H3 (di methyl K9) antibody (mAbcam 1220)—ChIP Grade (Abcam, ab1220) at 1:250 dilution. Primary Ab *WIZ* Antibody (Novus Biologicals, NBP1-80586) was used at 1:200 dilution. Following PBS wash, secondary antibodies were applied to sections for 1 h. Donkey anti-Rabbit IgG (H + L) Highly Cross-Adsorbed Secondary Antibody, Alexa Fluor 488 (Thermo Fisher Scientific, A-21206) was used at dilution 1:1,000 as well as Goat anti-Mouse IgG (H + L) Highly Cross-Adsorbed Secondary Antibody, Alexa Fluor Plus 594 (Thermo Fisher Scientific, A32742). Sections were mounted with Dako Fluorescence Mounting Medium (Agilent) and kept in 4°C until microscopic images were taken in Axio Image Z2.

Quantification of Spectral Intensity on Immunofluorescence Sections

The spectral quantification of intensity of staining was performed in ImageJ software (version: 1.53h). The area was selected by “segmented line” tool and the spectral intensity for each channel (green, red) was quantified by “plot profile” tool. The values were processed in “R” for plot generation. Y-axis labels the arbitrary unit of signal intensity, X-axis labels the distance in medio-lateral direction in μm . *n* = 3 *Wiz*^{-/-} and three WT samples, three sections each.

In situ Hybridization

Digoxigenin-labeled RNA probes (DIG RNA labeling kit; Roche) were prepared by *in vitro* transcription from linearized pGEM[®]-T Easy (Promega, A1360) plasmids containing murine *G9a*, *GLP*, and *Wiz*. *G9a*, *GLP*, and *Wiz* sequences were obtained by PCR amplification of cDNA (murine muscle, kidney) and sub-cloned into the pGEM[®]-T Easy Vector. Sequence identity was verified by sequencing. *Wiz* containing plasmid was linearized by *Sac*II. *G9a* containing plasmid was linearized by *Sac*II and *GLP* containing plasmid by *Spe*I enzymes (Supplementary Figures 1A–C). We also generated *Wiz*, *G9a*, and *GLP* sense probes as a negative control (Supplementary Figure 1D). *In situ* hybridization was performed according to standard protocols (Wilkinson and Nieto, 1993) on frontal sections from E13.5, E14.5, and E15.5 embryos. Sections were mounted with Aquatex (Merck). We analyzed the expression pattern in forming palate and surrounding tissue.

EdU Cell Proliferation Analysis

Pregnant females with embryos dedicated for proliferation analysis were injected peritoneally with 100 μl of 6.25 mM EdU (5-ethynyl-2'-deoxyuridine) solution in PBS each 90 min before the embryo harvest. Embryos were as usual fixed for 24 h in 4% PFA and processed for paraffin embedding and sectioning. The Click-iT EdU Cell Proliferation Kit for Imaging (Thermo Fisher Scientific) was used to visualize proliferating cells. Nuclear counterstain was performed with DAPI at 1:1,000 dilution. Cell counting for quantification was performed in ImageJ software on five sections from anterior and five sections from posterior region of palatal shelves from three *Wiz*^{-/-} and three WT embryos at E13.5 and E14.5. For statistical comparison, linear mixed model was used with animal ID as a random effect.

Supplementary Methods related to SDS-PAGE and immunoblotting and Quantitative real time reverse transcription polymerase chain reaction (qRT-PCR) can be found in **Supplementary Methods**.

RESULTS

Generation of Wiz Deficient Mouse Model

Targeted deletion of 32 nucleotides in exon 4 of *Wiz* causes frame-shift mutation and premature stop codon eliminating *Wiz* protein production (Supplementary Figure 2A). Western blot analysis using Anti-*Wiz* Ab detected a *Wiz* protein sized around 130 kDa in WT sample and lower amount of *Wiz* protein in heterozygous sample. No *Wiz* protein was detected in *Wiz*^{-/-} embryonic sample (Supplementary Figure 2B). Anti-*Wiz* antibody shows high cross-reactivity. Mass spectrometry analysis of gel cutout (Supplementary Figure 2C) was performed to confirm the absence of *Wiz* protein in *Wiz*^{-/-} protein lysate (Supplementary Figure 2D).

Wiz Deficiency Causes Growth Retardation and Craniofacial Defects

No viable *Wiz*^{-/-} mice were found after weaning. Moreover, no knockout pups were observed during the period before weaning. This finding strongly suggested that there is a late embryonic/perinatal lethal phenotype in *Wiz*^{-/-} mice. We proceeded with a standardized search (Dickinson et al., 2016) for the embryonic lethal period, showing that genotype distribution was variable but relatively normal at all developmental stages until E18.5, even though we observed dead *Wiz*^{-/-} embryos already from stage E12.5. After the birth, we were not able to recognize any viable *Wiz*^{-/-} newborns, suggesting that *Wiz*^{-/-} were subviable at E18.5 and show complete perinatal lethality (Figure 1B). This development corresponds to strong growth retardation at E18.5, which results in almost 25% lower CRL before birth compared to WT embryos (Figure 1C).

Besides the obvious growth retardation at E18.5 we observed improper development at multiple sites, especially in the craniofacial area as early as embryonic stage E14.5. At this stage, the horizontalization was delayed in *Wiz*^{-/-} palatal shelves which remained lateral to the tongue (Figure 2A). Horizontalization of shelves was never observed even at E15.5 (five embryos out of five *Wiz*^{-/-} embryos), when all WT palates were already fused. At E18.5 the craniofacial defect became even more visible with shorter snout morphology and also underdevelopment of eyelids. From the 12 *Wiz*^{-/-} embryos harvested at E18.5 approximately 60% (7) showed full cleft palate and 40% (5) showed incomplete palatal shelves fusion. Palatal morphology at this stage implies that the shelves were later able to proceed to horizontalization; however, the delay of this process resulted in cleft phenotype (Figure 2B).

WIZ Is Expressed in Palatal Shelves and Overlaps With G9a/GLP in Developing Palate Epithelium

In order to investigate whether *Wiz* protein has a direct role in palatogenesis, we proceeded with fluorescent immunostaining of *Wiz* protein and *in situ* hybridization on histological sections of developing palate at E13.5 and E14.5. The nuclear localization of

Wiz was indeed detected in palatal shelves, both in neural crest derived mesenchyme and in palatal shelf epithelium. Staining was stronger at the epithelial layer on the lateral side, which later forms the roof of oral cavity (Figure 3A, arrows). We also analyzed the expression of *G9a* and *GLP* to provide evidence that *Wiz* manifests its function during palate development via a possible interaction with the *G9a* and *GLP* methylation complex. Both *G9a* and *GLP* showed an overlapping expression pattern with *Wiz* and an increased expression at the oral side of palatal shelves (Figures 3B,C).

Wiz Deficiency Does Not Affect Cell Proliferation but Suppresses Methylation Pattern in Developing Palate While Involved Signaling Pathways Are Unaffected

In connection to observed failure of horizontalization and fusion of palatal shelves at E15.5, we asked whether the phenotype might be caused by a reduction in proliferative capacity of cells in the developing palate at earlier stages (E13.5 and E14.5). After a short EdU pulse (90 min) to visualize S phase proliferative cells, we examined the proliferation pattern in the palatal shelves. We could not observe a notable difference in number of EdU positive cells between WT and *Wiz*^{-/-} embryos on histological sections at E13.5 (Figure 4A) and at E14.5 (Supplementary Figure 3A). There was no significant difference in ratio of proliferating to all cells in anterior and posterior regions in palatal shelves at E13.5 (Figure 4B) as well as at E14.5 (Supplementary Figure 3B). These results suggest that the cell proliferation levels are not affected at these developmental stages.

To examine the possible disruption of signaling pathways involved in palate development, we performed a RT-qPCR analysis (Supplementary Figure 3C) of WT and *Wiz*^{-/-} whole palatal shelf tissue at E13.5. Our data show that signaling pathways such as Wnt (*Wnt5a*, *Axin1*, *Axin2*), Fgf (*Etv4*, *Etv5*, *Spry1*), Shh (*Gli*, *Shh*), Bmp (*Bmp2*, *Bmp4*), or TGF- β (*Tgfb- β*) or Notch (*Hes1*, *Notch2*) are not significantly affected by *Wiz* ablation at this stage as well as expression of other cleft palate associated genes like *Msx2* or *Cdh1*.

The presence of *G9a* and *GLP* methylation complexes in developing palate provides a strong indication that *Wiz* might be responsible for regulation of the histone methylation code. We used antibodies against monomethylated and dimethylated Histone 3 Lysine 9 (H3-K9), which is the most common target of the *G9a*/*GLP* methylation complex, and compared the methylation pattern on histological sections from between E13.5 and E15.5.

Starting from the stage E13.5 we did not observe changes in monomethylated H3-K9 in any part of developing palatal shelves. However, we already observed loci specific diminution of the methylation signal from dimethylated H3-K9 in the *Wiz*^{-/-} embryos (Figure 5A). The decrease of methylation marks was localized only in medial segment (part of developing palatal shelves) of future oral cavity epithelium in contrary to lateral segment (part of maxilla) (Figure 5A). The spectral intensity quantification supported these findings and also confirmed that

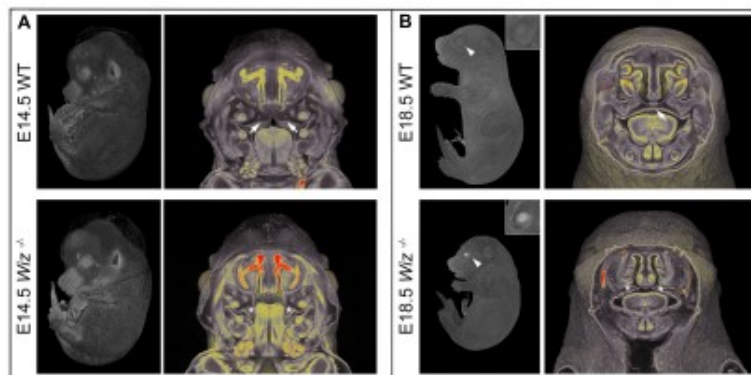


FIGURE 2 | *Wiz* deficiency causes improper development especially in craniofacial area. **(A)** MicroCT images of E14.5 embryos. White arrows point to palatal shelves of WT embryo in proper horizontal position on top of the tongue. White asterisks indicate palatal shelves of *Wiz*^{-/-} embryo remaining in vertical position along the tongue. **(B)** MicroCT images of E18.5 embryos. White arrowhead points to the eyelids, properly developed in WT and cleft in *Wiz*^{-/-} embryo. Detail of the eye is shown in the top right corner. White arrow points to fully fused and formed palate of WT embryo. White asterisks indicate severely hypomorphic palatal shelves of *Wiz* KO embryo.

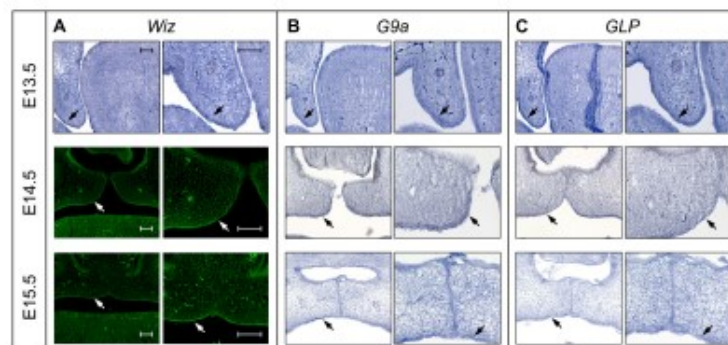


FIGURE 3 | Expression pattern of *Wiz* in epithelia of palatal shelves overlaps with *G9a/GLP*. **(A)** *In situ* hybridization on palatal sections and immunofluorescent stained palatal sections of E13.5 WT (upper panels), E14.5 (middle panels), and E15.5 (lower panels) palatal sections showing strong expression of *Wiz* in the epithelia on oral side of palatal shelves (black and white arrows). **(B,C)** *In situ* hybridization on palatal sections of E13.5 WT (upper panels), E14.5 (middle panels), and E15.5 (lower panels) showing overlapping pattern of *G9a/GLP* expression with *Wiz* (black arrows). Scale bar represents 100 μ m and applies for all images.

the methylation mark immunostaining was comparable among the samples and lateral part of shelves.

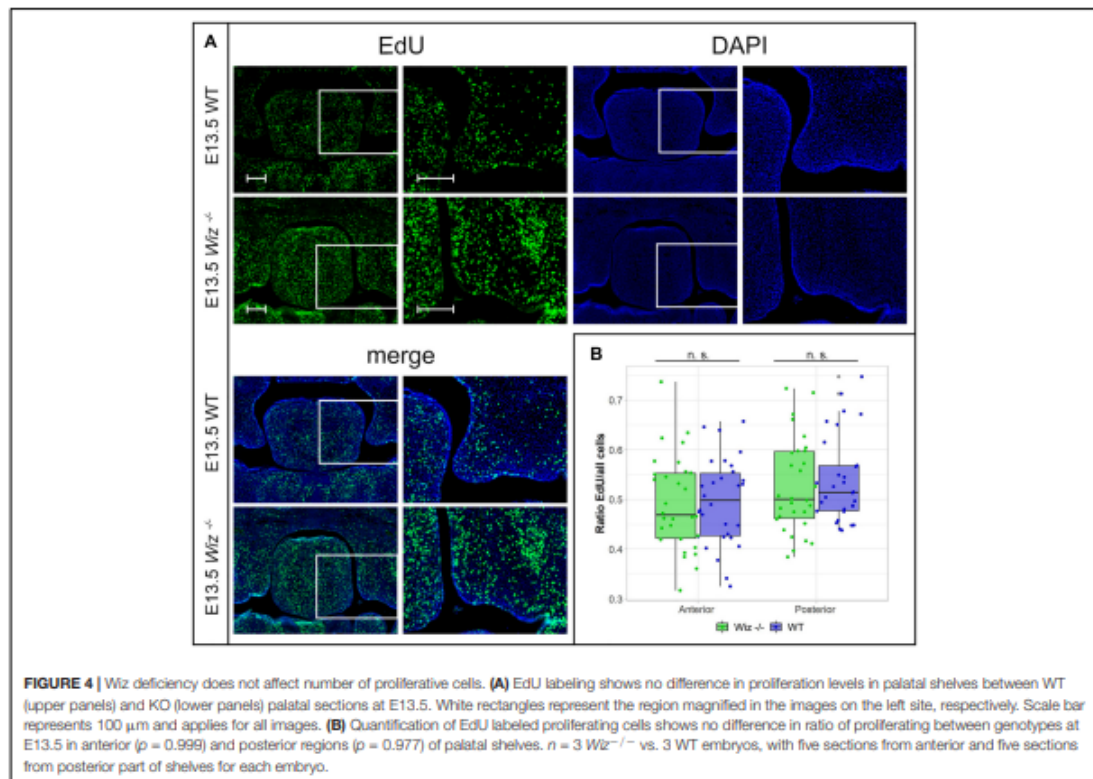
Such phenomenon is observable also during later stages of palate development at E14.5 and E15.5 (Figures 5B,C). Despite the deregulation of methylation code at this stage cannot be considered as primary cause of palatal clefting, it is worth mentioning that such spatial-temporal diminution of methylation is observable over the most critical period of palatal development.

The medial segment corresponding to lateral part of palatal shelf epithelium seems to be the most affected and is corresponding to sites of the strongest expression of *Wiz* and *G9a/GLP* (Figure 3). Our data suggest the regulatory role of *Wiz* protein in temporo-spatial regulation of chromatin methylation correlates with delayed palatal shelves horizontalization.

Nevertheless, the precise molecular mechanism of this action needs further examination, likely at single cell level and by unbiased transcriptomics.

DISCUSSION

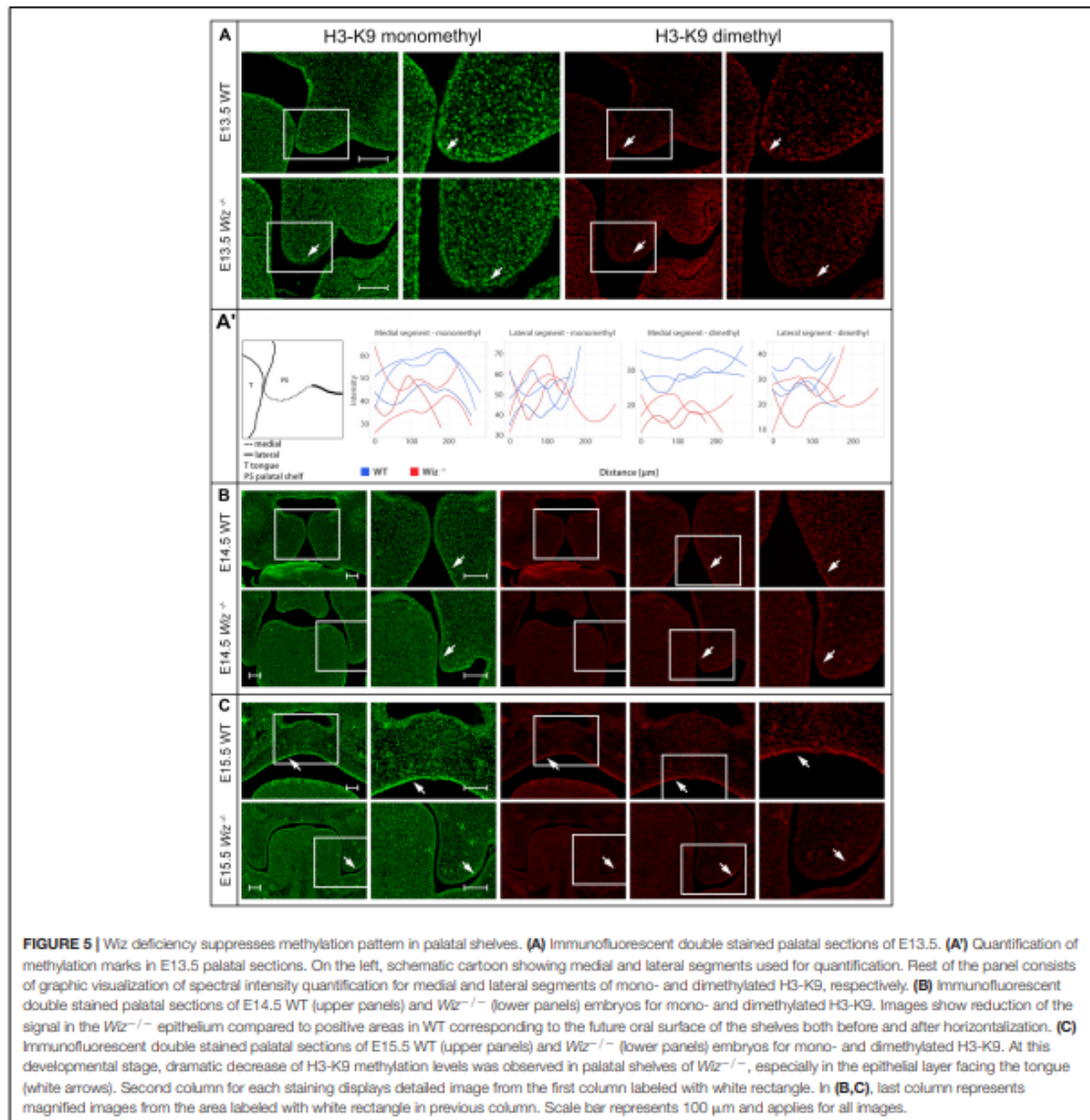
It was previously shown (Ueda et al., 2006; Bian et al., 2015) that *Wiz* is a core subunit of the *G9a/GLP* methylation complex and important for the complex's specificity. The *G9a/GLP* complex independently regulates both H3-K9 and DNA methylation, resulting in transcriptional silencing (Tachibana et al., 2008). Several studies have provided insight into the role of *Wiz* in mice, such as linking *Wiz* deficiency with behavioral phenotypes and anxiety (Isbel et al., 2016). It has been proposed that



either WIZ or ZNF644 is sufficient for targeting the G9a/GLP complex to specific loci for H3-K9 methylation (Bian et al., 2015). On the other hand, multiple other G9a-associated molecules containing zinc finger motifs have been reported, such as PRDI-BF1 (Gyory et al., 2004) or ZNF217 (Banck et al., 2009). This may explain why the functional ablation of WIZ is not embryonically lethal as early as G9a or GLP themselves. Due to early embryonic lethality, $Wiz^{MommD30}$ model (Daxinger et al., 2013) is not suitable for studying the function of WIZ gene in later embryonic development such as palate formation. Also, early lethality of some $Wiz^{-/-}$ embryos suggests presence of other than craniofacial defects creating opportunity for further developmental studies.

The data presented in this article support our hypothesis that WIZ deficiency causes disruption of methylation known to be driven by the G9a/GLP methylation complex, which we show is coexpressed with WIZ in the palatal shelf. In fact, our findings showed decreased H3-K9 methylation levels *in vivo*, which may result in developmental defects in mice fetuses limited to orofacial areas, especially epithelia of developing palatal shelves. These observations would be interesting to explore further with a precise genetic reporter system for analysis of changes in epigenetic regulations based on binding reporter to dimethylated H3-K9 or directly on WIZ activity on artificial promoter with

reporter. It seems that specific population of epithelial cells on the medial edge of palatal process is affected. Highly specific molecular signature of these cells is likely crucial for the properly timed horizontalization and subsequent fusion of the palatal shelves. This hypothesis is supported by the fact that proliferation rate within the anterior and posterior region of the shelves is not changed despite emerging possible difference in shelf shape caused by the failure of the shelf horizontalization itself. Images used for presentation of this phenomenon are stage and section matched. $Wiz^{-/-}$ palatal shelves appear to have denser cells, which may not migrate properly and spread out to achieve the shape of WT palatal shelves. The inability to find alteration of expression between $Wiz^{-/-}$ and WT samples may be caused by the fact that whole palatal tissues were used for RT-qPCR, however, only small domain is affected by methylation defect, and thus single cell level investigation seems to be more appropriate. In addition, the relatively local effect of the mutation on the epithelium and subsequent presumable dysregulation of horizontalization timing explains why some of the $Wiz^{-/-}$ embryos display only incomplete cleft phenotype when the processes are able to reach each other but fail to fuse properly. Developmental delay of $Wiz^{-/-}$ palatal shelves horizontalization results in a loss of ability to fuse even if they manage to elevate. This observation is supported by Jin et al. (2008) reporting that



loss of *Zfhx1a*, a transcription modulator of signaling pathways activated by members of TGF- β superfamily, leads to a cleft palate phenotype due to delayed palatal shelf elevation, while shelf size or cell proliferation rate is unchanged. By the E16.5, all of the *Zfhx1a* mutant palatal shelves were elevated above the tongue but remained separated. This 24–48 h developmental delay caused the palatal shelves to miss the window of competence to fuse (Jin et al., 2008). A similar situation was observed in retinoic acid (RA) teratogenic effect on palatal development. It has been shown that RA caused failure of palatal shelf elevation (Tang et al., 2016).

Tang et al. showed that impaired palatal shelf elevation may be caused by delayed progress of cell condensation and the failure of the tongue withdrawal. No regional differences in cell proliferation ratio at E13.5 were reported in the RA induced cleft palate phenotype (Okano et al., 2007). On top of these findings, other observed phenotypes of E18.5 *Wiz*^{-/-} embryos such as cleft eyelids may be connected to the cleft palate phenotype as they share a similar developmental program, which consists of directional tissue growth followed by tissue fusion. Different types of eyelid defects were found among patients with cleft palate

diagnosis (Anchlia et al., 2011). Similarly, shorter snout in mouse embryo may indicate more general alteration in growth dynamic of orofacial area, which can result in cleft phenotypes.

The connection between epigenetic chromatin modification and craniofacial defects is very complex and may be dependent or independent on DNA or histone modifications (Du et al., 2015). In recent years, altered DNA methylation was linked to non-syndromic cleft palate development (Alvizi et al., 2017; Gonseth et al., 2019), indicating that difference in methylation marks may contribute to a cleft palate phenotype. Interestingly also maternal exposure to RA inducing palate clefting is connected to dysregulated DNA methylation pattern in palatal shelves (Kuriyama et al., 2008). The need for proper epigenetic regulation was observed also on the effect of folic acid or choline, which are important co-factors for synthesis of the methyl donor group from S-adenosyl methionine. Both co-factors were linked to decreased risk of isolated non-syndromic cleft palate occurrence (Shaw et al., 2006; Wilcox et al., 2007) when overused during pregnancy. Together with genetic evidence that mutations in *G9a* are linked with Kleeftstra syndrome, characterized by developmental delay and altered facial features (Willemssen et al., 2012), there is strong evidence that epigenetic regulation is involved in precise orchestration of timing in the critical developmental processes. Thus, palate development is one of the most vulnerable processes, because there is only a narrow window of competence when palatal shelves can fuse.

DATA AVAILABILITY STATEMENT

The datasets presented in this study can be found in online repositories. The names of the repository/repositories and accession number(s) can be found in the article/Supplementary Material.

ETHICS STATEMENT

The animal study was reviewed and approved by the Animal Care and Use Committee of the Institute of Molecular Genetics.

AUTHOR CONTRIBUTIONS

IB performed the experiments, analyzed the data, and wrote the manuscript. KS produced the mice and initiated the project. MP performed the experiments and analyzed the data. IMB generated the mouse model. JP designed the experiments, analyzed the data, wrote the manuscript, and supervised the research. RS wrote the manuscript and supervised the research. All authors contributed to the article and approved the submitted version.

FUNDING

This work was funded by the National Sustainability Program II (LQ1604) and the Czech Centre for Phenogenomics (LM2015040 and LM2018126) by the Ministry of Education, the Youth and Sports of the Czech Republic (MEYS), the

Biotechnology and Biomedicine Centre of the Academy of Sciences and Charles University in Vestec (BIOCEV) (CZ.1.05/1.1.00/02.0109), Higher quality and capacity for transgenic models (CZ.1.05/2.1.00/19.0395) by MEYS and the European Regional Development fund and Upgrade of the Czech Centre for Phenogenomics: developing toward translation research (CZ.02.1.01/0.0/0.0/16_013/0001789) by MEYS and the European Structural Investment Fund and project Deciphering biological role of ZNF644 to edit the activity of *G9a*/GLP methylation complex (GACR, 19-21696S) by Czech Science Foundation.

ACKNOWLEDGMENTS

Acknowledgment to Karel Harant and Pavel Talacko from Laboratory of Mass Spectrometry, Biocev, Charles University, Faculty of Science for performing LC/MS analysis.

SUPPLEMENTARY MATERIAL

The Supplementary Material for this article can be found online at: <https://www.frontiersin.org/articles/10.3389/fcell.2021.620692/full#supplementary-material>

Supplementary Figure 1 | Probe design for *in situ* hybridization. (A) Plasmid maps of *G9a*-pGEM[®]-T plasmids used for probe preparation and sequence of interest. (B) Plasmid maps of *GLP*-pGEM[®]-T plasmids used for probe preparation and sequence of interest. (C) Plasmid maps of *Wiz*-pGEM[®]-T plasmids used for probe preparation and sequence of interest. Colors in text are corresponding to colors in the plasmid map. Restriction sites are written in red, primers sequences written in bold and underlined. Created with BioRender.com. (D) *G9a*, *GLP*, and *Wiz* sense probes generated as a negative control for *in situ* images.

Supplementary Figure 2 | Generation of *Wiz* deficient mouse model. (A) Schematic cartoon visualizing targeting exon 4 of *Wiz* gene by CRISPR/Cas9 resulting in 32 nucleotide deletion, frame-shift mutation and premature stop codon. Created with BioRender.com. (B) Western blot analysis from *Wiz*^{-/-}, *Wiz*^{+/-}, and WT embryonic lysate showing protein *Wiz* sized 130 kDa in WT sample, lower amount in heterozygous sample and none present in KO sample. (C) Localization of SDS-Page gel cutout for Mass Spectrometry. (D) Mass spectrometry analysis from gel cutouts and graphic visualization of logarithmic number of particles for protein *Wiz* present in WT sample. Contrary to that, no *Wiz* protein detected in *Wiz*^{-/-} sample.

Supplementary Figure 3 | *Wiz* deficiency does not affect number of proliferative cells. (A) EdU labeling shows no difference in proliferation levels in palatal shelves between WT (upper panels) and KO (lower panels) palatal sections at E14.5. Scale bar represents 100 μ m and applies for all images. White rectangles on the right side panels show the area that is presented magnified on the left side panels respectively. (B) Quantification of EdU labeled proliferating cells shows no difference in ratio of proliferating cells between genotypes at E14.5 in anterior ($p = 0.305$) and posterior regions ($p = 0.468$) of palatal shelves. $n = 3$ *Wiz*^{-/-} vs. 3 WT embryos, with five sections from anterior and five sections from posterior part of shelves for each embryo. (C) Expression levels of representative genes from signaling pathways involved in palatogenesis do not change between genotypes. $n = 4$ *Wiz*^{-/-} and WT samples. Expression levels of the genes of interest were normalized to levels of *Rpl19* and are presented as levels relative to wild type (set as 1).

Supplementary Methods | Supplementary methods for SDS-PAGE and immunoblotting, in gel digestion, nLC-MS 2 Analysis, Data analysis, and Quantitative real time reverse transcription polymerase chain reaction (qRT-PCR).

REFERENCES

- Alvizi, L. K., X., Brito, L. A., Seselgyte, R., Moore, G. E., Stanier, P., et al. (2017). Differential methylation is associated with non-syndromic cleft lip and palate and contributes to penetrance effects. *Sci. Rep.* 7:2441. doi: 10.1038/s41598-017-02721-0
- Anchlia, S., Rao, K. S., Bonanthaya, K., Anupama, B., and Nayak, I. V. (2011). Ophthalmic considerations in cleft lip and palate patients. *J. Maxillofac. Oral Surg.* 10, 14–19. doi: 10.1007/s12663-010-0058-z
- Banck, M. S., Li, S., Nishio, H., Wang, C., Beutle, A. S., and Walsh, M. J. (2009). The ZNF217 oncogene is a candidate organizer of repressive histone modifiers. *Epigenetics* 4, 100–106. doi: 10.4161/epi.4.2.7953
- Bian, C., Chen, Q., and Yu, X. (2015). The zinc finger proteins ZNF644 and WIZ regulate the G9a/GLP complex for gene repression. *Elife* 4:e05606. doi: 10.7554/eLife.05606
- Bush, J. O., and Jiang, R. (2012). Palatogenesis: morphogenetic and molecular mechanisms of secondary palate development. *Development* 139, 231–243. doi: 10.1242/dev.067082 Erratum in: *Development* 139:828.
- Cox, J., Hein, M. Y., Lubner, C. A., Paron, I., Nagaraj, N., and Mann, M. (2014). Accurate proteome-wide label-free quantification by delayed normalization and maximal peptide ratio extraction, termed MaxLFQ. *Mol. Cell. Proteomics* 13, 2513–2526.
- Cox, J., and Mann, M. (2008). MaxQuant enables high peptide identification rates, individualized p.p.b.-range mass accuracies and proteome-wide protein quantification. *Nat. Biotechnol.* 26, 1367–1372.
- Daxinger, L., Harten, S. K., Oey, H., Epp, T., Isbel, L., Huang, E., et al. (2013). An ENU mutagenesis screen identifies novel and known genes involved in epigenetic processes in the mouse. *Genome Biol.* 14:R96. doi: 10.1186/gb-2013-14-9-r96
- Dickinson, M. E., Flenniken, A. M., Ji, X., Teboul, L., Wong, M. D., White, J. K., et al. (2016). High-throughput discovery of novel developmental phenotypes. *Nature* 537, 508–514. doi: 10.1038/nature19356 Erratum in: *Nature* 551:398.
- Du, J., Johnson, L. M., Jacobsen, S. E., and Patel, D. J. (2015). DNA methylation pathways and their crosstalk with histone methylation. *Nat. Rev. Mol. Cell Biol.* 16, 519–532. doi: 10.1038/nrm4043
- Enomoto, H., Nelson, C. M., Somerville, R. P., Mielke, K., Dixon, L. J., Powell, K., et al. (2010). Cooperation of two ADAMTS metalloproteases in closure of the mouse palate identifies a requirement for versican proteolysis in regulating palatal mesenchyme proliferation. *Development* 137, 4029–4038. doi: 10.1242/dev.050591
- Gonsath, S., Shaw, G. M., Roy, R., Segal, M. R., Asrani, K., Rine, J., et al. (2019). Epigenetic profiling of newborns with isolated orofacial clefts reveals widespread DNA methylation changes and implicates metastable epiallele regions in disease risk. *Epigenetics* 14, 198–213. doi: 10.1080/15592294.2019.1581591
- Gritli-Linde, A. (2007). Molecular control of secondary palate development. *Dev. Biol.* 301, 309–326. doi: 10.1016/j.ydbio.2006.07.042
- Gyory, L., Wu, J., Fejér, G., Seto, E., and Wright, K. L. (2004). PRDI-BF1 recruits the histone H3 methyltransferase G9a in transcriptional silencing. *Nat. Immunol.* 5, 299–308. doi: 10.1038/ni1046
- Hebert, A. S., Richards, A. L., Bailey, D. J., Ulbrich, A., Coughlin, E. E., Westphal, M. S., et al. (2014). The one hour yeast proteome. *Mol. Cell. Proteomics* 13, 339–347.
- Isbel, L., Prokopyuk, L., Wu, H., Daxinger, L., Oey, H., Spurling, A., et al. (2016). WIZ binds active promoters and CTCF-binding sites and is required for normal behaviour in the mouse. *Elife* 5:e15082. doi: 10.7554/eLife.15082
- Ito, Y., Yeo, J. Y., Chytil, A., Han, J., Bringas, P. Jr., Nakajima, A., et al. (2003). Conditional inactivation of Tgfb2 in cranial neural crest causes cleft palate and calvaria defects. *Development* 130, 5269–5280. doi: 10.1242/dev.00708
- Jin, J. Z., Li, Q., Higashi, Y., Darling, D. S., and Ding, J. (2008). Analysis of Zfhx1a mutant mice reveals palatal shelf contact-independent medial edge epithelial differentiation during palate fusion. *Cell Tissue Res.* 333, 29–38. doi: 10.1007/s00441-008-0612-x
- Justice, M., Carico, Z. M., Stefan, H. C., and Downen, J. M. (2020). A WIZ/Cohesin/CTCF complex anchors DNA loops to define gene expression and cell identity. *Cell Rep.* 31:107503. doi: 10.1016/j.celrep.2020.03.067
- Kim, S., Prochazka, J., and Bush, J. O. (2017). Live imaging of mouse secondary palate fusion. *J. Vis. Exp.* 125:e56041. doi: 10.3791/56041
- Kuriyama, M., Udagawa, A., Yoshimoto, S., Ichinose, M., Sato, K., Yamazaki, K., et al. (2008). DNA methylation changes during cleft palate formation induced by retinoic acid in mice. *Cleft Palate Craniofac. J.* 45, 545–551. doi: 10.1597/07-134.1
- Lan, Y., and Jiang, R. (2009). Sonic hedgehog signaling regulates reciprocal epithelial-mesenchymal interactions controlling palatal outgrowth. *Development* 136, 1387–1396. doi: 10.1242/dev.028167
- Livak, K. J., and Schmittgen, T. D. (2001). Analysis of relative gene expression data using real-time quantitative PCR and the 2^{-ΔΔC_T} method. *Methods* 25, 402–408. doi: 10.1006/meth.2001.1262
- Nakajima, A., Shuler, C. F., Gulka, A. O. D., and Hanai, J. I. (2018). TGF-β signaling and the epithelial-mesenchymal transition during palatal fusion. *Int. J. Mol. Sci.* 19:3638. doi: 10.3390/ijms19113638
- Okano, J., Suzuki, S., and Shiota, K. (2007). Involvement of apoptotic cell death and cell cycle perturbation in retinoic acid-induced cleft palate in mice. *Toxicol. Appl. Pharmacol.* 221, 42–56. doi: 10.1016/j.taap.2007.02.019
- Rice, R., Spencer-Dene, B., Connor, E. C., Gritli-Linde, A., McMahon, A. P., Dickson, C., et al. (2004). Disruption of Fgf10/Fgfr2b-coordinated epithelial-mesenchymal interactions causes cleft palate. *J. Clin. Invest.* 113, 1692–1700. doi: 10.1172/JCI20384
- Shaw, G. M., Carmichael, S. L., Laurent, C., and Rasmussen, S. A. (2006). Maternal nutrient intakes and risk of orofacial clefts. *Epidemiology* 17, 285–291. doi: 10.1097/01.ede.0000208348.30012.35
- Tachibana, M., Matsumura, Y., Fukuda, M., Kimura, H., and Shinkai, Y. (2008). G9a/GLP complexes independently mediate H3K9 and DNA methylation to silence transcription. *EMBO J.* 27, 2681–2690. doi: 10.1038/emboj.2008.192
- Tachibana, M., Sugimoto, K., Nozaki, M., Ueda, J., Ohta, T., Ohki, M., et al. (2002). G9a histone methyltransferase plays a dominant role in euchromatic histone H3 lysine 9 methylation and is essential for early embryogenesis. *Genes Dev.* 16, 1779–1791. doi: 10.1101/gad.989402
- Tachibana, M., Ueda, J., Fukuda, M., Takeshi, N., Ohta, T., Imamura, H., et al. (2005). Histone methyltransferases G9a and GLP form heteromeric complexes and are both crucial for methylation of euchromatin at H3-K9. *Genes Dev.* 19, 815–826. doi: 10.1101/gad.1284005
- Tang, Q., Li, L., Lee, M. J., Ge, Q., Lee, J. M., and Jung, H. S. (2016). Novel insights into a retinoic-acid-induced cleft palate based on Rac1 regulation of the fibronectin arrangement. *Cell Tissue Res.* 363, 713–722. doi: 10.1007/s00441-015-2271-z
- Tyanova, S., Temu, T., Sinitcyn, P., Carlson, A., Hein, M. Y., Geiger, T., et al. (2016). The Perseus computational platform for comprehensive analysis of (pro)teomics data. *Nat. Methods* 13, 731–740.
- Ueda, J., Tachibana, M., Ikura, T., and Shinkai, Y. (2006). Zinc finger protein WIZ links G9a/GLP histone methyltransferases to the co-repressor molecule CtBP. *J. Biol. Chem.* 281, 20120–20128. doi: 10.1074/jbc.M603087200
- Wilcox, A. J., Lie, R. T., Solvoll, K., Taylor, J., McConaughy, D. R., Abyholm, F., et al. (2007). Folic acid supplements and risk of facial clefts: national population based case-control study. *BMJ* 334:464. doi: 10.1136/bmj.39079.618287.0B
- Wilkinson, D. G., and Nieto, M. A. (1993). Detection of messenger RNA by in situ hybridization to tissue sections and whole mounts. *Methods Enzymol.* 225, 361–373. doi: 10.1016/0076-6879(93)25025-w
- Willemsen, M. H., Vulto-van Silfhout, A. T., Nillesen, W. M., Wissink-Lindhout, W. M., van Bokhoven, H., Philip, N., et al. (2012). Update on Kleeftstra Syndrome. *Mol. Syndromol.* 2, 202–212. doi: 10.1159/000335648
- Zhang, Z., Song, Y., Zhao, X., Zhang, X., Fermin, C., and Chen, Y. (2002). Rescue of cleft palate in Mx1-deficient mice by transgenic Bmp4 reveals a network of BMP and Shh signaling in the regulation of mammalian palatogenesis. *Development* 129, 4135–4146.

Conflict of Interest: The authors declare that the research was conducted in the absence of any commercial or financial relationships that could be construed as a potential conflict of interest.

Copyright © 2021 Bukova, Szczekowska, Prochazkova, Beck, Prochazka and Sedlacek. This is an open-access article distributed under the terms of the Creative Commons Attribution License (CC BY). The use, distribution or reproduction in other forums is permitted, provided the original author(s) and the copyright owner(s) are credited and that the original publication in this journal is cited, in accordance with accepted academic practice. No use, distribution or reproduction is permitted which does not comply with these terms.

SUPPLEMENTARY METHODS

SDS-PAGE and immunoblotting

Embryonic tissue was harvested into RIPA buffer (150mM NaCl, 1% Nonidet P-40, 0.5% Sodium deoxycholate, 0.1% SDS, 1mM EDTA, 50mM Tris/HCl pH8) with phosphatase and protease inhibitors PhosSTOP (Roche, Germany) and cOmplete Tablets, mini (Roche, Germany) and dissociated in Tissue Lyser II (Qiagene). Concentration of proteins was estimated by the BCA method (Pierce Biotechnology Inc., Rockford, USA). Before separation by 7% SDS-PAGE, 100 mM DTT and 0.01% bromophenol blue were added to the cell lysates. The same protein amount (20 µg) was loaded into each well. After electrophoresis, proteins were electrotransferred from the gel onto a nitrocellulose membrane using the wet transfer method and detected by specific antibodies WIZ Antibody (Novus Biologicals, NBP1-80586) at 1:1000 dilution and β -tubulin (Santa Cruz, cs-2146s. Detection was performed by SuperSignal West Pico PLUS Chemiluminiscent Substrate (Thermo Scientific, #34580).

In gel digestion

Individual bands containing proteins of interest were excised from Coomassie stained SDS PAGE gel using a razor blade and cut into small pieces (aprox. 1 mm x 1 mm). Bands were destained by sonication for 30 min in 50% acetonitrile (ACN) and 50mM ammonium bicarbonate (ABC). After destaining, solution was removed and gels were dried in ACN. Disulfide bonds were reduced using 10mM DTT in 100mM ABC at 60°C for 30 min. After that, samples were again dried with ACN and free cystein residues were blocked using 55mM iodoacetamide in 100mM ABC for 10 min at room temperature in dark. Samples were dried thoroughly and digestion buffer (10% ACN, 40mM ABC and 13 ng/µl trypsin) was added to cover gel pieces. Proteins were digested at 37 °C overnight. After digestion, 150 µl of 50% ACN with 0,5% formic acid was added and sonicated for 30 min. Supernatant containing peptides was replaced to a new micro centrifuge tube and another 150 µl of elution solution was added and sonicated for 30 min. This solution was removed, combined with previous solution and dried using Speedvac. Dried peptides were reconstituted in 2% ACN with 0,1% TFA and injected into Ultimate 3000 Nano LC coupled to Orbitrap Fusion.

nLC-MS 2 Analysis

Nano Reversed phase columns (EASY-Spray column, 50 cm x 75 µm ID, PepMap C18, 2 µm particles, 100 Å pore size) were used for LC/MS analysis. Mobile phase buffer A was composed of water and 0.1% formic acid. Mobile phase B was composed of acetonitrile and 0.1% formic acid. Samples were loaded onto the trap column (C18 PepMap100, 5 µm particle size, 300 µm x 5 mm, Thermo Scientific) for 4 min at 18 µl/min loading buffer was composed of water, 2% acetonitrile and 0.1% trifluoroacetic acid. Peptides were eluted with Mobile phase B gradient from 4% to 35% B in 120 min. Eluting peptide cations were converted to gas-phase ions by electrospray ionization and analyzed on a Thermo Orbitrap Fusion (Q-OT- qIT, Thermo Scientific). Survey scans of peptide precursors from 350 to 1400 m/z were performed in orbitrap at 120K resolution (at 200 m/z) with a 5×10^5 ion count target. Tandem MS was performed by isolation at 1.5 Th with the quadrupole, HCD fragmentation with normalized collision energy of 30, and rapid scan MS analysis in the ion trap. The MS2 ion count target was set to 104 and the max injection time was 35 ms. Only those precursors with charge state 2–6 were sampled for MS2. The dynamic exclusion duration was set to 45 s with a 10 ppm tolerance around the selected precursor and its isotopes. Monoisotopic precursor selection was turned on. The instrument was run in top speed mode with 2 s cycles (Hebert, Richards et al., 2014).

Data analysis

All data were analyzed and quantified with the MaxQuant software (version 1.6.3.4) (Cox & Mann, 2008). The false discovery rate (FDR) was set to 1% for both proteins and peptides and we specified a minimum peptide length of seven amino acids. The Andromeda search engine was used for the MS/MS spectra search against the *Mus musculus* database (downloaded from Uniprot on January 2021, containing 17 059 entries). Enzyme specificity was set as C-terminal to Arg and Lys, also allowing cleavage at proline bonds and a maximum of two missed cleavages. Dithiomethylation of cysteine was selected as fixed modification and N- terminal protein acetylation and methionine oxidation as variable modifications. The “match between runs” feature of MaxQuant was used to transfer identifications to other LC-MS/MS runs based on their masses and retention time (maximum deviation 0.7 min) and this was also used in quantification experiments. Quantifications were performed with the label-free algorithm in MaxQuant (Cox et al., 2014). Data analysis was performed using Perseus 1.6.1.3 software (Tyanova et al., 2016).

Quantitative real time reverse transcription polymerase chain reaction (qRT-PCR)

Total RNA from E13.5 palatal shelves was isolated using RNeasy Mini Kit (Qiagen, USA) according to the manufacturer's protocol. 4 embryos from *Wiz^{-/-}* and 4 control littermates were used for the analysis. All samples were run in technical triplicates. cDNA was synthesized from 1000 ng of total RNA with Random Primers and Oligo (dT)15 primer (Promega, USA) using M-MLV Reverse Transcriptase and buffer (Promega, USA), RNasin® Ribonuclease Inhibitor (Promega, USA) and dNTP, Deoxynucleotide Mix 10 mM (Sigma, Germany). qRT-PCR was performed in The LightCycler® 480 (Roche, Germany) using LightCycler® 480 SYBR Green I Master (Roche, Germany).

The following sets of primers were used:

Wnt5a: FW: 5'-CAAATAGGCAGCCGAGAGAC-3', RV: 5'-CTCTAGCGTCCACGAACTCC-3'

Axin1: FW: 5'-GCTGACACGCTATCCCTTAC-3', RV: 5'-TACTCTCCTGCATCTCCCTT-3'

Axin2: FW: 5'-GTCCGCCTCCCCAAAG-3', RV: 5'-TCCAGTTCCTCTCAGCAATC-3'

Cdh1: FW: 5'-GTCCTGCCAATCCTGATGAA-3', RV: 5'-GAACACCAACAGAGAGTCGT-3'

Etv4: FW: 5'-AGCAGGAAGCCACCACT-3', RV: ATGGCGATTTGTCTGGGG-3'

Etv5: FW: 5'-CCCGAGATTACTGTGCTGAC-3', RV: 5'-ATGGCTGCTGGAGAAATACC-3'

Gli1: FW: 5'-GAGGTTGGGATGAAGAAGCA-3', RV: 5'-CATTGGATTGAACATGGCGT-3'

HES1: FW: 5'-CCAAGCTAGAGAAGGCAGAC-3', RV: 5'-GGTATTTCCCCAACACGCTC-3'

Bmp2: FW: 5'-AGCAGCAACACTAGAAGACAG-3', RV: 5'-TGTGGAGACTCTCTCAATGGA-3'

Bmp4: FW: 5'-GAACAACTTGCTGGAAAGGC-3', RV: 5'-TCATTGCAGCTTTCTAGAGGTC-3'

Spry1: FW: 5'-GCCCAGTATCTGTGAAGGAC-3', RV: 5'-ATACCAGGGGCAAATCAGAC-3'

Msx2: FW: 5'-CTCGGTCAAGTCGGAAAA-3', RV: 5'-GTGCAGGTGGTGGGG-3'

Shh: FW: 5'-GAATCCAAAGCTCACATCCAC-3', RV: 5'-CGTAAGTCCTTACCAGCTTG-3'

TGF- β : FW: 5'-ACTGATACGCCTGAGTGGCT-3', RV: 5'-
TTGCTGTCACAAGAGCAGTGA-3'

Notch2: FW: 5'-GCCACCTGCAATGACTTCA-3', RV: 5'-
CACTCGTCCACTTCATACTCAC-3'

Fgf10: FW: 5'- CAACTCCGATTTCCTGATGT-3', RV: 5'-
GCTGTTCTCCTTCACCAAGT-3'

Rpl19 FW: 5'-ATGAGACCAATGAAATCGCC-3', RV: 5'-CACAGGCTTGCGGATGA-3'

The relative quantity of cDNA was estimated by the $\Delta\Delta C_t$ method (Livak & Schmittgen, 2001). Expression levels of the genes of interest were normalized to levels of Rpl19 and are presented as levels relative to wild type (set as 1).